UNIVERSIDADE FEDERAL DO ESPÍRITO SANTO
CENTRO TECNOLÓGICO
PROGRAMA DE PÓS - GRADUAÇÃO EM ENGENHARIA ELÉTRICA

CLEMENS HÄGELE

POLYMER OPTICAL FIBER CURVATURE MEASURING TECHNIQUE BASED ON SPECKLE PATTERN IMAGE PROCESSING

VÍTORIA
2015

Dados Internacionais de Catalogação-na-publicação (CIP)
(Biblioteca Setorial Tecnológica,
Universidade Federal do Espírito Santo, ES, Brasil)

Hägele, Johann Clemens, 1984-H142p
Polymer optical fiber curvature measuring technique based on speckle pattern image processing / Johann Clemens Hägele. – 2015.
156 f. : il.

Orientador: Anselmo Frizera Neto.
Coorientador: Maria José Pontes.
Dissertação (Mestrado em Engenharia Elétrica) – Universidade Federal do Espírito Santo, Centro Tecnológico.

1. Speckle. 2. Processamento de imagens. 3. Fibras ópticas. 4. Polímeros. 5. Reconhecimento de padrões. 6. Sensor de curvatura. I. Frizera Neto, Anselmo. II. Pontes, Maria José. III. Universidade Federal do Espírito Santo. Centro Tecnológico. IV. Título.

CDU: 621.3

CLEMENS HÄGELE

Dissertação apresentada ao Programa de Pós - Graduação em Engenharia Elétrica – PPGEE, do Centro Tecnológico das Universidade Federal do Espírito Santo – UFES, como requisito parcial para obtenção do Grau de Mestre em Engenharia Elétrica.

Orientador:	Anselmo Frizera Neto
Co - Orientadora:	Maria José Pontes

VÍTORIA

2015

CLEMENS HÄGELE

Dissertação apresentada ao Programa de Pós-Graduação em Engenharia Elétrica – PPGEE, do Centro Tecnológico das Universidade Federal do Espírito Santo – UFES, como requisito parcial para obtenção do Grau de Mestre em Engenharia Elétrica.

Aprovada em 15 de Outubro de 2015

BANCA EXAMINADORA

Prof. Dr. Anselmo Frizera Neto - Orientador
Universidade Federal do Espírito Santo – UFES

Profa. Dr. Maria José Pontes - Co - Orientadora
Universidade Federal do Espírito Santo – UFES

Prof. Dr. Alessandro Botti Benevides
Universidade Federal do Espírito Santo – UFES

Prof. Dr. Paulo Fernando da Costa Antunes
Universidade de Aveiro – UA

Abstract

A self-developed light intensity-modulated curvature measuring principle for the measurement of bending angles within a range from $-120°$ to $+130°$ under application of a Polymer Optical Fiber is described in the present work. The determination of the bending angle is based on the graphical analysis of the speckle-pattern that is affected by the curved fiber. The contours of speckles in a defined region of interest in the speckle-pattern are made visible by an edge-detection algorithm and their amount is set in relation to the bending angle. The digital image of a speckle-pattern represents a source of image information that facilitates the further analysis by a variety of image processing techniques. The purpose of this work is the evaluation of a graphical analysis of a speckle-pattern for the curvature measurement. The research incorporates the basic study of general effects on the fiber under curvature until the development of a final measurement setup that facilitates a reliable and precise measurement of the bending angle. Coherent light with a wavelength of 632.8 nm is propagated through a looped Polymer Optical Fiber and received by a 5-Megapixel Charge-Coupled-Device-camera, positioned on the fiber output face. An especially designed acrylic goniometer facilitates the defined bending of the fiber for different fiber loop configurations. Different fiber arrangements and spatial image filters are evaluated under consideration of precision of bending angle gauging and computational efficiency. A developed digital signal processing routine performs a signal noise reduction and precision improvement for the bending angle measurement. Practical results revealed the existence of a non-linear dependence in static and dynamic operation in the range from $-120°$ to $+130°$ between the geometrical arrangements of the fiber, the average pixel intensity, the amount of detected speckle contours and the bending angle. A potential application of the sensor for the measurement of human joint movement and posture in the medical field of rehabilitation is possible. The curvature measurement for an application in the robotic field or industrial application is also convenient.

Acknowledgments

Firstly, I would like to thank my girlfriend Katia for the her patience, comprehension, motivation and constant assistance during the work on the master thesis. I would like to thank my mother, my sister, my brother and my friends for their assistance and steady motivation meanwhile writing on the master thesis.

Gratitude is dedicated to the coordinator of the *Postgraduate Program in Electrical Engineering*, Moisés Renato Nunes Ribeiro, for making the Post-Graduation at *Universidade Federal do Espírito Santo* possible. I want to thank my supervisor Anselmo Frizera Neto and Co-Supervisor Maria José Pontes for their technical orientation and support during the work on the master thesis.

In thanks to *Laboratório de Telecomunicações* (LABTEL) from *Universidade Federal do Espírito Santo* (UFES) for the opportunity to study in Brazil. Gratitude to *Fundação de Amparo à Pesquisa do Espírito Santo* (FAPES) for the scholarship. Thanks to *Petrobras*, *Coordenação de Aperfeiçoamento de Pessoal de Nível Superior* (CAPES) for the financial support of the project.

Contents

1. Introduction

1.1. Motivation

The application of Polymer Optical Fiber-based sensors became more attractive in the last few years according to the improvement of the highly complex manufacturing process and material compositions of the Polymer Optical Fiber (POF). POF-based sensor applications can be found in the industry, the domestic, medical, aerospace, automobile field. POF-curvature sensors based on light intensity-modulation are increasingly utilized in the field of human joint movement analysis by the advantageously characteristics such as lightweight, cost efficiency, mechanical robustness, electromagnetic interference immunity and simplicity in application [1], [2].

Angular joint movement in static operation is analyzable by radiographic and stereo radiographic imaging technology, characterized by highly time consuming, technically complex and harmful by the fact of the patients repeated X-ray-exposure. Non-invasive skin-mounted sensor concepts that are utilized to examination of limb curvature in static operation are the spinal mouse, flexible curves, electromagnetic and and gyroscope sensors [3], [4].

The well-established measuring technique for angular joint movement in dynamic operation, composed of CCD-cameras and reflecting markers is characterized by high installation effort and complexity [4].

A reliable high precision curvature sensor based on light intensity-modulation to gauge the dynamic angles of a human knee joint is presented in [5]. The characteristic curve possess an exponential dependence in the range from $-125°$ to $+125°$ and a linear range between $-45°$ and $+25°$, as depicted on figure 1.1. The fiber core is provided with a *Sensitive Zone* consisting of grinded fine cavities in a defined pattern. The manufacturing process is highly precise and needs special tools and equipment. A stronger signal attenuation is induced by the removal of

the cladding and the bending direction of the fiber is detectable while the mechanical flexibility and robustness is limited. A cracking at a bending angle of 140° is reported in [5]. The generated curvature data is transmitted via *ZigBee* to a personal computer for its analysis and documentation. The signal response as a function of the bending angle represents high precision and stability. The perturbation by loose parts of the fiber between the knee joint and the control device weared on the persons waist were noticed.

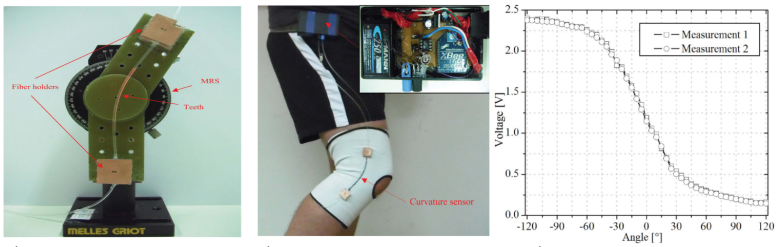

a) b) c)

Figure 1.1: Knee curvature sensor: a) Measurement setup b) Attachment of curvature sensor on human body c) Signal output as a function of the bending angle, adapted from [5].

The constant movement of the limb and the body makes the attachment of the curvature sensor on the human body challenging. The curvature sensor has to resist the movement of the leg in the three dimensions and the body movement in the sagittal and frontal plane, in case of a knee curvature sensor.

Several researches proved that the signal attenuation of a curved fiber in relation to the bending angle is non-linear [2], [6], [5], [7], [8], [9], [10], [11]. The mechanical manipulation of the fiber has no influence on shape of the non-linear characteristic curve. The mechanical robustness and flexibility is preserved for a non-manipulated fiber while the sensor sensitivity is comparatively low.

Speckles are defined as *Modal Noise* in literature and the time-varying intensities of the speckles inside the speckle-pattern represent a challenging task for the image information extraction [6]. The bending shape of the fiber is indicated as non-linear and depends mainly on the stiffness of the fiber as described in [10] and [7]. Measurement setups that intend to generate a defined bending at a constant bending radius and changing bending angle is presented in [11] and [12]. The extensive measurement setups are characterized by highly precise results. The

bending characteristic depends on the bending radius, bending angle, temperature, material properties of fiber. The signal attenuation as a function of the bending angle is influenced for an alteration of one of these parameters [6], [2].

In the present work, coherent light with a wavelength of 632.8 nm is propagated through a looped Polymeric Optical Fiber and received by a Charge-Coupled-Device camera positioned on the fiber back-end. An embedded system provided with a 5-Megapixel CCD-Camera controls acquisition parameters and transmits the image data via *TCP/IP* to a desktop computer for subsequent image processing tasks. The contours of speckles in a defined region of interest in the speckle-pattern are made visible by an edge-detection algorithm and their amount is set in relation to the bending angle. The signal response is compared to the commonly known speckle image processing technique *Speckle Mean Intensity Variation* as presented in [13].

All components are mounted on a self-developed acrylic goniometer that facilitates the defined bending of the fiber. Different fiber loop arrangements, spatial image filters and speckle image processing techniques are examined under consideration of precision for the bending angle gauging and computing efficiency. Digital Signal Processing (DSP) routines were developed for noise suppression and precision improvement for the bending angle measurement. The wireless sensor concept as presented in [5] represents a possible application example for the present measurement method.

A potential application for the measurement of human joint movement and posture in the medical field of rehabilitation is possible. Industrial tasks in the robotic field application would be convenient.

1.2. Scope of The Work

The present research investigates the influence of a curved polymer optical fiber on a speckle-pattern for the measurement of the bending angle in the range from $-120°$ to $130°$. The speckle-pattern is analyzed graphically with a self-developed

arrangement of image processing techniques and digital signal processing routines. An elementary measurement setup consisting of an acrylic goniometer, a He-Ne-Laser to provide light with a wavelength of 632.8 nm, a 5-Megapixel CCD-camera and a polymer optical fiber produces reliable and stable measurement results of the bending angle . Several parameters in the experimental setup such as spatial image filters, addition of a polarizer, amount of fiber loops and image parameters are varied for a detailed system identification. The general influences of temperature and mechanical perturbations on the measurement setup will be investigated.

1.3. Objectives

A new method for the curvature analysis based on the graphical analysis of speckle-pattern variation is evaluated and described in the present work. The application of image processing stages facilitates the detection and counting of speckle contours in a defined region of interest of the speckle-pattern.

An experimental setup that enables the examination of the sensor principle for future application in the analysis of human joint movement analysis has to be created. The setup has to include the attachment of different fiber arrangements, an embedded system and, a CCD-camera and their power supply. The experimental setup should produce a uniform shape of the bent fiber to ensure a precise bending angle measurement.

A system description of the experimental setup that facilitates the determination of disturbances on the speckle-pattern during fiber bending has to be developed and therefore new types or similar experimental setups characterized by high precision can be developed. The optimum fiber arrangement that facilitates a compromise between adequate signal variation and feasibility in implementation for the measurement of bending angle has to be determined.

Influences of image processing stages such as spatial filtering methods and edge-detection parameters has to be determined thus a defined configuration for the image processing steps can be developed. The variation in amount of detected

contours induced by a curved fiber must be studied for different external influences such as temperature and mechanical waves. A detailed analysis of the output signal has to be performed for the subsequent filtering process that incorporates noise reduction and precise determination of bending angle.

A final comparison to the commonly known speckle image processing technique *Mean Speckle Intensity Variation* has to be made for an qualitative evaluation of the proposed speckle measuring technique.

1.4. Document Structure

The light propagation in the POF is a physical process which knowledge is essential for the present work, as presented in section 2.2. Speckle-patterns are graphically analyzed by image processing techniques. The origin of speckles and their main properties are reported in section 2.5. Further explanations of the curvature effects on the light propagation in chapter 2.6 are based on the physical theories of light propagation. Different physical mechanisms of signal attenuation and signal losses of the Polymer Optical Fiber are explained in section 2.3. An overview of the POF-based sensors demonstrates the variety of their application and working principles that are relevant for the present project. The sensor overview includes: POF-based sensors based on the graphical speckle-pattern analysis, curvature sensors based on light intensity modulation in general and for the analysis of joint movements, common techniques for the analysis of human joint movements, POF-based sensor for the analysis of human knee joint movement. The entire experimental design, including the images processing routine, for the curvature analysis is presented in chapter 3. An improved measurement setup based on the system identification analysis performed in section 4.2.3 is presented in subsection 3.3.1. The measurement results and the detailed interpretation are listed in section 4.1. The final measurement curves, processed by a self-developed digital signal processing procedures are illustrated in chapter 5. The final chapter 6 summarizes the projects success and gives some proposals for further research directions and possibilities.

2. Properties of Polymer Optical Fiber

2.1. The Multimode Polymer Optical Fiber

The ray path inside the fiber core is defined by the characteristic of the fiber such as *Singlemode* or *Multimode fiber*. The Singlemode fiber consists of a relatively thin core, even ten times thinner than the Multimode core, where the wave model of light is applied for the calculation of modes. The core diameter of the Multimode fiber type is sufficient for the analysis of the ray paths under assumption of the geometric ray-tracing model [2]. The *Normalized Frequency* determines the separation between both fiber groups.

The designation of the fiber type belongs firstly to the type of mode propagation inside the core such as *Singlemode* or *Multimode* and secondly on the type of refraction of modes, affected by the structure of the refractive index profile. The main refractive profiles of *Polymethyl Metacrylate* (PMMA)-POF Multimode fibers are: Step-Index (SI), Multi-Step-Index (MSI) and Graded-Index (GI). The Multimode PMMA-POF that is utilized in the current work is characterized by a Step-Index Refractive Index Profile [6], [2], [14], [15].

The refractive index profile of the Multimode Step-Index Fiber is uniform over the whole fibers length. The light ray enters the Multimode Step-Index Fiber input face at an incident angle within the range of the acceptance angle and reflects totally at the core-cladding interface [6], [2], [14], [15].

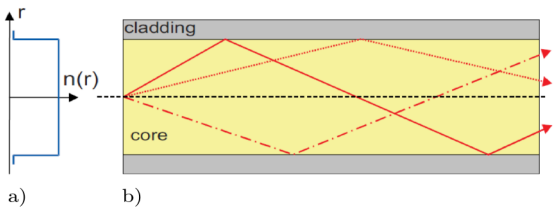

Figure 2.1: Multimode-Step-Index fiber a) Index profile b) Light propagation path [6], [2].

2.2. Light Propagation in POF

2.2.1. Total Reflection

The refractive index of the *Core* n_{co} must be higher than the refractive index of the *Cladding* n_{cl}, or $n_{co} > n_{cl}$ thus the conditions for a total reflection are given. In the contrary case of $n_{co} < n_{cl}$, interference is caused by induced *Cladding Modes*. The POF utilized in the current work owns a core refractive index of 1.49 and a cladding refractive index of 1.417. The refractive indexes of the core and the cladding depends on the material compositions and ambient influences such as temperature and humidity. The conditions of light propagation are determined by the ratio between core and cladding refractive indexes.

The light waves incident angle determines whether the light wave reflects totally or reflects partially on the core-cladding interface, as depicted on the following figure 2.2. For an ideal total reflection the incident angle β is the same as the angle of the refracted wave α. The angle of reflection depends on the order of the mode. Higher modes propagate under a large angle and lower modes under a lower angle of reflection. A total reflection is given when $\beta > \alpha_{min}$ where α_{min} is the incident angle for $\alpha' = 90°$.

In the condition of an ideal total reflection, the incident angle is the same as the angle of reflection therefore the direction of propagation of the modes is towards the fibers end face.

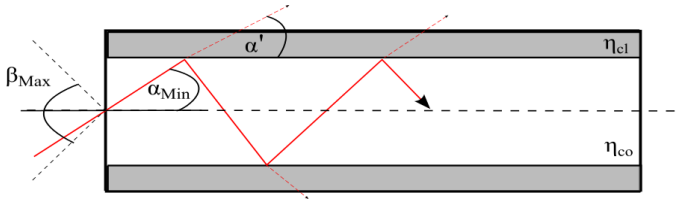

Figure 2.2: Ray path in condition of a total reflection [6], [16].

2.2.2. Numerical Aperture

The *Numerical Aperture* (NA) is considered as a main characteristic of the fiber and describes the capacity of light coupling on the input and the loss characteristics under curvature. A high value of the NA facilitates light coupling in a wide acceptance range.

Assuming the *Snell's law*, when light enters with an incident angle of β_{max} and a refraction angle of α_{max} then:

$$n_0 \cdot \sin(\beta_{max}) = n_{co} \cdot \sin(\alpha_{max}) = n_{co} \cdot \sin(90° - \gamma_{max}) \tag{2.1}$$

$$n_0 \cdot \sin(\beta_{max}) = \sqrt{(n_{co}^2 - n_{cl}^2)} \qquad in\ Air \quad n_0 = 1 \tag{2.2}$$

$$\sin(\beta_{max}) = \sqrt{(n_{co}^2 - n_{cl}^2)} \tag{2.3}$$

β_{max} is defined as the *Acceptance Angle* or *Aperture Angle* and sets the maximum incident angle for a light wave in which the conditions for a total reflection is still given without loss by waves refraction. The range of acceptance is the *Numerical Aperture* and is defined as:

$$NA = \sin(\beta_{max}) = \sqrt{n_{co}^2 - n_{cl}^2} \tag{2.4}$$

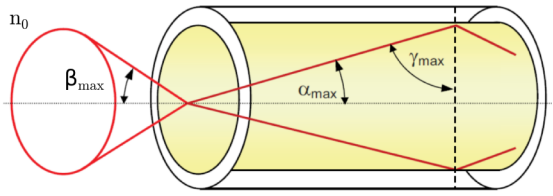

Figure 2.3: Illustration of numerical aperture, adapted from [6].

The fiber utilized in the current work is a Multimode Step-Index Polymer Optical Fiber, Model *Eska Premier*, fabricated by *Mitsubishi Rayon Co. LTD* and is characterized by a numerical aperture of 0.5 that corresponds to an acceptance angle of $\beta_{max} = 30°$ [17]. The acceptance angle is comparatively high and facilitates the coupling of light into the fiber without any precise aligning with a light source or a

receiver. Light enters the fiber in a defined angle range and exits the fibers output in a determined angle range as shown on figure 2.4.

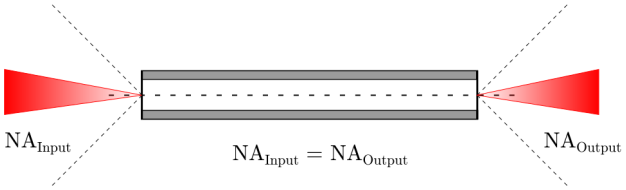

Figure 2.4: Numerical aperture characteristic of fiber input and output, adapted from [16].

The POF owns the largest numerical aperture and diameter in comparison to other fiber types, such as glass or silica fibers, as depicted on the following figure 2.5 [16], [2], [6].

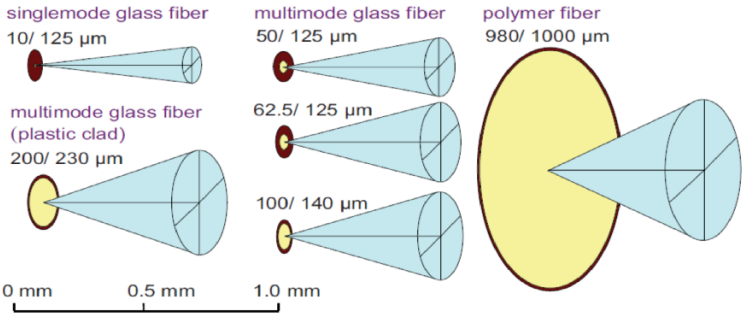

Figure 2.5: Numerical aperture of different fiber types [6].

2.2.3. The Mode Concept

Light waves are generally described as *Mode Propagation* in literature to discuss effects observed in the fiber optic propagation, which equations are derived by the Eigenvalue calculation of Maxwell's equations. Wave paths are traceable and effects of attenuation within a relaxed and bend fiber are describable by the mode theories and physical approaches. The current section describes the modes and their main properties.

In order to propagate a light wave from the fiber input to the output, it must constructively overlap itself with the own reflection wave. Therefore, the phase position repeats after a double reflection [6]. The thick lines perpendicular to the direction of light propagation on figure 2.6 identify the planes of the same phase angle. The spacing between the lines is defined as $\frac{\lambda}{n_{co}}$.

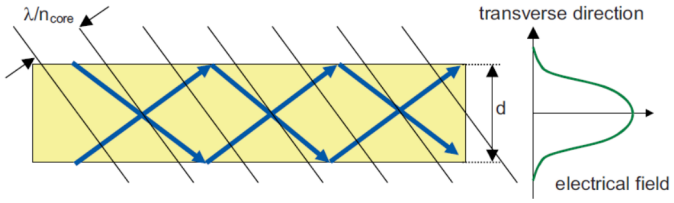

Figure 2.6: Formation of mode structure within the fiber core [6].

2.2.4. Types of Modes

Radiation Modes are generated when the range of the acceptance angle for a total reflection is exceeded. Radiation modes cross the core-cladding interface and are absorbed by the cladding, as depicted on the following figure 2.7.

Cladding Modes are formed when the cladding refractive index is higher than the core refractive index. A minor part of the radiated modes continue traveling inside the cladding. That specific type of light waves is designated as *Skew Rays*, *Leaky Waves* or *Tunneling Rays* and they are detectable even at more than twenty meters after the local of occurrence. This physical effect is considered as a disturbance and has significant influence on the signal quality in transmission and measurement. Radiation modes are not countable in contrary to guided modes [2], [6].

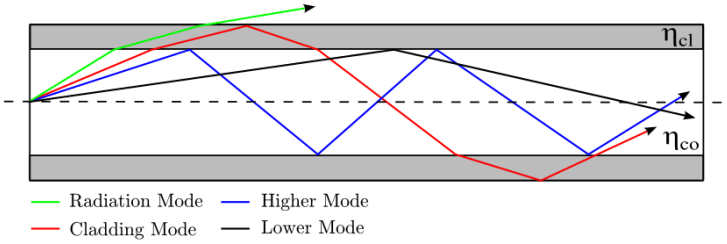

Figure 2.7: Types of modes, adapted from [6].

2.2.5. Number of Modes

As aforementioned, the type of light propagation inside the fibers core is grouped into the *Singlemode*- and *Multimode*-fibers. The *Normalized Frequency* determines the separation between both fiber groups and is defined as [6], [2]:

$$V = \frac{2\pi\rho}{\lambda} \cdot \sqrt{(n_{co}^2 - n_{cl}^2)} \tag{2.5}$$

or by substituting the term (2.4) for the *Numerical Aperture* in (2.5) results in (2.6).

$$V = \frac{2\pi\rho}{\lambda} \cdot NA \tag{2.6}$$

where ρ is the fiber core radius and λ the wavelength. If the value of the *Normalized Frequency* V is lower than 2.405, only one mode is propagated, as in case of the *Singlemode*-fiber, otherwise more modes are propagated, as in case of a *Multimode*-fiber. A value of 2432.65 for the normalized frequency under assumption of the parameters from the currently utilized fiber was derived in chapter 2.6 in equation (2.20).

The number of modes N for a Multimode-Step-Index fiber is derived by (2.7) [2], [6]:

$$N = \frac{V^2}{2} \tag{2.7}$$

The number of modes N of a Multimode-Graded-Index fiber is defined as (2.8) [2], [6]:

$$N = \frac{V^2}{4} \tag{2.8}$$

The number of modes depends mainly on the refractive indexes that are included in the equation of the NA, as can be observed from the equations (2.7) and (2.8) [2], [6], [16]. The number of modes with the parameters of the utilized fiber in the project is calculated as $2.96 \cdot 10^6$ as described in chapter 2.6 from equation (2.23).

2.2.6. Mode Coupling

The core-cladding interface surface is provided with discontinuities that originate from the manufacturing process and the polymer characteristics. The discontinuities provoke minimal deviations of the refractive index in the core-cladding interface and produce scattering centers, as illustrated on figure 2.8 and figure 2.9. Signal losses are generated by scattered light waves. *Mode Coupling* depends on the angle of light propagation and coupling length of the fiber. This physical effect generates a considerable part of light attenuation in the fiber and causes *Mode Dispersion* which reduces the bandwidth [16], [2], [6].

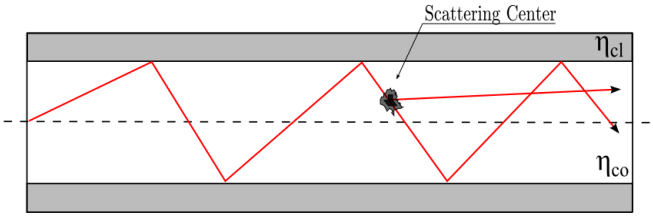

Figure 2.8: Mode coupling occurrence on scattering center, adapted from [6].

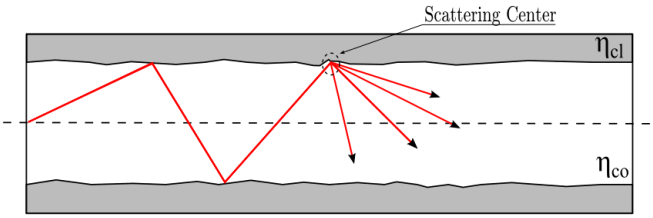

Figure 2.9: Mode coupling occurrence on core-cladding interface, adapted from [6].

2.2.7. Mode Conversion

Mode conversion arises in a curved fiber as in case of a microbend or macrobend and by fluctuations in the refractive index and is considered as a special condition of *Mode Coupling*.

Variations in the fiber position result in an altered reflection path of the light rays and generate losses by the presence of mode conversion. Mode calculation on a bent fiber is performed by the consideration of the cross-sections at the moments before and after bending. The fiber axis rotates by the amount of the bending angle as depicted on figure 2.10. An alteration of the light propagation direction leads to a rise in signal attenuation $Loss_{intensity}$ that amplifies for a higher bending angle α_{bent} or diminished bending radius r_{bent}, as described in the relations (2.9) [16], [2], [6].

$$\alpha_{bent} \uparrow \quad = \quad r_{bent} \downarrow \quad = \quad Loss_{intensity} \uparrow \tag{2.9}$$

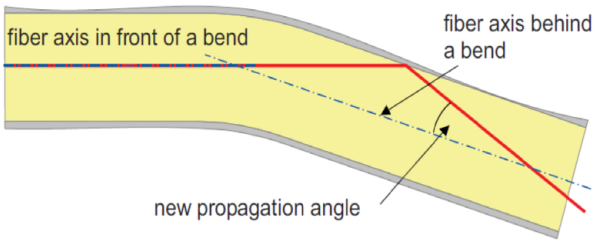

Figure 2.10: Mode propagation in the core of a curved fiber [6].

2.2.8. Mode-Dependent Attenuation

The material composition of the cladding is mainly responsible for *Mode- Dependent Attenuation*. A part of the electrical field escapes into the thinner cladding material by a distance in the order of the wavelength even in the conditions of a total reflection. That effect is also known as the *Goos-Hähnchen-Shift*.

A shift from the reflection plane into the optical thinner medium is the origin of this effect, as depicted on figure 2.11. The reflected light ray is slightly displaced on the core-cladding interface surface in the range of μm. The *Goos-Hähnchen Shift* is detectable in case of a reduced core diameter [16], [2], [6].

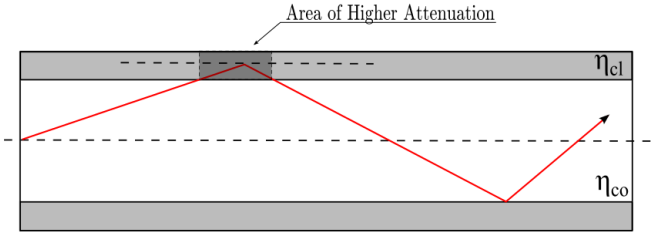

Figure 2.11: Mode dependent attenuation, Goos-Hähnchen Shift, adapted from [6].

2.3. Attenuation processes of the POF

The fibers physical characteristics include signal attenuation that is generated by the fiber characteristics such as length, core diameter, numerical aperture and wavelength.

Signal losses are induced by structural composition, external influences, internal material compositions fluctuations and impurities of the fiber.

Signal losses are not influenced by the operator, where the signal attenuation can be partly influenced by the choice of the fiber main characteristics.

2.3.1. Signal Attenuation Induced by Fiber Length

The signal attenuation of the fiber rises with the length l of transmission, arising from *Mode-Dependent Attenuation*. The transmission loss $P(l)$ in dependence with the fiber length l is defined as:

$$P(l) = P(0) \cdot e^{-a' \cdot l} \tag{2.10}$$

$P(l)$ is the signal power at the fibers output at a fiber length of l in km and $P(0)$ is the signal power on the fibers input at position 0. a' is the value of the *Attenuation Coefficient* in km^{-1} and commonly expressed logarithmic in dB/km [6], [2], [15].

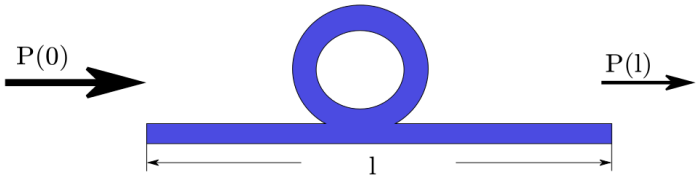

Figure 2.12: Signal attenuation in relation to fiber length [6].

$$\alpha = \frac{10}{l} \cdot \log\left(\frac{P(0)}{P(l)}\right) = 4,343 \cdot a' \tag{2.11}$$

The signal attenuation of the fiber utilized in the current work is 170 $\frac{dB}{km}$ at a wavelength of $\lambda = 650\ nm$ [17].

2.3.2. Signal Attenuation Induced by Numerical Aperture

The numerical aperture describes the *Acceptance Angle* in degree for that coupled light is still reflected totally inside the core. A high NA ensures a higher amount of light coupled into the fiber. A higher attenuation due to higher amount of refracting and radiating modes is provoked by this fact [6], [2], [15].

$$NA \uparrow \quad = \quad Attenuation \uparrow \tag{2.12}$$

2.3.3. Signal Attenuation Spectrum

The signal attenuation characteristics of a fiber as a function of the wavelength, determines the choice of light source for the transmitted signal. Material characteristics and compositions fluctuations are the origins of signal attenuation, as explained detailed in the following subsection 2.3.6. Impurities in the PMMA-material induce signal attenuation in the visible- and infrared- range of the light spectrum. Vibration Modes provoke attenuation in the red- and infrared-region of the light spectrum. Organic pollutants generate attenuation in the infrared range and electronic transitions of polymers in the region of ultraviolet light spectrum [6], [2], [15].

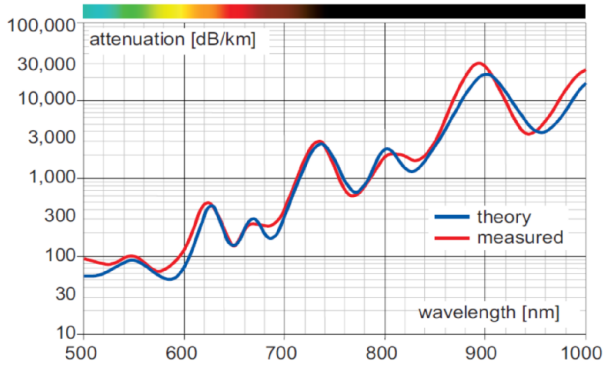

Figure 2.13: Attenuation spectrum of a PMMA-POF [6].

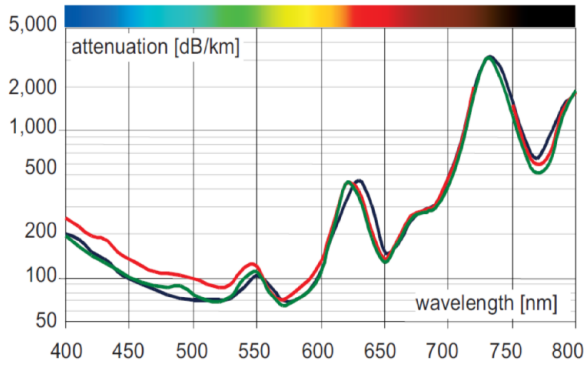

Figure 2.14: Attenuation spectrum of different standard-NA SI-POF (Measurement by POF-AC Nürnberg) [6].

2.3.4. Overview of Loss Mechanisms

The fiber experiences different kinds of signal losses, originated by the material composition and imprecision in the manufacturing process. The type of signal losses is separated into two main categories:

The *Intrinsic losses* and the *Extrinsic losses*. Each category is divided into several subdivisions, representing the origin of signal loss. Absorption, dispersion or radiation of the light rays are the physical mechanisms of signal loss, as depicted on the following figure 2.15.

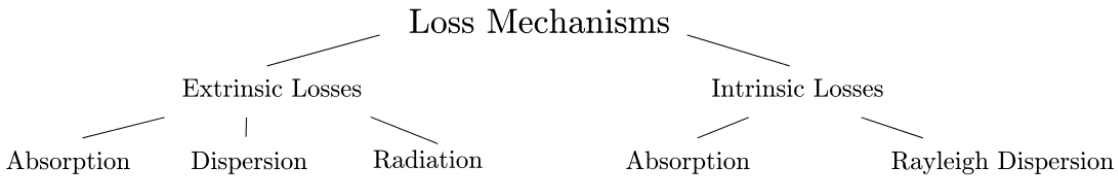

Figure 2.15: Overview of losses and their attenuation mechanisms in the POF [2].

2.3.5. Intrinsic Losses

Intrinsic losses originate from the organic polymer composition and they are reducible by improvement of the manufacturing process. Intrinsic losses alter the refractive index of the fiber over the distances in the order of the wavelength. The Intrinsic losses summed up, compose the *Ultimate Transmission Loss Limit* [6], [2], [15]. The composition of the intrinsic losses is illustrated on the following figure 2.16.

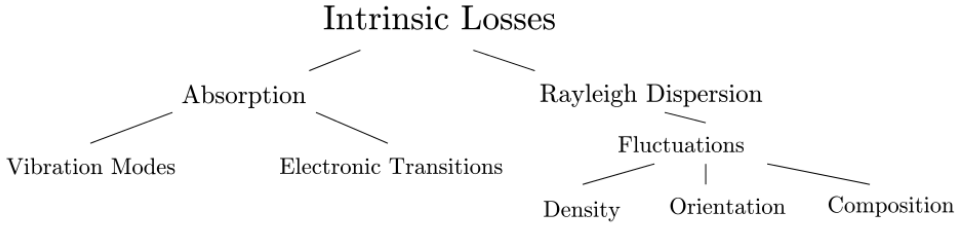

Figure 2.16: Overview of intrinsic losses and their attenuation mechanisms in the POF [2].

2.3.6. Extrinsic Losses

The manufacturing process generates impurities and imperfections representing the extrinsic losses. The composition of the extrinsic losses is illustrated on the following figure 2.17.

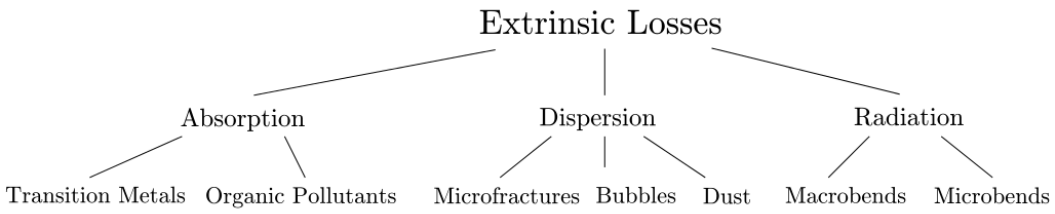

Figure 2.17: Overview of extrinsic losses and their attenuation mechanisms in the POF [2].

Absorption of light rays is induced by *Transition Metals* and *Organic Pollutants*. The transparency of the fibers core is reduced and the signal attenuation amplified by these impurities.

Dispersion of light rays according to *Dust*, *Microfractures*, *Bubbles* and *Structural Imperfections* generates inhomogenities of the core transparency and signal attenuation.

Radiation of light rays is produced by *Microbends* and *Macrobends* [6], [2], [15]. By the fact of relevance of microbends on the present work it is described in the following section.

2.3.6.1. Microbends

Radiation of light waves are induced by microbends. They represent slight scale-fluctuations of the fiber axis in the order of the fiber diameter. Microbends are produced by defects in the manufacturing process and by non-uniform lateral pressure during the cabling process [6], [2], [15].

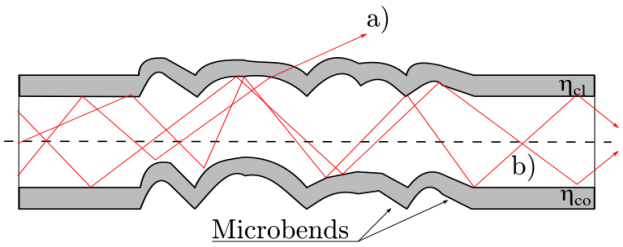

Figure 2.18: Microbends: a) Power loss from higher order modes b) Coupling to higher order modes, adapted from [2].

2.4. Signal Attenuation Induced by Ambient

2.4.1. Temperature

The fiber expands in size and shape under increasing temperature conditions and affects the refractive index of the fiber. The fiber tension is reduced under higher temperatures and yields to a reduced signal attenuation under curvature. The transparency of the core material declines with an rising temperature. A POF-based temperature sensor takes advantage of this physical condition, as described in [2], [14]. Temperature and relative humidity are significantly responsible for the aging progress of the fiber [6], [2].

The physical definition of the temperature effect on the local numerical aperture for a straight and a bent fiber is described in [18] and [19]. The core refractive index grows for higher temperatures and results in a higher numerical aperture and signal attenuation as described in [18]. The storage of the fiber in high temperature and constant high relative humidity causes constant aging of the fiber and destroys the internal structure of the POF. The signal attenuation lies in the range of 60 $\frac{dB}{km}$ for 1.000 h of storage at a temperature of +85° in a relative humidity of 95 %. The storage of the POF over a time range of 1000 h, a temperature rise from +80° to +85° causes an attenuation of 30 $\frac{dB}{km}$ as illustrated on figure 2.19. The temperature is the major factor for the aging of the fiber as can be seen from the graph 2.19.

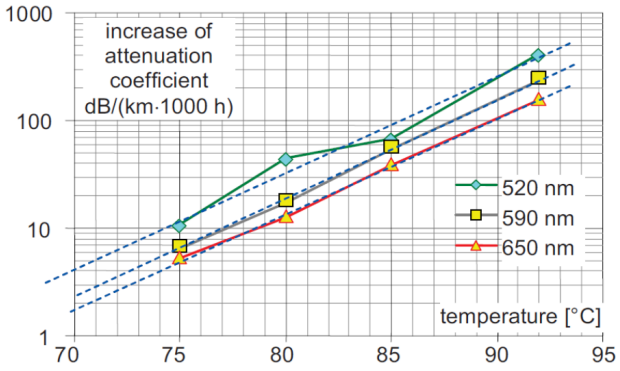

Figure 2.19: Aging process of a PMMA-POF [6].

2.4.2. Humidity

The absorption of water and humidity of the fiber leads to a reduced transparency of the core, causing higher signal attenuation, typically in the range of 10 $\frac{dB}{km}$. The absorption process is reversible, hence the humidity is released in dry environment. The capacity of absorbing water rises for an increasing storing time in a dry environment of higher temperature in the range of 70°. The attenuation of the currently utilized POF at 25° C is 170 $\frac{dB}{km}$ at a wavelength of 650 nm in a dry environment. The attenuation for the same temperature and wavelength in a relative humidity of 90 % rises to 190 $\frac{dB}{km}$ [6], [2].

2.5. Speckles

2.5.1. Formation of Speckles

A spatially coherent light source emits light waves with different but constant phases of the same frequency and amplitude through a Multicore POF. Microscopic scattering waves are generated when light waves travel against the optically rough surface of the fibers end face. The microscopic scattered light waves obtain a different phase in relation to the phase of the incident light wave. The dephased individual coherent wavelets interfere constructively in space, in equiphase, or destructively, in antiphase. A statistically intensity distributed granular spatial speckle-pattern is generated.

The speckle-pattern projected on the fiber end face, is temporally constant and spatially determined by the scattered surface structure, it is considered as a *fingerprint* of the micro structure. The reflection of a light ray on an optical rough surface erases the direction of preference. The surface roughness R_z is assumed as major than the wavelength λ of the light source. $R_z > \lambda$.
The surface roughness determines the structure of the speckle-pattern, in our case the fiber end face roughness.

Additional noise at the fiber end is caused when light is not transmitted at coupling points as depicted on the following figure 2.20. The phenomena of speckles in the specific case of Multimode fibers is described in this section [16], [2], [6].

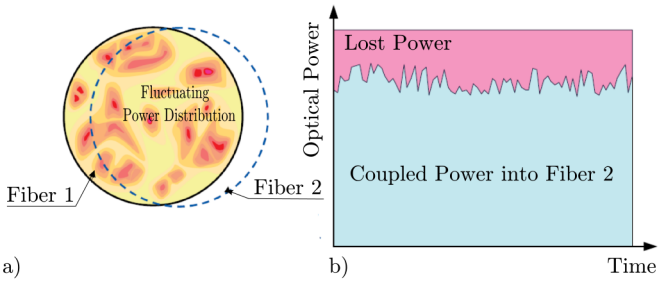

Figure 2.20: Modal noise at optical coupling point: a) Cross sections of two fibers b) Power loss diagram of optical coupling point, adapted from [6].

Speckle-patterns are producible by the illumination of optically rough surfaces by less coherent light sources like mercury lamps and laser diodes [20], [21].

Mechanical or temperature perturbations applied on the fiber sensing element induce a variation of the speckles in intensity, where the allover intensity of the speckle-pattern remains unchanged. The coherence of light and spectral width are the main influences on the speckle-patterns characteristics, besides the phase correlation between the modes. The structural distribution along the fiber provokes differential mode delay and spatial filtering [13]. Changes in speckle-patterns are analyzable by image processing techniques as described in section 3.5.

2.5.2. Statistical Intensity Distribution of a Speckle-Pattern

Speckles inside the speckle-pattern are stochastic spatially distributed and described quantitatively by probability and statistics. The emitted coherent laser light is linearly polarized. The speckle-patterns complex amplitude describes a circular Gaussian-statistic form in the complex plane. The intensity distribution of a speckle-pattern consists of a negative exponential probability, as illustrated on figure 2.22.

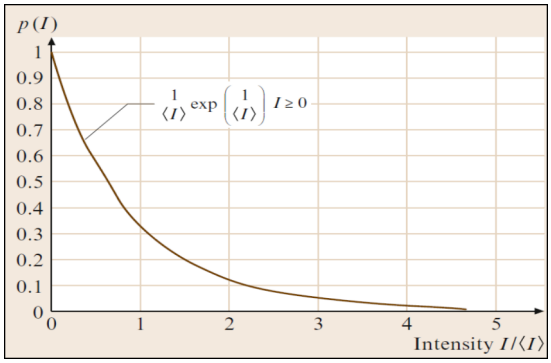

Figure 2.21: Probability density function based on numerous measurements taken from a speckle-pattern [21].

The probability density function is given by:

$$p(I) = \frac{1}{\langle I \rangle} \cdot exp\left(\frac{-I}{\langle I \rangle}\right) \quad I \geq 0 \tag{2.13}$$

where $\langle I \rangle$ is the mean value of the speckle-pattern intensity. The most probable intensity of the speckle distribution on the image plane is zero.

2.5.3. Speckle Size

The number of modes in a Multimode-Step-Index Fiber is defined as:

$$N = \frac{V^2}{2}$$

The modes travel through the fibers core on different optical paths and interfere on the fibers end face constructively, or destructively, producing the characteristic granular speckle-pattern. The statistical average speckle size, received in a defined distance to the scattered field, in our case the fiber end face, is defined as:

$$d_s \approx 2.44 \cdot \frac{\lambda \cdot f}{d_{co}} \tag{2.14}$$

where λ is the wavelength of propagated light, f the distance between the scattered field and the receiving image plane. d_{co} is the fibers core diameter. The *F-Number* is a commonly applied quantity in literature and is defined as:

$$F = \frac{f}{d_{co}} \tag{2.15}$$

The insertion of (2.15) in (2.14) results in (2.16).

$$d_s \approx 2.44 \cdot \lambda \cdot F \tag{2.16}$$

The speckle size grows at an increasing wavelength λ and F-Number. The speckle size is an important parameter for image acquisitions and is adjustable by the aperture of the receiving lens.

Amount of Speckle in Speckle-Pattern

The total amount of bright and dark speckles in a defined speckle-pattern array is defined as:

$$N_{pattern} = \frac{NA^2 \cdot d_{co}^2}{\lambda} \tag{2.17}$$

where NA is the Numerical Aperture, d_{co} the fiber core diameter and λ the wavelength of propagated light [13], [21].

Each image point of a speckle in an image plane results in an intensity distribution as illustrated on figure 2.22 for a diffraction. J_1 is the Bessel-function of the first-order. α is the angle of diffracted light that deviates from the normal direction and is defined as $\alpha = \frac{d_{co}}{2}$ The Fraunhofer-diffraction function I yields the intensity distribution of the airy disk for perpendicular incidence [21], [22].

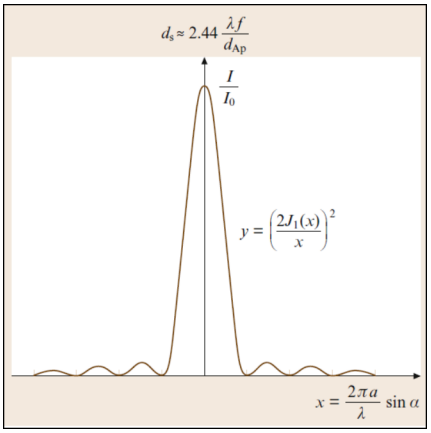

Figure 2.22: Speckle intensity distribution changing with the diffraction of a plane wave through a circular aperture [21].

2.5.4. Speckle Measurement Methods

The measurement setup determines whether *Subjective- Speckles* or *Objective-Speckles* are produced. Speckles as depicted on figure 2.23 are induced in free space and defined as the Objective-Speckles or Far-Field-Speckles.

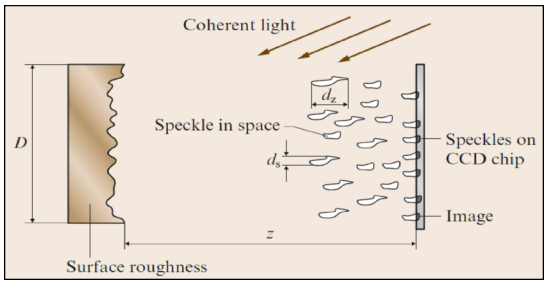

Figure 2.23: Formation of objective-speckles in free space [21].

A subjective-speckle-pattern as depicted on figure 2.24 is the recorded information of an imaging system that represents the major part of speckle occurrence by the fact of the commonly utilized CCD-cameras and digitalization of images.

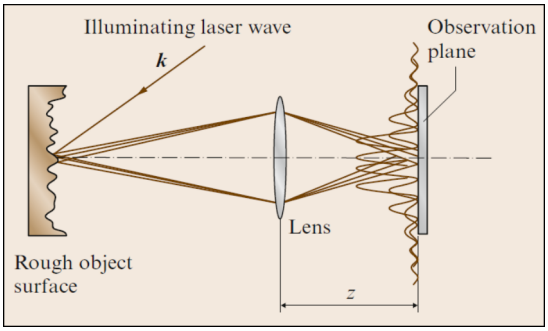

Figure 2.24: Formation of subjective-speckles by imaging system [21].

Subjective-speckles are formed by the superposition of complex amplitudes that originate from the scattered wavelets in the image plane. Light beams reflected by the illuminated part of the object surface are captured as points on the image, arising from the pixel structure of the CCD-array. Therefore, the properties of the speckles depend on the scattered light collected by the image aperture and the properties of the image recording device. The speckle size is set by the spatial frequencies passing through the lens system [21]. The amount of deformation is deducible by the information of the change in speckle surface geometry and speckle surface intensity distribution, by comparison of speckle-patterns before and after a deformation. The research field *Speckle Metrology* incorporates the analysis of

speckle-pattern properties by image processing methods and special measurement setups. 3D - deformation of objects under strain, pressure, temperature, vibration, static or dynamic loading is precisely measurable by observation and is known as *Nondestructive Testing* (NDT) or *Nondestructive Evaluation* (NDE)

Speckle Metrology is divided into two subdivisions:
The *Speckle Interferometry* (SI) describes the evaluation of changes in object surface intensity by the evaluation of the speckle intensity distribution and speckle phase inside a speckle-pattern, designated as means of first-order statistics.

Geometric changes of an object are grouped under *Speckle Correlation* and base upon the evaluation of the spatial structure of a speckle-pattern, the second-order statistics [21].

The previously described properties of speckles prove that the analysis of the speckle-pattern has to be realized by statistical methods and an appropriate imaging system for the exact speckle detection. The changes in the speckle-pattern by external influences are analyzed by graphical methods, based on statistical methods and correlation algorithms. The present project demonstrates a measurement method that is based on the detection of the amount of speckle contours in a defined region of interest in the speckle-pattern to measure the bending angle of a curved POF.

2.6. Analysis of Fiber under Curvature

2.6.1. General Considerations of Fiber Curvature

The following explanation of the fiber bending process is applied to a Multimode Step-Index Polymer Optical Fiber (MSI-POF). Several researches that describe the effects on modes and signal attenuation of a curved fiber were realized, as for example in [23] where a three-dimensional analysis of a bent fiber is described and the redistribution of light power and radiated power are illustrated. The effect of the bending radius and the number of turns on the signal attenuation are investigated in [23].

The influences of the bending radius on the power loss for different fiber core diameters is presented in [11]. The influence of number of turns, the bending radius, the core diameter and the cladding thickness is presented in [9]. The results of the previously mentioned researches demonstrate the knowledge base for the present research.

At the beginning, the process of bending or curvature of the fiber is distinguished in different kinds of bending.

Static Bending is existent when the fiber is installed in locations like buildings or industrial production lines. An almost constant loss of light intensity is induced in that condition. The knowledge about the amount of signal attenuation is important for the planning of the power budget to ensure a sufficient energy transport over a defined fiber length [6].

The *Minimum Bending Radius* defines the radius for that the fiber is bendable over a short-time range without mechanical destruction or partially damage [6].

Repeated Bending is the case of the fiber bending for several times over a defined time without being mechanically destroyed or damaged. Some fibers has the requirement to tolerate bends in numbers of 10^5 to 10^6 [6]. The fiber utilized in this present project posses a loss increment of less than 1 dB after 10.000 bendings [17].

Reel Change Bending arises particularly in drag chains in industrial installations [6].

Macrobends

Macrobends are assumed as bending radii that are significantly higher than the fibers core diameter. A decreasing bending radius generates an exponentially increasing radiation loss as depicted on the following figure 2.25. The signal loss of a bent Multimode-GI-POF is significantly higher than for a Multimode-SI-POF.

Figure 2.25 shows the exponentially formed signal loss in relation to the bending radius for a POF with a core radius $r_{co} = 0.49\ mm$ and describes the ray path for a bent fiber when the ray goes under refraction due to the curved fiber [6], [2], [15].

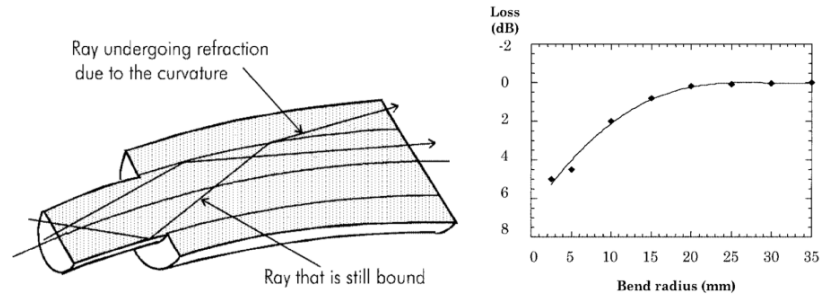

a) b)

Figure 2.25: Macrobends: a) Ray path in a curved fiber b) Power loss as a function of the bending radius, adapted from [2].

The signal loss during bending mainly depends on the ambient temperature ϑ, the bending radius R, the core diameter d_{co}, the refractive index of the core n_{co} and the wavelength λ of the transmitted light.

2.6.2. Effects on Numerical Aperture

The numerical aperture of a fiber with a constant length, bending radius and a descending bending angle is reduced under curvature. A signal attenuation on the fibers output is induced that proves the existence of a dependence between the light intensity of the fibers output and a bending angle, as depicted on the following figure 2.26.

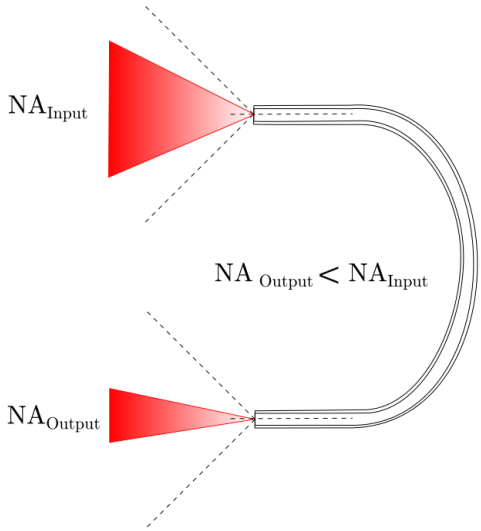

Figure 2.26: Reduction of numerical aperture of a curved fiber, adapted from [16].

The NA as a function of the bending radius and the fiber core radius is defined as:

$$NA_{bent} = \sqrt{n_{co}^2 - n_{cl}^2 \cdot \left(1 + \frac{r_{co}}{R_{bent}}\right)} \tag{2.18}$$

where r_{co} is the core radius of the fiber and R_{bent} the bending radius. The quantities of the fiber parameters utilized in the present project are as follows:

$$NA = 0.5, n_{co} = 1.49, n_{cl} = 1.417, r_{co} = 0.49\ mm, R_{bent} = 20\ mm$$

The insertion of the values in equation (2.18) for the numerical aperture of a bent fiber leads to:

$$NA_{bent} = \sqrt{1.49^2 - 1.417^2 \cdot \left(1 + \frac{0.49\ mm}{20\ mm}\right)} = 0.40 \tag{2.19}$$

The previous calculation of the NA in (2.19) proves the decrease of the numerical aperture for a reduced bending radius. The amount of light intensity on the fiber output under curvature is mainly influenced by the core diameter and the refractive indexes of the core and cladding [24].

2.6.3. Effects on Modes

The analysis of light rays under curvature is usually performed by the Ray-tracing method. The cross-sections of the fiber are considered before and after bending for

a calculation of guided ray paths inside a curved fiber. The propagation sense of guided light rays is in direction of the core-cladding axis in a straight fiber which serves as a reference axis for the calculation of guided rays inside the fiber core [6].

The bending process leads to a rotation of the core-cladding axis by the amount of the bending angle α. Guided light rays still tend to propagate in the same direction as in the condition of the relaxed fiber and mode conversion occurs. Guided modes are transformed into *Radiation Modes* and are absorbed by the cladding or leave the core and convert into *Cladding Modes*, as previously described in section 2.2.7. The ray path inside the bent fiber core is illustrated on the following figure 2.27 [6].

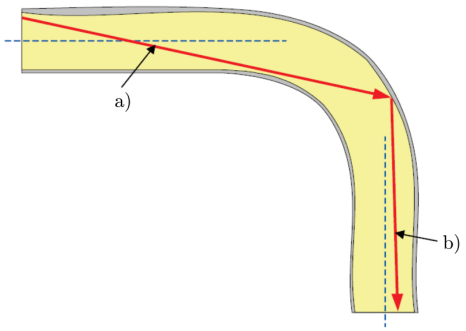

Figure 2.27: Ray path in a curved fiber a) Propagation direction before bending b) Altered propagation direction after bending, adapted from [6].

The distribution of modes at the end of the curved fiber with a large NA is demonstrated on the following figure 2.28. Outer modes own a stronger tendency to convert into radiation modes for lower numerical apertures [6].

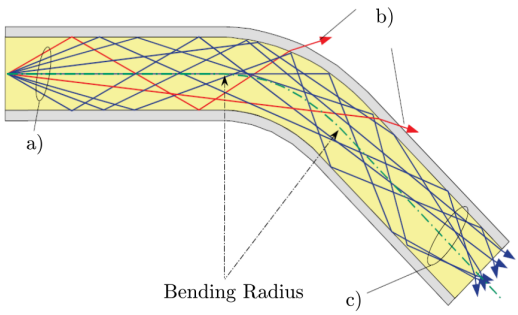

Figure 2.28: Detailed ray path in a curved fiber: a) Launched light rays b) Rays that exceed the critical angle of total reflection behind the bend c) Guided rays after the bend, adapted from [6].

Theoretical Approach of the Ray Path within a Curved Fiber

A theoretical approach for the calculation of the transmitted energy in a bent fiber was realized in [9]. The calculation is based on the Ray-tracing model and under assumption of a finite cladding thickness, thus light can travel into the cladding without beeing absorbed or totally lost.

The ray theory describes the ray tracing characteristics as follows:
A Mode reaches the core-cladding interface and is divided into a *Refracted Mode* and a *Cladding Mode* or *Tunneling Mode*. The refracted mode, produced at the outer core-cladding interface is depicted as '1' on the following figure 2.29. The cladding mode travels into the inner core-cladding interface, depicted as '2' on the following figure 2.29 [9].

The Mode characterized by a thicker line, traveling inside the core on figure 2.29 is illustrated under assumption that the cladding thickness is finite. That assumption forces partially refracted or radiated modes to be absorbed by the cladding on the core-cladding interface. Reflected modes return back into the core under conditions of a real fibers. The number of refracted and tunneled rays grows with 2^n for a n-times-looped fiber [9].

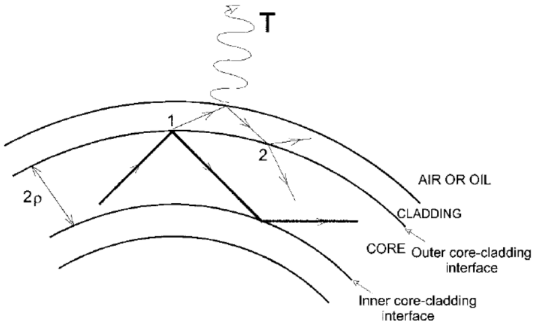

Figure 2.29: Ray path in a curved fiber of finite cladding thickness: 1) Refracted mode 2) Cladding mode, adapted from [9].

The transmission energy T_r of the refracted modes is based on the classical Fresnel's coefficient in scalar approximation. The transmission energy of the cladding modes is low, by $T_t \approx 10^{-8}$, in comparison to the transmission energy of the refracted modes T_t and therefore $T_t = 0$ is assumed. The detailed calculations of these transmission energies are presented in [9]

Calculation of Number of Modes with Parameters of current Application

The quantities of the fiber parameters, utilized in the current project are as follows:

$$NA = 0.5, n_{co} = 1.49, n_{cl} = 1.417, r_{co} = 0.49\ mm, R_{bent} = 20\ mm$$

The normalized frequency V for a relaxed fiber is derived as follows:

$$V = \frac{2 \cdot \pi \cdot r_{co}}{\lambda} \cdot NA = \frac{2 \cdot \pi \cdot 490\ \mu m}{0.6328\ \mu m} \cdot 0.5 = 2432.65 \tag{2.20}$$

The number of modes is significantly reduced by the fact of the reduced numerical aperture, as proven in equation (2.19) for the numerical aperture of the bent fiber. The diminished normalized frequency V for the reduced $NA = 0.4$ is calculated as follows:

$$V = \frac{2 \cdot \pi \cdot r_{co}}{\lambda} \cdot NA = \frac{2 \cdot \pi \cdot 490\ \mu m}{0.6328\ \mu m} \cdot 0.4 = 1946.11 \tag{2.21}$$

The number of modes for the relaxed fiber is calculated as follows:

$$N = \frac{V^2}{2} = \frac{2432.65^2}{2} = 2.96 \cdot 10^6 \tag{2.22}$$

The number of modes for the bent fiber is calculated as follows:

$$N = \frac{V^2}{2} = \frac{1946.11^2}{2} = 1.9 \cdot 10^6 \tag{2.23}$$

The previous calculations of the numerical aperture (2.19), the normalized frequency (2.20) and the number of modes (2.23) prove that a decreasing bending angle leads to a reduced numerical aperture and secondly a descending number of modes.

$$R_{bent}\ \downarrow \Rightarrow NA\ \downarrow \Rightarrow V \downarrow \Rightarrow N \downarrow$$

2.6.4. Effects on the Amount of Speckles

The amount of speckles and its intensity distribution varies in dependence to the amount of curvature. The measurement results proved that the amount of speckles

and the speckle-pattern intensity reduces for a growing bending angle, by the fact of a decreasing numerical aperture.

The following equations demonstrate the influence of the curvature on the amount of speckles. The total amount of bright and dark speckles in a defined speckle pattern array is defined as:

$$N_{pattern} = \frac{NA^2 \cdot d_{co}^2}{\lambda^2} \tag{2.24}$$

under the utilization of the physical quantities of the present project:

$$N_{pattern} = \frac{NA^2 \cdot d_{co}^2}{\lambda^2} = \frac{0.5^2 \cdot 980^2\ \mu m}{0.6328^2\ \mu m} = 599 \cdot 10^3 \tag{2.25}$$

The amount of speckles in a defined speckle-pattern area for the reduced $NA = 0.4$ of the bent fiber is calculated as follows:

$$N_{pattern} = \frac{NA^2 \cdot d_{co}^2}{\lambda^2} = \frac{0.4^2 \cdot 980^2\ \mu m}{0.6328^2\ \mu m} = 383.7 \cdot 10^3 \tag{2.26}$$

Equation (2.18) of the numerical aperture under curvature, equations (2.24) and (2.26) prove the reduction of the amount of speckles for a decreasing bending radius.

$$R_{bent}\ \downarrow \Rightarrow NA\ \downarrow \Rightarrow N_{pattern} \downarrow$$

2.6.5. Effects on inner Light Intensity Distribution

The mode distribution on the fibers end face during curvature is explained in this section, based on research results of [24].

The incident ray crosses the whole section in a straight fiber whereas in a bent fiber it crosses only the half of the cross section, as depicted on figure 2.30. The power distribution of the inner fiber core changes during the propagation path and concentrates on one side of the fiber over the length. The concentration of light at the end face of the fiber is analyzable graphically by image processing techniques.

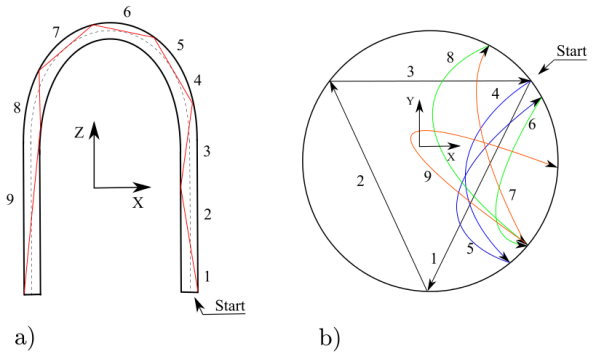

Figure 2.30: Intensity distribution in a a curved fiber: a) Ray Path b) Light intensity distribution over fiber cross section at different length steps, adapted from [24].

The light intensity diminishes in a defined area on the fibers end face with an ascending bending angle, as described in [24] and [25]. The position of the energy concentration field on the fibers end face is constant. For a determination of the light intensity in relation to the bending angle, a defined region of the fibers end face can be observed graphically. The simulation results of [24] for the energy distribution on the fibers end face for different bending radii are illustrated the following figure 2.31. As observable, the field intensity at a constant position declines with an decreasing bending radius.

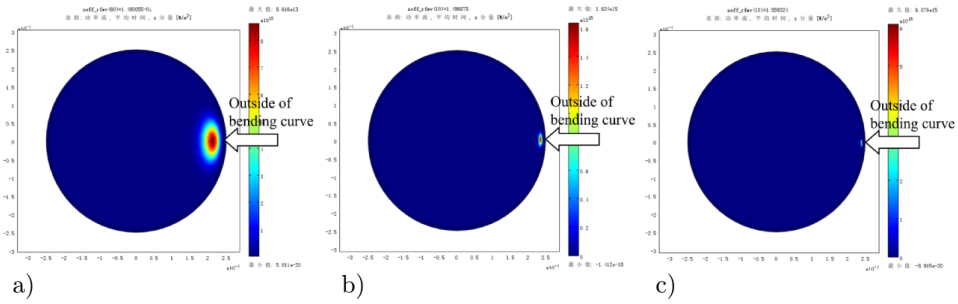

Figure 2.31: Field distribution of the fundamental mode versus bending radius by simulation: a) $R_{bent} = 5\ m$ b) $R_{bent} = 0.05\ m$ c) $R_{bent} = 0.005\ m$, adapted from [24].

The theoretical and simulated results are proven by a practical demonstration in [24]. 2.32. The fiber was maintained in a curved position by epoxy glue at a bending radius of $R_{bent} = 5\ mm$, as illustrated on figure 2.32a. Subsequently, the fiber was cut and polished in the middle of the bending arc as demonstrated on 2.32b thus, the energy distribution on the fibers end face was observable with a microscope, as illustrated on 2.32c.

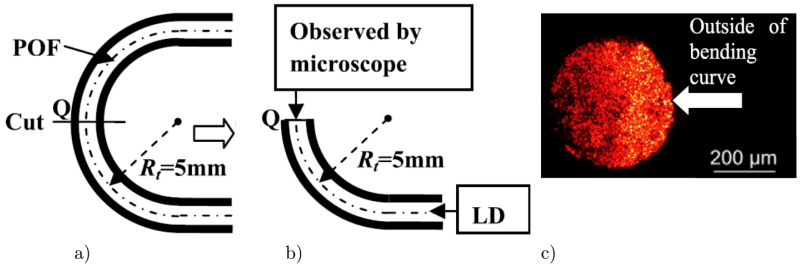

Figure 2.32: Experimental setup to detect field distribution on fiber end face: a) Fixation of bent fiber in epoxy glue b) Cut of fiber to analyze end face c) Microscope image of speckle-pattern at fiber end face, adapted from [24].

2.6.6. Effects on Light Intensity for Multiple Looped Fiber

The transmission loss T_t represents the major part of signal attenuation for a n-looped fiber, as previously described. That part of energy loss is comparatively high for a low amount of loops. Refraction modes lose most of their energy after several loops, due to the propagation path length. Afterwards, the secondary losses such as cladding modes or tunneling modes are detectable. This physical effect explains the disproportional signal attenuation in relation to the amount of loops [9].

Signal Attenuation as a Function of Amount of Loops

The following figure 2.33 represents the output power over the wavelength for different amounts of fiber loops. As can be seen, the signal attenuation between $n = 5$ and $n = 10$ loops is not the doubled as expected. The signal attenuation in relation to the amount of loops is nonlinear in the region from $n = 1$ to $n = 10$, as depicted on figure 2.33. The small wavelength dependence is referred to tunneling rays and core-refractive index dependence over the wavelength $n_{co} \equiv n_{co}(\lambda)$ [9].

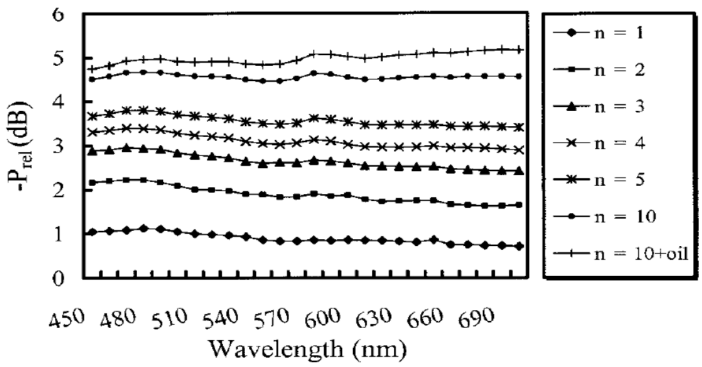

Figure 2.33: Output power as a function of wavelength and number of fiber turns at a bending radius $R_{bent} = 5.1\ mm$ and core diameter $d_{co} = 1\ mm$ [9].

The attenuation after $n = 8$ for a bending radius $R = 8\ mm$, demonstrates continuity on figure 2.34. The parameters of the fiber under test are $d_{co} = 980\ \mu m$, $cladding\ thickness = 10\ \mu m$, $n_{co} = 1.492$, $n_{cl} = 1.402$.

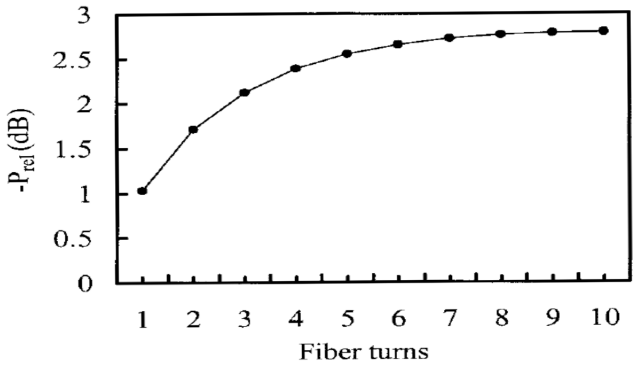

Figure 2.34: Output power loss in relation to amount of fiber turns [9].

Signal Attenuation as a Function of Amount of Fiber Loops and Bending Radius

After $n = 5$, only slight changes in the signal attenuation for bending radii higher than $R = 5.10\ mm$ are detectable on the following figure 2.35. The attenuation for a descending bending radius rises strongly by an growing amount of turns. The sensitivity of a curvature sensor consisting of a looped fiber is improved by the the reason of the amplified attenuation.

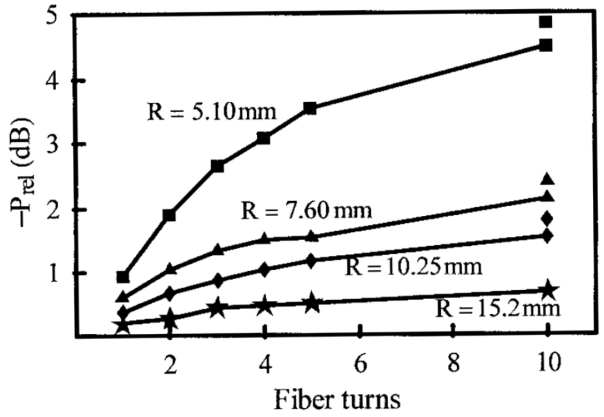

Figure 2.35: Output power loss in relation to amount of fiber turns for different bending radii [9].

Signal Attenuation of Looped Fibers of different Manufacturers

Figure 2.36 and figure 2.37 represent the relation between the signal attenuation of looped fiber of different manufacturers in relation to the bending radius. A

Standard POF PFU-CD-1000 characterized by a commonly high NA is utilized in figure 2.36.

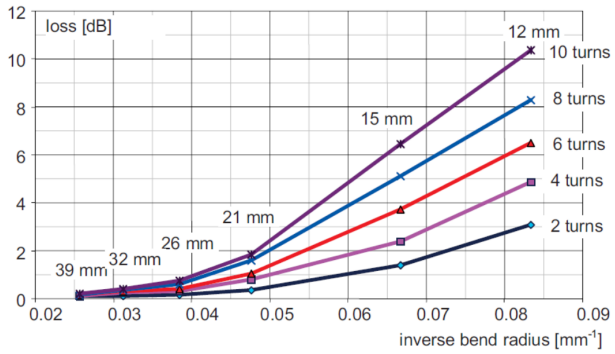

Figure 2.36: Output power loss versus inverse bending radius for different amount of fiber turns of a PFU-CD1000 [6].

In figure 2.37 a POF NC-1000 characterized by a relatively small NA was utilized. The POF NC-1000 owns a stronger signal attenuation in comparison to the PFU-CD-1000. The signal attenuation grows significantly with the number of turns at a constant bending angle. Generally, the signal attenuation rises strongly for a growing number of turns and bending angle.

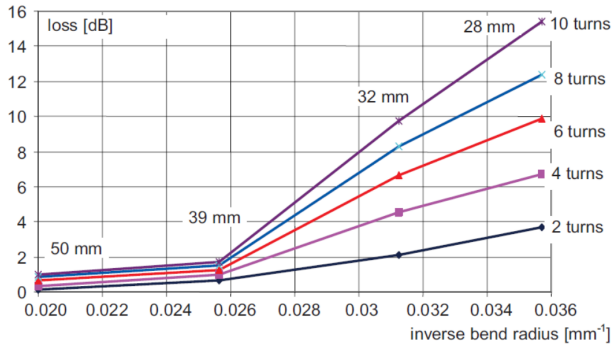

Figure 2.37: Output power loss versus inverse bending radius for different amount of fiber turns of a NC-1000 [6].

2.6.7. Repeated Curvatures in Long-Time Range

A repeated bending test of a POF over a long-time range was performed in [12] and the results revealed that the signal attenuation rises rapidly with a diminishing bending radius over the time, as depicted on the following figure 2.38. A lower bending radius generates higher signal attenuation for several repeated bendings. A significant attenuation after 1000 bends at a bending radius of 5 *mm* is noticed.

A bending radius of 10 mm has no significant effect on the signal attenuation as demonstrated on figure 2.38.

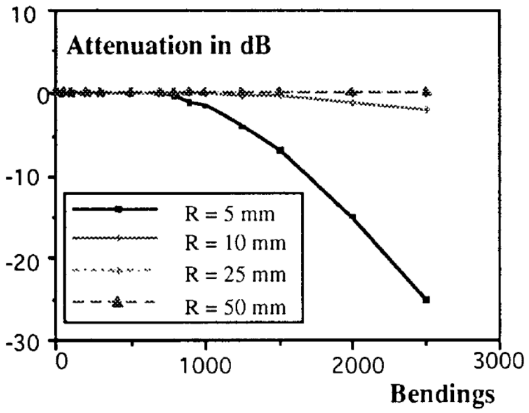

Figure 2.38: Signal attenuation as a function of the bending radius and amount of repeated bendings [12].

2.6.8. Repeated Curvatures in Short-Time Range

The elasticity and mechanical memory of the fiber cause deviations of signal response in high frequent repeated bending operation. Assuming the following procedure:

A fiber is curved in one direction to an angle α and rested for some seconds and is subsequently turned back to the relaxed position. After a time lapse of several seconds, the process is repeated. Both signal responses for the same bending angle α represent a deviation, traced back to the mechanical memory of the fiber. This effect was proven in [12] and is illustrated on figure 2.39, where the repeat accuracy for a bending radius of 10 mm was examined.

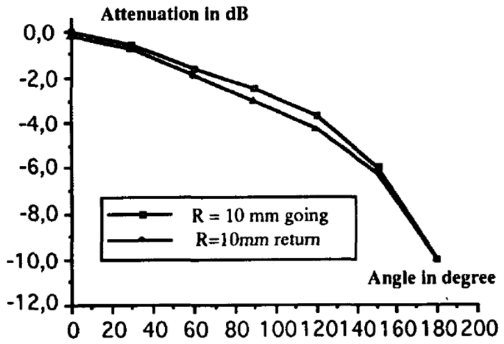

Figure 2.39: Signal attenuation as a function of the bending radius in bending-straightening mode [12].

2.6.9. Practical Implementations based on Curvature Analysis

The previously described physical effects on a curved fiber serve as a knowledge base for the design of the experimental setup.

The speckle pattern analysis for the determination of the bending angle of the curved fiber, are performed by the knowledge of the research results revealed in [24]. The speckle-pattern that is projected on the fiber end face changes visible during curvature and can be analyzed graphically by the observation of a defined region of interest of the speckle-pattern.

The signal attenuation is significantly amplified by looping the fiber for several times. This effect is utilized as an adjustable parameter for the curvature sensor sensitivity. A higher signal attenuation is generated for a looped fiber during curvature and therefore, the measurement of signal in relation to the bending angle is more precise by the fact of the stronger attenuation.

2.7. Relevant Research and State of the Art

2.7.1. Technical Evolution of the POF

The demand of POFs raised rapidly in the last decades according to the reduction of impurities in the material by an improved manufacturing process and material compositions. The fiber bandwidth increased by the simultaneous diminish of signal attenuation. Sensors based on POF, find application in environmental, biological and chemical research, structural health monitoring, medicine, civil engineering, aeronautics, aerospace and automobile industry [26], [14], [15], [2]

The physical characteristics such as lightweight, electromagnetic interference immunity, chemical resistance, mechanical robustness and flexibility made the POF more attractive for industrial applications. Manufacturing of the POF is characterized by low installation and linking effort arising from a high numerical aperture, low bending radius and large diameter. Comparatively low expenses for material and elementary development equipment make the processing of the POF feasible [2], [1].

2.7.2. Overview of POF - Based Sensors

The POF-based sensors utilized in industrial applications are frequently applied for gauging physical related parameters such as strain, pressure, stress, vibration, current, rotation, displacement, temperature, leakage, bending angle, biomedical parameters, deformation, [2], [1], [27], [28], [26], [15], [6], [14]. Special applications such as acceleration measurement [29], determination of surface roughness [30], determination of thickness of a transparent plate [31] or glass damage detection [6] were developed. For a better overview, POF-based sensor examples and their working principle in industrial applications are presented:

Strain Sensor

The physical measuring parameter is often transformed in another quantity to be measured as realized in [24] where the strain applied on a elastic belt is transformed into a curvature of the fiber by special fiber arrangement. A dependence between the strain and the signal attenuation is achieved by this method.

Force Sensor

A POF is arranged in 20 loops over a hollow flexible cylinder. Lateral forces applied on the cylinder cause a deformation of the cylinder and a signal attenuation on the fiber output. The applied force causes a displacement and can be physically transformed in pressure, force or displacement, as presented in [10]. The signal attenuation is disproportional to the amount of loops and a non-linear characteristic of the attenuation as a function of the deformation of the cylinder was revealed.

Wing-Deformation Sensor

A rotor wing deformation sensor of wind power plants was developed by *Photon Project* and supported by *Bavarian Research Foundation* is presented in [6]. The POF is fixed on the rotor wing and a phase modulated signal is propagated through the fiber. A wing deformation provokes a phase shift between the modulated reference signal and the curved POF mounted on the wing. A linear characteristic of the deformation as a function of the phase shift is revealed.

Temperature Sensor

A POF-based temperature sensor consists of a macrobend loop and its sensitivity is adjusted by the radius of the macrobend as described in [18]. The signal loss raises with an increasing temperature and its sensitivity is adjusted by the bending radius. A similar principle with multiple macrobend loops for the temperature measurement is presented in [19]. Both researches revealed the dependence of bending losses with the temperature and bending radius.

Humidty Sensor

A POF-based humidity sensor is realized by the analysis of the refractive index alteration by absorbed water of the fiber core. Certain molecules of the polymer material swell up when the fiber absorbs water and the change of the refractive index leads to a different signal attenuation on the fiber output [6].

The major part of the POF-sensors is based on light intensity modulation as demonstrated by the preceding sensor examples. The loss in light intensity is often proportional to the physical related measured parameter which simplifies the measurement of the signal response. However secondary losses caused by absorption, scattering and radiation are included in the resulting measured parameter and represent a negative influence on the accuracy and reliability of the sensor [1].

The signal on the Multimode-fiber output can be analyzed with a CCD-camera instead of a photodiode or phototransistor as realized in the following sensor examples. A granular speckle-pattern can be captured and analyzed with digital image processing techniques to determine the change of physical parameters as described in the following section.

2.7.3. POF - Sensors based on Speckle-Pattern Analysis

Modal Noise occurs only in Multimode-fibers and is also known as *Mode-Distribution Noise* or *Speckle-Noise*. Each light ray contains a own power distribution over the fiber cross section. The power distribution between light rays are defined as *Speckle-Pattern* and it varies with external changes such as temperature, wave-

length of light source and vibration while the allover intensity of the speckle-pattern remains unchanged [2], [6]. Several image processing techniques for the analysis of the speckle-pattern were developed as presented in this section.

Fiber Elongation Sensor

A strain gauge for the determination of the fiber elongation in the μm-range is based on a self-developed correlation factor between two speckle-pattern images [20]. A comparison of the speckle-patterns intensity distribution before and after deformation generate a spatial correlation factor defined by a given formula. A decreasing correlation factor represents a lower similarity between the images and demonstrates a higher grade of elongation. The measuring method is characterized by low computing effort, adaptability, high precision and reliability.

Temperature Sensor

The spatial correlation calculation between two speckle-pattern images for temperature measurement is described in [13] and compared with the *Mean Speckle Intensity Variation* (MSV) image processing technique. A subsequent image is subtracted from a reference image and afterwards integrated. Both techniques are characterized by a certain adaptability and high precision.

Vibration Sensor

The measurement of vibration by the application of the speckle-pattern image difference technique is presented in [32] where the variation of the speckle-pattern intensity distribution is examined. The technique is characterized by computational low effort and simplicity in implementation.

Specklegram Sensor

A wavelength domain multiplexed fiber specklegram sensor is presented in [33] that analyzes the influence of the wavelength on the signal response for a POF Multimode-Step-Index Fiber under perturbation. Green light with a wavelength of 532 nm and red light with a wavelength of 632.8 nm are coupled together over an optical 50/50 coupler into a fiber of 1 m length and a diameter of 980 μm, as

depicted on figure 2.40. A CCD-camera generates speckle-pattern images with a resolution of 400 x 400 pixels on the fibers end face.

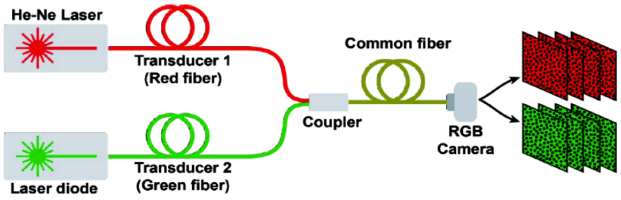

Figure 2.40: Specklegram measurement setup [33].

The images are scaled to its mean value to compensate differences in light energy between the color channels red, green and blue. The employment of an RMS-contrast to the images improved the visibility of the speckles. The specklegram of the red channel demonstrated a better contrast than the green channel as illustrated on figure 2.41

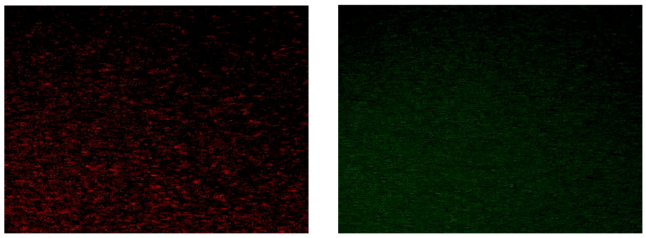

Figure 2.41: Equalized specklegrams of a) Red channel b) Green channel [33].

The images are analyzed with the speckle-pattern image difference technique for each color channel and subsequent images before and after perturbation are compared. The image differences for each channel was recorded and analyzed as depicted on figure 2.42.

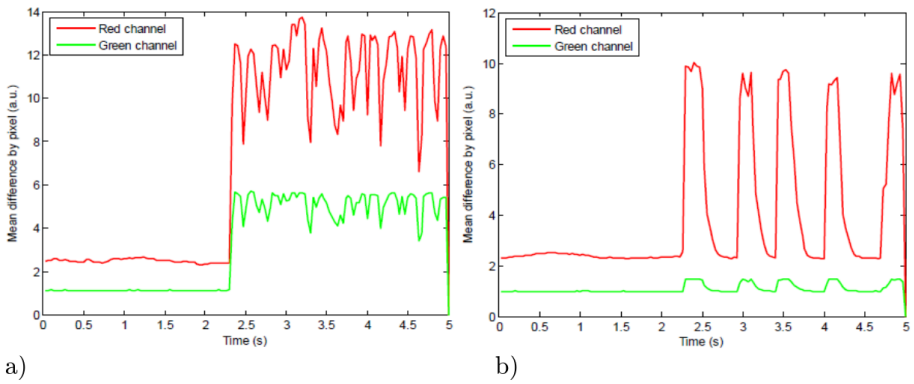

Figure 2.42: Signal responses of specklegram sensor for perturbation on a) The common fiber and b) The fiber of red light channel, adapted from [33].

The experimental results revealed a higher sensitivity for the red channel under perturbation in comparison to the green channel. The utilization of only one CCD-camera facilitates the separated analysis of three different specklegrams. The image difference technique is applicable for varying ambient temperatures by the arbitrarily chosen reference image.

Force Sensor

A statistical mode sensor in combination with an *Artificial Neural Network* (ANN) of *Multilayer Perceptron* (MLP) structure is presented in [34]. Red light provided by an LED is propagated through a Multimode-Step-Index Silica Fiber, fixed between two metal plates. The actuation of a force on the metal plate generates a homogeneous force distribution on the fiber and induces a signal attenuation. The signal response at the fibers end face is captured by an objective lens with a 20 x zoom and recorded by a CCD-Camera.

The resulting image is a speckle-pattern in form of a illuminated circle over a black background is shown on figure 2.43. The diameter of the speckle-pattern changes in relation to the applied force on the metal plates. The applied force is represented by weights from 0.5 kg to 3 kg, applied in steps of 0.5 kg and from 1 kg to 6 kg, applied in steps of 1 kg. A linear characteristic of the applied weight as a function of the speckle-patterns diameter was measured for both cases as depicted on figure 2.44.

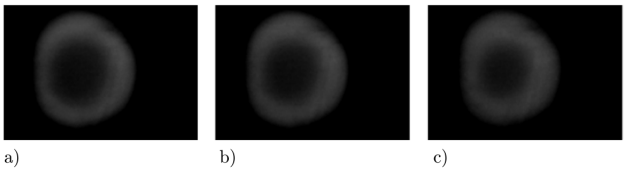

Figure 2.43: Speckle-patterns for different loads: a) Relaxed b) 0.5 c) 3 kg, adapted from [34].

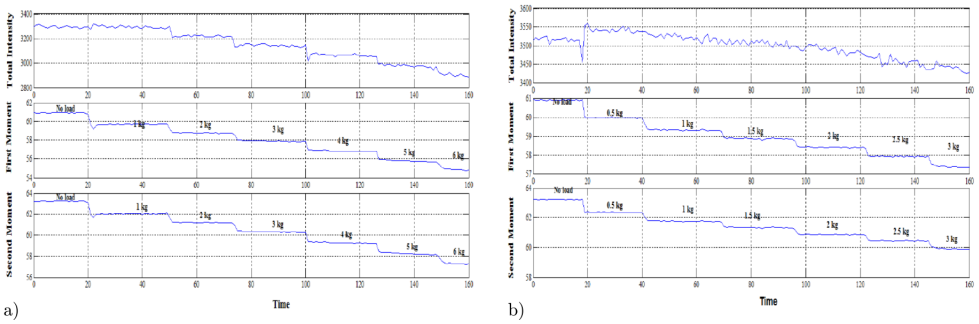

Figure 2.44: Signal responses as a function of weight in ranges a) from 0 kg to 3 kg and b) from 0 kg to 6 kg, adapted from [34].

Statistical first and second moments where applied on the signal response. The results of the first and second moments served as an input for an Artificial Neural Network with a MLP-Structure that is capable to predict further values of an potentially applied force. Different types of MLP-Algorithms were applied and their *Mean Square Errors* (MSE) compared. The Algorithm named *One Step Secant* showed a Test-MSE of only $2.25 \cdot 10^{-2}$ in comparison to the commonly known *Resilent Backpropagation*-Algorithm with a Test-MSE of $3.71 \cdot 10^{-2}$. The results revealed that the ANN improved the signal response significantly as shown on the following table.

Signal Input	**Test Mean-Square-Error**
First Moment	0.1825
Second Moment	0.2965
ANN with First and Second Moment as input	0.0510

Table 2.1: Measurement results of force sensor based on speckle-pattern image processing, [34].

Images of speckle-patterns are normally distorted and sensitive for external disturbances such as temperature, mechanical shocks or vibration applied on the fiber. An ANN makes the sensor adaptable to external disturbances and changes in the characteristic curve of the signal response by the adjustment of its parameters.

Physical parameters such as deformation, temperature or mechanical waves are produced by the human body and utilized for the determination of the health state of a human person. POF-based sensors found wide application in the field of

health monitoring. A sensor example of an arterial pulse and respiration sensor, based on the graphical analysis of speckle-pattern is given.

Arterial Pulse and Respiration Sensor

The properties of a speckle-pattern are changed under mechanical perturbation of a light guiding fiber. This fact is utilized in [35] for the determination of the arterial pulse and the respiratory rate of a patient by the graphical analysis of speckle-pattern variations.

Arterial pulse is caused by the heart that pumps blood into the arteries and is detectable by the fingers on the wrist or neck of a person. The manual procedure is substituted by an attached fiber on the wrist of a person and the graphical analysis of the resulting variations in the speckle-pattern, as depicted on figure 2.45. A headband is provided with the fiber and weared on the wrist of the patient.

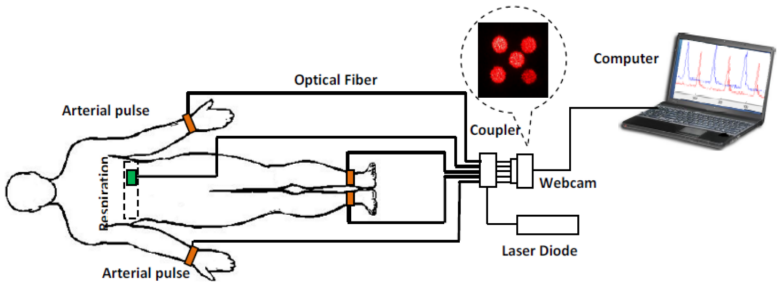

Figure 2.45: Measurement setup of arterial pulse and respiration rate sensor, adapted from [35].

The respiration of a person causes visible variations in the chest diameter by the expansion of the thorax and can be utilized for the determination of the breathing rate. The POF is formed in a 'U'-shape with a radius of 5 mm and fixed on an elastic cord surrounding the chest. The respiration induces a change of the 'U'-shaped POF bending radius and varying properties of the speckle-pattern. The speckle image difference technique was applied, where the correlation between two subsequent images before and after perturbation is calculated and set in relation to the breathing rate, as depicted on figure 2.46 and 2.47.

The signal response of the arterial pulse profile is regular in frequency and inconstant in the amplitude height as shown in figure 2.46. The averaged error of

$\pm$ 0.15 BPM in comparison to the palpation pulse measuring technique is considered as imperceptible. The measuring results of the chest respiratory prove a regularity in frequency and constancy in amplitude as illustrated on figure 2.47.

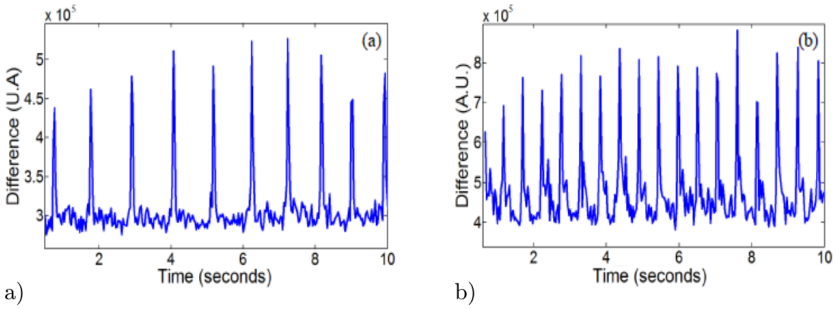

a) b)

Figure 2.46: Signal output of blood pulse measurement at a) 61 BPM and b) 78 BPM, adapted from [35].

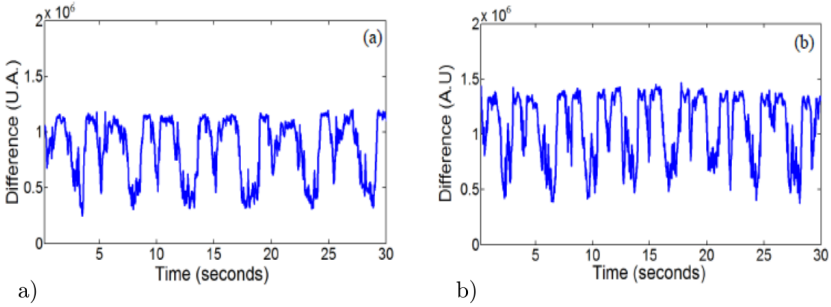

a) b)

Figure 2.47: Signal output of respiration rate measurement at a) 12 BPM and b) 17 BPM , adapted from [35].

The simultaneous evaluation of two speckle-patterns is performed and the variations of the observed regions marked as 'A','B' and 'C' on figure 2.48.

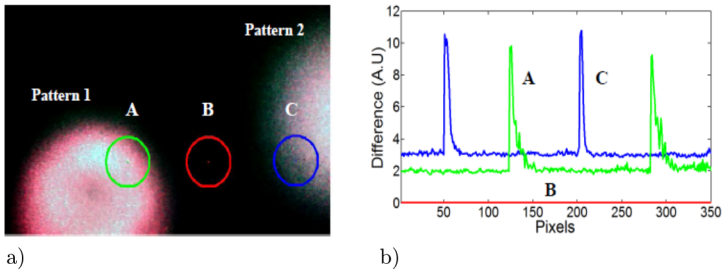

a) b)

Figure 2.48: a) Two speckle-patterns recorded by web cam b) Output signal of image processing, adapted from [35].

The widespread application of the POF-based sensors in the medical field includes sensor principles that are capable to measure angular movement of human joints by the determination of its curvature, as presented in the following sections. An

overview over POF-based curvature sensors and their working principle is given, followed by special curvature sensors and curvature sensors that are utilized for the human joint movement analysis.

2.7.4. POF Curvature Sensor Principles

The curvature sensors based on light-intensity modulation consist of Singlemode or Multimode fibers and the bending of the fiber induces a signal attenuation that is analyzed and set in relation to a physical parameters.

Sensors based on light intensity modulation can be separated in five different subcategories related to their function: fiber displacement, shutter modulated, reflective, transmission loss and evanescent field while the transmission loss function is treated and applied in the present work [1].

Three commonly applied curvature sensors structures based on light intensity modulation for transmission loss are dependent on their measuring principle. The fiber in transmission mode is characterized by the entering of light on the input and outgoing on the opposite output as depicted on figure 2.49a.

The folded fiber fiber in transmission mode is constructed as the former version but folded for the amplification of the signal attenuation by two bending points as depicted on figure 2.49b.

The fiber in reflection mode requires a 50/50 optical coupler which means that the light intensity is distributed over two fibers instead of one. The light enters the fibers input via optical coupler, reflects on its end face and is received by the second fiber of the 50/50 coupler as depicted on figure 2.49c [8].

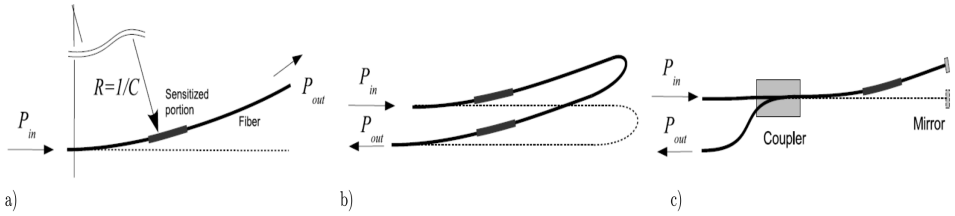

Figure 2.49: Curvature sensor based on transmission loss: a) Transmission mode b) Folded fiber in transmission mode c) Reflection mode [8].

An amplified signal attenuation is achieved by the manual manipulation of the fiber representing a higher sensor sensitivity. The main manipulation techniques for fiber sensitizing are explained in the following section.

2.7.5. Sensitivity Improvement Techniques for POF - Curvature Sensors

The sensitivity of a light intensity modulated POF-sensor is variable by the mechanical manipulation of the fiber core leading to a higher signal attenuation on the fiber output during curvature. The method is considered as an adjustable parameter of the sensor sensitivity.

The manipulation methods are divided into the *destructive* and *non-destructive* manipulation methods where the former method predominates in the current sensor applications.

The jacket and cladding of the fiber are removed, characterized by a visible fiber core in the case of the destructive method. The fiber core is manipulated manually by several kinds of manufacturing techniques that cause different appearances, as depicted on figure 2.50. The precision of the mechanical manipulation is important for the constancy of the sensor sensitivity over the entire bending angle range. Chemical and plasma based etching methods are described in [14]. A special drilling technique with the aid of a special high precision driller was utilized in [5]. A manual cutting method with the aid of a metallic molding tool is presented in [26]. A high quality and reliable technique based on a CO_2-Laser is presented in [36]. The creation of the cavities can also be made by grinding, heat forming or molding as proposed in [37].

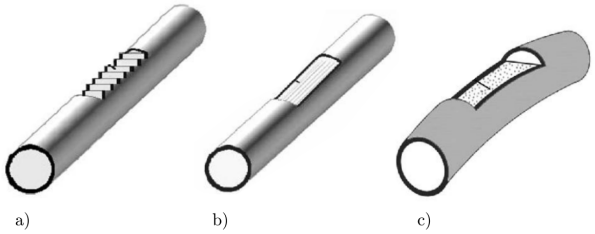

Figure 2.50: Types of sensitive zones: a) Serrated surface b) Longitudinal grain c) Random grain, adapted from [37].

The sensitized zone, characterized by ripples or cavities, is the most utilized form in the field of curvature sensors besides the side- or radial polished method [38]. The imperfections provoke a change of the light wavelets incident angle, resulting in a summation of partial internal reflections, reverse reflections and double refractions [7]. These physical facts are utilized in [5] to distinguish the polarity of bending directions as depicted on figure 2.51.

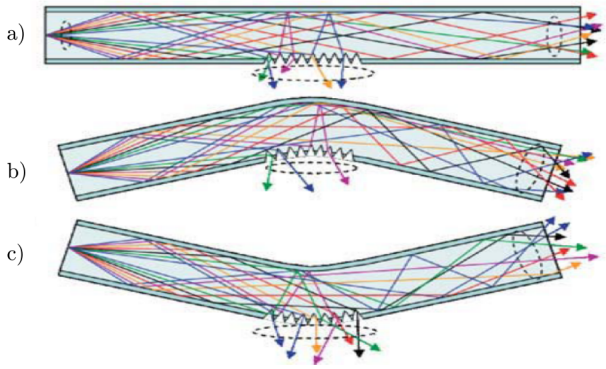

Figure 2.51: Detection of bending direction: a) Relaxed fiber b) Negative bend, less scattered rays c) Positive bend, more scattered rays [6].

The signal response on the fiber output increases for negative bending angles and declines for positive bending angles according to light coupling effects during curvature, as illustrated on figure 2.52.

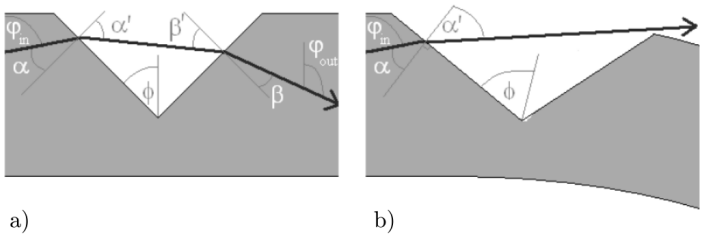

Figure 2.52: Ray path for different bending directions a) Negative bend: Light is coupled back to fiber core b) Positive bend: Light escapes the fiber core, adapted from [7].

A detailed research and its results about the influences of the sensitive zone such as abrasion angle, the location angle, the displacement and the V-groove depth on the signal attenuation are presented in [7]. The main parameters are depicted on figure 2.53.

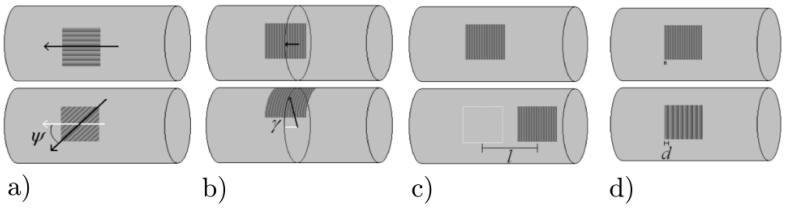

Figure 2.53: Parameters of sensitive Zone: a) Abrasion angle b) Location angle c) displacement d) V-groove depth, adapted from [7].

The imperfections limit the mechanical flexibility of the fiber as reported in [5], where the fiber core cracked at a bent angle of +140°.

The second non-destructive method is characterized by looping the fiber for several times or providing it with plastic rods where the former method is mainly utilized. A displacement sensor consists of several fiber loops surrounding a hollow cylinder as presented in [10]. The looping of the fiber as a macrobend is utilized in [15] and [18] as an amplification and sensing factor for the measurement of temperature. The sensitivity of a curvature sensor for respiratory measurement was amplified by looping of the fiber, as described in [39].

Plastic rods are utilized in [38] to amplify the bending losses by an increase in bending points over the fiber length, as illustrated on figure 2.54a. The measurement revealed that the sensor sensitivity is amplified proportional to the number of rods. The raise is noted as 0.11 % for each rod.

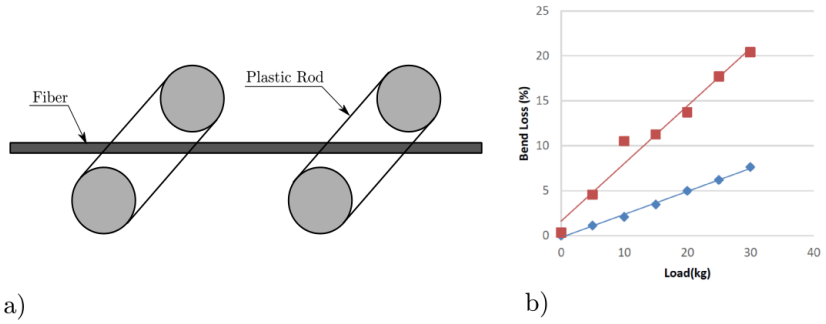

a) b)

Figure 2.54: Improvement of sensitivity: a) Plastic rods attached on fiber b) Signal attenuation as a function of load, adapted from [40].

Comparison of Sensitizing Method

The destructive manipulation technique is efficient as researches revealed. The four main degrees of freedom for the adjustment of the sensor sensitivity such as abrasion angle, location angle, displacement and V-groove depth are reported in [7]. The requirements on the sensing elements on the fiber output are less, by the amplification of the signal attenuation which is considered as an advantage of this sensitizing method. The fiber is damaged by the manipulation process thus the robustness and durability are reduced. That fact has to be considered in applications where the fiber acts as a curvature sensing element. The effort and precision are comparatively high in comparison to the price of the fiber and the reproduction of this method is difficult.

The looping of the fiber is advantageous by the fact of being non-destructive. The fiber is arranged in several loops for the signal attenuation and lateral forces, strain or expansionary movements can be transformed into curvature movements by intelligent fiber arrangement. The type of looping and amount of turns can be adjusted to the specific application for the a desired signal output. Several looping arrangements are described in [1].

The looping of the fiber can be extensive in size and demonstrates a disadvantage in some cases because the length of the fiber is increased. A comparatively high amount of turns must be realized to reach the same attenuation amplification as in the case of the destructive manipulation method.

Sensor applications in the field of human joint movement analysis that made advantage of the destructive sensitizing method are described chronologically in the next section.

2.7.6. POF - Curvature Sensors provided with Sensitive Zone

One of the fist sensors based on light intensity modulation, provided with a sensitive zone, was invented in 1996, as reported in [25]. A higher sensitivity and the bending direction detection of a metallic beam were realized by the mechanical manipulation of the fiber core.

The POF-based curvature sensor consisting of a side-polished fiber for the measurement of arm movements is described in [41] and the information about the bending directions of the arms was utilized for a gesture control of a mobile robot.

Several approaches of the ray tracing model and physical explanation for the phenomen of the sensitive zone were developed in 2006 and presented in [37]. Experimental tests evidence the previously established physical theories and reveal that a higher surface roughness of the sensitive zone produce a higher amount of scattered waves. Multimode-Fibers characterized by different core diameters were sensitized with grinded imperfections and the signal attenuation was compared to them of untreated fibers. The application of a sensitive zone generated a linear dependence of the signal attenuation as a function of the bending angle.

A theoretical approach for the phenomena of the sensitive zone is given in [42] and [43]. The light source and the inner light propagation of the fiber core is described detailed by mathematical descriptions. The cavities were assumed as uniformly distributed and smoothly surfaced. The physical relations between the signal attenuation, the bending radius and the amount of cavities were examined by a theoretical model of the fiber under curvature. The optimum amount of cavities in the sensitive zone was determined to 50. The relations between the optimal length of the sensitive zone, the angle and height of the cavities were expressed in a single formula.

The effects of the imperfections and their characteristics such as abrasion angle, location angle, displacement and V-groove cavity depth on the signal attenuation are documented in [7]. The aforementioned parameters offer additional degrees of freedom for the individual adjustment of the sensor to its target application.

A curvature sensor owning a linear relation between the signal attenuation and the bending angle for a higher bending radius than 60 mm in static operation is presented in [44]. As in other researches, the bending direction was detectable by the sensitizing of the fiber with serrated cavities and its protection with an absorption layer. An IR-LED serving as a light source emits infrared light that is subsequently modulated to a frequency of 1 KHz. The demodulated signal demonstrated a polarity for each bending direction. The relative output loss as a function of the sensitive zone parameters was evaluated.

The *Monte-Carlo* simulation, characterized by ray tracing and an orthogonal matrix are utilized for the optimization of the sensitive zone parameters in 2010 and presented in [45]. The depth and the number of cavities represent the main sensitivity parameters of the sensor and the optimum amount of cavities was proposed to 55.

Looped fibers provided with sensitive zones were arranged on two symmetrical surfaces for the bending direction and torsional bending detection of surfaces is presented in [46] and illustrated on figure 2.55. A moving coordinate system in space enables the determination of the bending angle in relation to its shape in space.

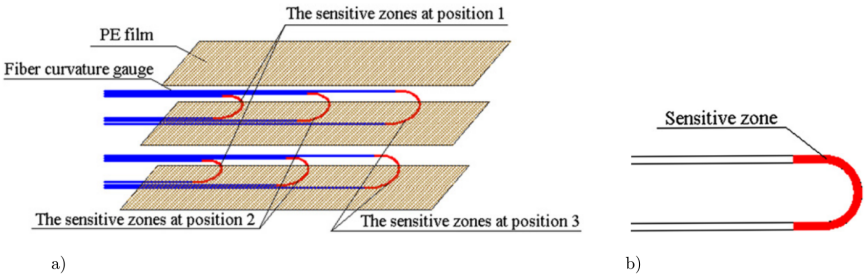

Figure 2.55: 3D-Curvature sensor a) Looped fiber arranged in sensor array b) Fiber provided with sensitive zone, adapted from [6].

A sensitized fiber, as illustrated on figure 2.56 represents a curvature sensor for the detection of small curvatures [47]. The sensor characteristics were determined on flexible and rigid surfaces. A potential sensor application is the crack detection in civil engineering. An almost linear dependence of the deformation and the normalized output power was revealed. The sensor principle is capable to measure strain, force and bending angle.

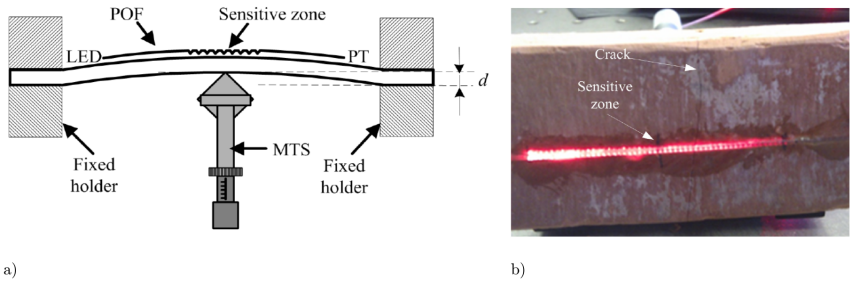

Figure 2.56: Deformation sensor: a) Measurement setup b) Fiber mounted on brick for damage detection, MTS-manual translation stage, PT-phototransistor, adapted from [47].

A high precision curvature sensor for displacements in a range of 1 mm with a resolution of 0.05 mm is described in [8] and illustrated on the following figure 2.57. Deformations of an metallic beam with the aid of a LED, a photodiode and a sensitized polymer optical fiber in transmission mode are measured.

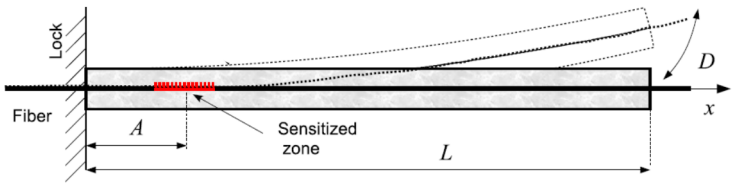

Figure 2.57: Curvature sensor for deformation measurement [8].

2.7.7. Sensor Applications for Human Joint Movement Analysis

Human Joint movement analysis is mainly utilized in rehabilitation, sportive analysis for high performance athletes and general medical applications. Lumbar spine analysis finds application in clinical assessment for the investigation of low back pain [4].

Human joint motion analysis is analyzable by non-invasive skin mounted systems, besides radiographic and stereo-radiographic imaging technologies. Repeated x-ray exposure, technical complexity and time consuming analysis is a disadvantage of the radiographic technology and it is only applicable for the analysis in static operation. General non-invasive skin mounted sensors for the analysis of limb curvature are: flexible curves, spinal mouse, electromagnetic sensors and gyroscopes [3].

Flexible curves facilitate the tracing of spinal shape by the derivation of its shape. The spinal mouse works with a wheeled accelerometer for the continuous recording of relative inclination in relation to the vertical body axis. Electromagnetic sensors, attached to a probe that tracks the spinal curve, consist of an electromagnetic emitting source for the location and orientation of the sensors. These techniques commonly determine curvature by the knowledge of the resultant angle between two tangents and provides static measurement of lumbar curvature or lordosis in a given posture. Emphasizing that all the aforementioned sensors only operate in static operation [4].

The analysis of human joint movements with the aid of tri-axial accelerometers is proposed in [1]. Several inertial sensors are attached next to the target joint before application. The measuring method results in a an extensive overall sensor design. A similar approach for the measurement of uni-axial joint movements based on a combination of accelerometers and gyrometers is presented in [48].

A graphical analyzing technique based on CCD-cameras for the detection of reflecting markers was proposed in [1]. The reflecting markers are attached on the

human body for the determination of joint position and body parts independently of the joint type. The accuracy of this technology depends mainly on the distance between the camera and human body, the size and the amount of markers.

The amount of POF-based sensors for the analysis of human joint movement increased rapidly due to the improvement of the POF characteristics and precision of detection methods. The measurement of human body movements is based on the determination of curvature or bending angles of a human joint by the examination of light intensity modulation on the fiber output.

2.7.8. POF Curvature Sensors for Human Joint Movement Analysis

Several approaches for the determination of curvature, utilizing POF-based sensors were realized in the past where the major part of the curvature sensors are based on light-intensity-modulation. The capability of reliable operation in dynamic operation, in contrary to a huge part of the traditional technology, makes the technology advantageous. The bending of the fiber induces a signal attenuation as a function of the bending angle and manufacturing methods were developed for the sensor sensitivity improvement, as explained in the preceding section. The bending direction of the fiber is specifiable by this method and represents the main advantage for the application in human joint movement analysis. The general POF-based curvature sensors utilized in human joint movement analysis with relevance to the present work are presented.

A light intensity modulated curvature sensor based on the misalignment between two fibers was developed in 1988 [49]. The fibers were positioned with the polished end faces, opposite to each other and aligned by a elastic tubing, as demonstrated on figure 2.58. The intensity alteration under curvature is measured by a photodiode and serves as parameter for the determination of the bending angle from a human finger.

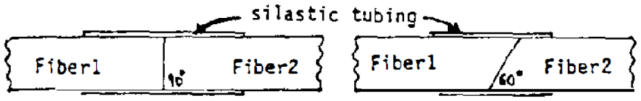

Figure 2.58: Curvature sensor composed of two opposite arranged fibers [49].

Posterior, the characteristics of a polymer optical fiber under curvature were analyzed detailed in [12]. The movement of a human limb was reconstructed by a special measurement setup and the application of the sensor is proposed for the field of rehabilitation in human joint movement analysis. An intelligent measurement setup forces a fiber to bend in a defined range and direction. Guiding slopes and the fixation of the fiber on a rotating wheel simulate a movement of a human limb such as arm, finger or knee. The wheel radius represents the constant bending radius and the amount of rotation, the bending angle. The incremental rotation of the wheel is controlled by a stepper motor, granting a high precision, as illustrated on figure 2.59.

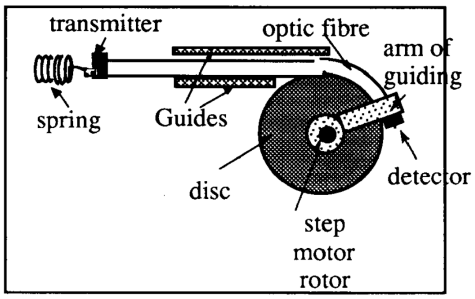

Figure 2.59: Measurement setup for reconstruction of human limb movement [12].

The curve shape of the signal attenuation as a function of the bending angle is nonlinear as depicted on figure 2.60a. The experimental results revealed that a decreasing bending radius leads to more accuracy in the bending angle determination due to a higher signal attenuation. The measuring range of the bending angle is enhanced for a larger bending radii.

The repeat accuracy was measured for a bending radius of $10mm$ as depicted on figure 2.60b. The mechanical memory of the POF leads to a difference in the the signal responses between a bend in going direction and a bend in return direction.

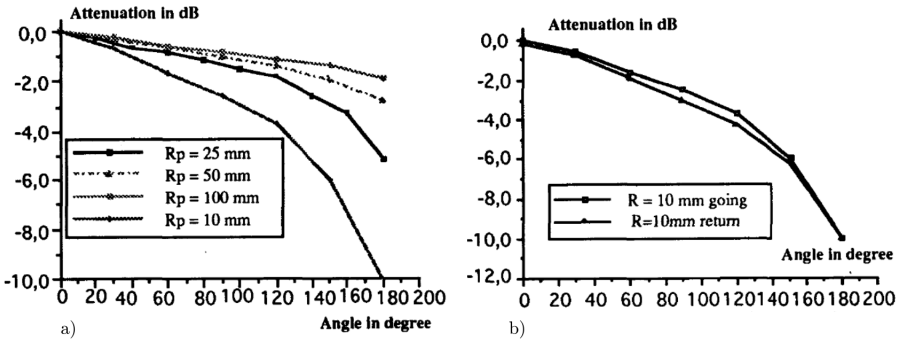

Figure 2.60: Signal response of curvature sensor: a) Signal attenuation as a function of the bending angle b) Signal attenuation for repeated bending as a function of the bending angle, adapted from [12].

Subsequent in 1995, the first approach of a curvature sensor provided with a sensitive zone is presented in [25], where two fibers are placed on a 500 mm cantilever beam and displaced in a range of 0.6 mm in each direction. Two LEDs serve as a light source and a Darlington-type photodetector as a receiver. The characteristic curve demonstrated a linear characteristic of the deformation as a function of the signal attenuation.

A wearable curvature sensor setup for physically handicapped persons is presented in [41] where two sensitized POF-based curvature sensors are attached on the garment and generate the input signal for an artificial neural network. The curvature sensors are based on light intensity modulation and consist of an IR-LED as light source, a photodetector as a receiver and a sensitized POF as sensing element. The fiber is finely machined by the side-polishing manipulation method for the bending direction detection. The sensor principle was applied as a gesture control unit for a mobile robot.

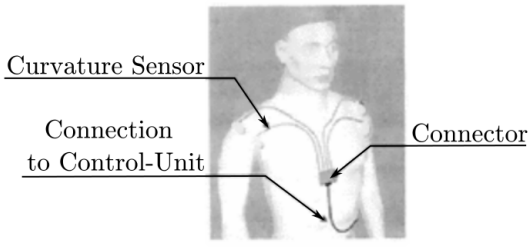

Figure 2.61: Werable curvature sensor for detection of arm movements, adapted from [41].

A POF curvature and strain sensor based on light intensity modulation is de-

scribed in [50]. The characteristic curve posses a linear sensitivity and high stability. A high reliability and small hysteresis proved the existence of low cost sensors characterized by high precision and reliability which makes it comparable to a Fiber-Bragg-Grating sensor.

Another POF sensor based on light-intensity-modulation for the detection of human angular movement was developed in 2003 and is described in [51]. The movement of a human arm was reconstructed by a special test setup where the bending radius and angular displacement were variable. An almost linear behave of the signal attenuation in relation to the bending angle range from 0° to 90° was produced.

A wearable curvature sensor, based on light-intensity-modulation for three dimensional trunk motion analysis is described in [52]. The measuring system consists of an IR-LED that provides light with a wavelength of 900 nm and a IR-photodiode as a receiver. The voltage output of the photodetector is processed by a microcontroller and the extracted information about the bending angles is transmitted via Bluetooth to a desktop computer.

A especially modified fiber-optic sensor, attached on a persons back determines dynamic movements of the lumbar spines during flexion and lifting, as presented in [4]. Fiber optic sensors based on light intensity-modulation were utilized for the measurement of dynamic changes in the lumbar spine surface. The sensors were arranged in an array and embedded in a plastic film. The curvature of lower and whole lumbar spine was measured and the results compared to the video-based analysis method *Vicon 370*, as depicted on figure 2.62. The optical sensor system proved almost identical consistency across repeated measurements in comparison to the video-based system. The authors mention that the system of *Vicon 370* requires days to reach sufficient competency for its utilization, while the POF-based proposed system is applicable within one day.

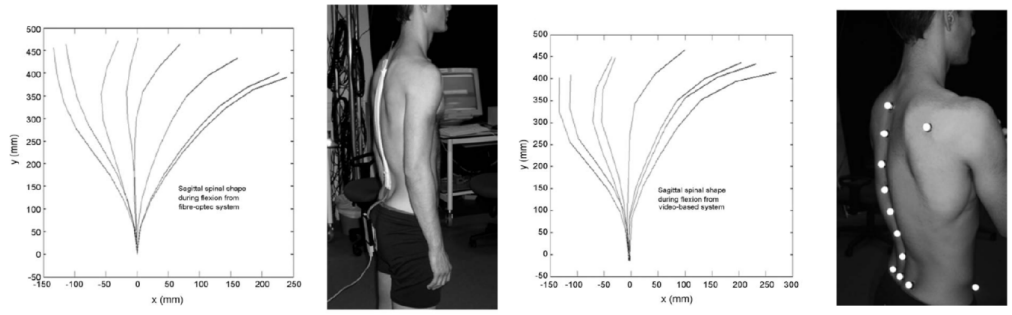

a) b)

Figure 2.62: Curvature and posture sensor for analysis of lumbar spine curvature a) POF-based sensor b) Video-based system, adapted from [4].

A curvature sensor for human joint movements is presented in [53], where looped fibers were arranged in a thin array and laminated on a ribbon substrate to sense bend and twist.

The preceding section described sensor examples of POF-based sensors and proved that POF-based sensors are applicable for human joint movement analysis by the measurement of curvature. Subsequent specific examples of curvature sensors for the analysis of knee joint movements are given in the following section.

2.7.9. Wearable Knee Sensors based on POF Curvature Sensors

A POF-based curvature sensor for the analysis of knee joint, elbow and ankle movements is presented in [54]. A side-polished fiber is supplied with carbon tubes to avoid an over bending of the sensitive region. A reference signal is received by a second photodetecor to determine the light fluctuations induced by the light source. The generated bending angle data is transmitted via Bluetooth to a desktop computer for subsequent analysis. The whole measurement system is attached on the persons waist and embedded in a belt wallet. Different movement scenarios for the knee joint such as barefoot walking, running and walking with slippers were performed. The movement scenarios for the elbow include flexures and throwing of an object. The ankle plantar-dorsiflexion angle for standing, sitting and stepping was examined. Reliable and constant signal responses were noticed for all movement scenarios.

A similar setup, developed in [54], for the monitoring of knee joint movements and gait analysis is presented in [55]. The research concentrates on the examination of the wearable sensor systems reliability, tested on different persons under certain ambient influences over a long time range. Thermal influences on the wearable measurement system were determined and revealed a slight influence of relative humidity (RH) on the sensor characteristics. The temperature effects were compensated by a calibration function. The sensor tests were proceeded on four different persons and reliable signal performance over a long time range were achieved.

A reliable and high precision curvature sensor based on light intensity-modulation for the examination of bending angles in dynamic operation of a human knee joint is presented in [5] and illustrated on figure 1.1. The characteristic curve of the signal attenuation as a function of the bending angle possess an exponential dependence in the range from $-125°$ to $+125°$ and a linear range between $-45°$ to $+25°$. In a reproducible process, the POF is finely formed with cavities arranged in a defined pattern. The measured data is transferred via *ZigBee* to a desktop computer for the analysis in *LABVIEW*. The signal response demonstrates a highly precise and reliable characteristic. The perturbation by loose part of the fiber between the joint and the control device, mounted on the persons waist were noticed.

3. Experimental Design

3.1. Experimental Design Considerations

The design and intentions for the creation of the experimental setup are described in the present chapter. At the beginning, some considerations in respect to the choice of the individual system components and their characteristics are made.

Measurement setups for the simulation of human limb movements were developed in several researches. Measurement setups for the guided curvature of the fiber with a constant bending radius are presented in [11] and [12], as illustrated on the following figure 3.1a and 3.1b. The movement of a human arm was reconstructed and described in [51], as depicted on 3.1c.

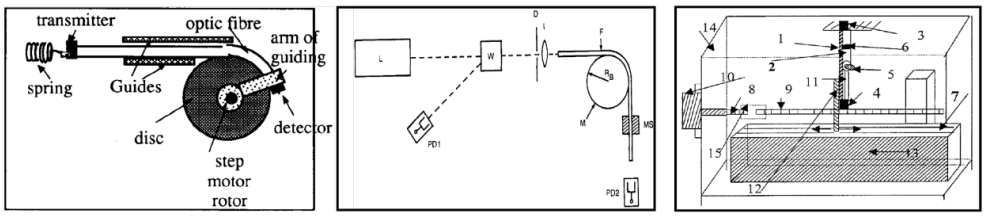

a) b) c)

Figure 3.1: Different measurement setups for the reconstruction of a human limb: a) Automated curvature setup [12] b) Curvature setup for guided bending of fiber [11] c) Reconstruction of an elbow joint movement [51].

The influence different looped fiber arrangements on the signal response are investigated in the present work. Therefore, an experimental setup has to be created that facilitates the examination of the fiber curvature with a goniometer. Initial tests on an elementary measurement setup lead to a general impression of the fiber curvature effect on the speckle-pattern and founded the basic knowledge for the design of an acrylic goniometer, as depicted on figure 3.4. The measurements for the fiber arrangements of fivefold-, threefold-looped and single fiber are performed on the first measurement setup, as illustrated on figure 3.4. The system was identified on the basis of these measurement results and an second improved test setup with a two-times looped fiber was realized, as shown on figure 3.12.

The determination of the bending angle is based on digital speckle-pattern image processing. The embedded system *Raspberry Pi* includes a 5-Megapixel high frame rate and wide-angle lens CCD-camera for the capture of high resolution images. The individual configuration of the CCD-camera parameters is the main reason for the choice of this system. Hardware drivers of digital web-cameras are often limited in configuration and contain automatic calibrations of *White Balance*, *Brightness* or *Exposure*. Thus, unpredictable recordings of the speckle-pattern images would result. The embedded systems small dimensions and wireless network connection devices, makes it comfortable for the present application.

The sensor concepts as presented in [5], [52], [54] and [55] demonstrate an autonomous measurement system including a wireless data transfer method for the outsourced analysis of data. The signal processing unit is embedded in an plastic case or wallet and weared on the persons waist belt. In the present application, the transferred data is a video stream for the posterior image processing and bending angle calculation on a desktop computer. The image data represents a high amount of data. 40 frames with a resolution of 1296 x 972 and 8-bit depth per second corresponds to a data size of approximately 1.96 MB per second that has to be transmitted. The transmission over Wi-Fi on the protocol platform TCP/IP was chosen. The technology is convenient, the RPI supports a transmission range of 100 Mbps and almost every computer is equipped with a receiving device.

The robustness of the fiber is strongly diminished by mechanical or chemical etching, as revealed in [5]. The advantages of the sensitizing methods for curvature sensors was analyzed in section 2.7.5. The potential application of the curvature sensor for joint movement analysis, requires a fiber of high durability that resists high quantities of repeated bendings. A non-destructive method for the improvement of sensor sensitivity was chosen and is realized by looping the fiber for several times, as depicted on figure 3.6. This method contains several degrees of freedom in the arrangement, as previously analyzed in section 2.7.5.

The recorded digital images of the speckle-pattern represent a source of informa-

tion for a diversity of analyzing techniques. A video of a speckle-pattern during a movement can be recorded and afterwards analyzed the utilization of the measurement setup. The image processing techniques can be combined with intelligent algorithms like an Artificial Neural Network for the compensation of external influences such as temperature or humidity. A diversity of image filters is applicable in the spatial or in the frequency range. The degrees of liberty for further researches is given by the application of an image processing technique for the determination of the bending angle based on the changes in the speckle-pattern.

The considerations and fundamental studies lead to a system design as represented on the schematic overview on the following figure 3.2 and on the a realization on the photo 3.3.

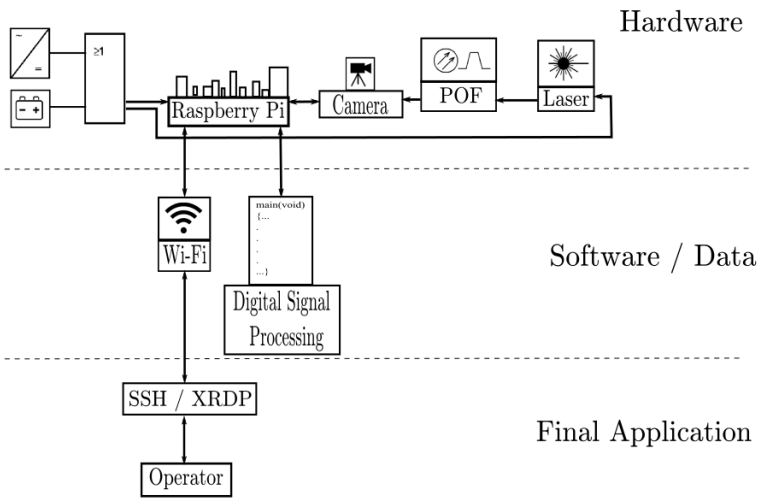

Figure 3.2: System overview of measurement setup.

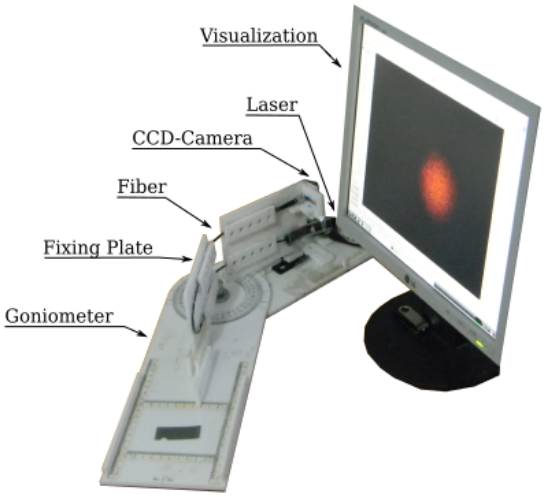

Figure 3.3: Photo of measurement setup.

3.2. Overview of Experimental Design

The curvature measurement setup is composed of several components such as the Multimode-Step-Index Polymer Optical Fiber, Model *Eska Premier*, fabricated by *Mitsubishi Rayon Co. LTD*, serving as a wave guide and curvature sensing element. A He-Ne laser that provides continuous coherent light with a wavelength of 632.8 nm. The POF core with a typical diameter of 980um consists of *Polymethyl-Methacrylate Resin* with a core refractive index of 1.49 and a numerical aperture of 0.5 [17].

A video stream with a frame rate of 40 frames per second (FPS) and a resolution of 1296 x 972 is generated by the *RaspiCam* that consists of an individually configurable five Megapixel CMOS Image sensor *Omnivision OV5647* and is controlled by the embedded system *Raspbery Pi Model B+* [56].

A desktop computer receives the video stream via Wi-Fi and realizes the image processing with the aid of the open source computer vision library *OpenCV 2.4.9*.

The overall measurement components are mounted on an acrylic self-designed goniometer, as depicted on the following figure 3.4. The measuring setup was

developed in a previously published research for the curvature measurement with the aid of speckle image processing [57].

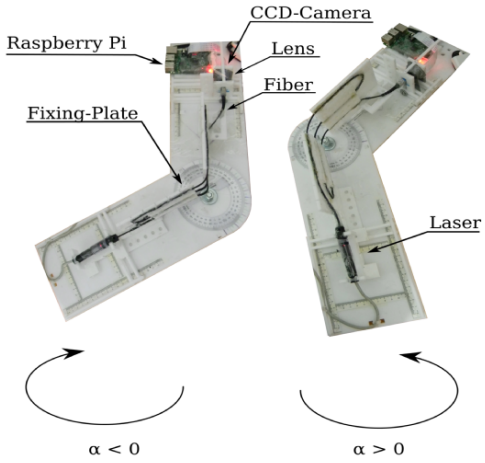

Figure 3.4: Detailed measurement setup with bending directions.

The sensor setup was developed under consideration to be applied as a human knee curvature sensor as proposed in [5], therefore the data is sent via Wi-Fi to a desktop computer and the power supply is realized with a battery. A defined curvature of the fiber with a constant bending radius as described in [12] is necessary for qualitative and reliable measurement results. Hence a mechanical construction for the curvature measurements that incorporates the light source and the image processing unit was developed. Looped fiber arrangements as described in [38], [18] and [19] demonstrated an amplification in signal attenuation during curvature and of this effect is taken advantage with the attachment of the fiber on fixing plates on the top of the goniometer. The amount of the bending angle can be adjusted individually by the movement of one goniometer leg.

The whole system mounted on the top of the goniometer, describes an idea for a compact setup of a human knee curvature measurement under general aspects of its application. The following figure 3.5 represents the measurement setup of the threefold-looped fiber, attached on the fixing plates on top of the goniometer.

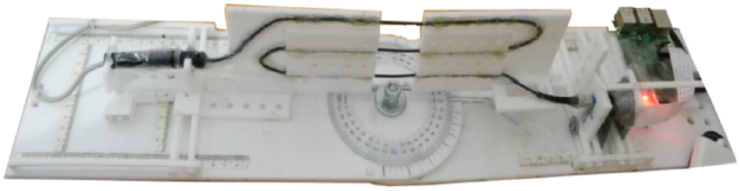

Figure 3.5: Side view of threefold-looped fiber measurement setup.

3.3. Hardware Setup

3.3.1. Mechanical Goniometer

A general evaluation of the signal response under curvature at the beginning of the project was realized with some elementary constructions and fiber arrangements. Low mechanical shocks, such as knocks or vibrations caused by a fan or a desktop computer on top of the measuring table, already caused a visible distortion in the speckle-pattern, visible by image blurring. The effects are amplified by partly loose fiber parts attached on the goniometers fixing plates. These effects arise from undefined and non-repeatable bending shape of the fiber under curvature. Therefore, the whole fiber path is hot glued on acrylic fixing plates.

The laser, the fiber tip and the CCD-camera are fixed on adjustable slopes to ensure an adaptable measurement setup. The components are fixed with screws on the slopes, after positioning. These degrees of liberty are important for adjusting the speckle-pattern image by aligning the lens, the CCD-camera and the fiber tip in the horizontal and vertical plane. The whole goniometer is mounted on foam-pads for the mechanical decoupling of the measurement table. The bending radius of the fiber is determined by the distance between the two acrylic fixing plates. The measurement results that are described in the further section were produced with a bending radius of 200 mm for the fiber arrangements, as depicted on figure 3.6.

The curvature of the fiber reduces the numerical aperture and leads to a rising signal attenuation for an ascending bending angle, as previously described in section 2.6.2. The amount of loops is varied for the examination of the effects

on the signal response and the fiber arrangements as depicted on figure 3.6 were utilized. The amount of loops demonstrates the amount of bending points of the fiber under curvature. The laser is positioned opposite to the CCD-camera on the goniometer and leads to an odd amount of loops for the first measurement setup. The different arrangements of the fiber are performed chronologically and designated with ascending roman numbers, as depicted on the following figure 3.6. The test setups are designated as the first for the fivefold-looped setup, the second for the three-times-looped setup, the third for the single fiber setup and the fourth for the two-times-looped fiber setup to demonstrate the chronological sequence of development of the test setups, as described on the figure 3.6.

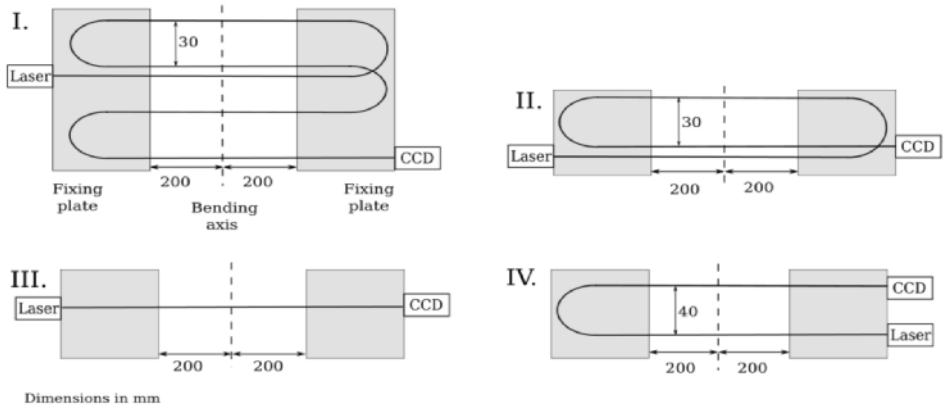

Figure 3.6: Fiber arrangements in chronological sequence I. Five-times-looped fiber II. Three-times-looped fiber III. Single fiber IV. Two-times-looped fiber.

The amount of loops is considered as an adjustable sensibility parameter of the sensor. The effect of a fivefold-, threefold-, twofold-looped and a single fiber under curvature are evaluated by the analysis of the resulting speckle-pattern.

Modifications on Mechanical Goniometer

For the determination of the bending angle, one leg of the goniometer is moved clockwise and counter-clockwise, as depicted on figure 3.4. The method of the POF attachment on the fixing plates generated an inconstant bending characteristic. The following figure 3.7 represents the goniometer and the marked points, where displacements occurred during bending. As observable, the fiber bending point is slightly displaced from the origin bending axis of the goniometer, marked as a dotted line, which influences the signal response as revealed later in the section

of the analysis.

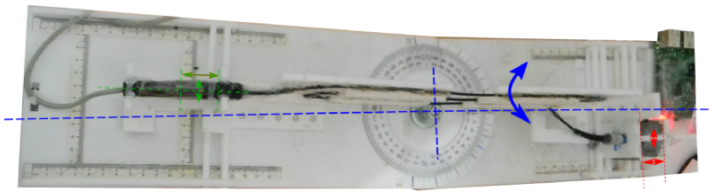

Figure 3.7: Origins of signal deviations of first measurement setup.

The fixing plate, mounted on the same side of the goniometer as the laser, experienced a displacement in horizontal direction with an growing bending angle, marked as red arrows in the following figure 3.7. A more far distance between the laser and the fiber input face is induced by drawing forces, marked with green arrows on figure 3.7. This effect induced a measurable influence on the speckle-pattern light intensity and was compensated by the mechanical connection of the laser with the fiber input.

The fixing plate, mounted on the same side of the goniometer as the CCD-camera, experienced a vertical displacement with an ascending bending angle, marked with blue arrows on figure 3.7. This fact can be explained by the sole fixing point on the bottom, thus the upper part of the fixing plate is flexible. The displacement of the fixing plate grows with an ascending bending angle, according to the rigidity of the fiber. The relative horizontal position between the fibers end face and the CCD-camera lens gets affected. Significant changes in the speckle-pattern are produced. The point of displacement between the CCD-camera and the fiber end face is marked with red arrows on figure 3.7. This undesirable effect was compensated by supporting the fixing plate with additional lateral plates. Secondly, the mounting plate of the POF tip and the CCD-camera were connected constructively as depicted on the following figure 3.8.

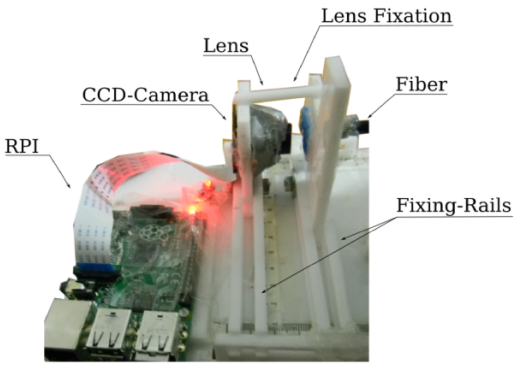

Figure 3.8: Detailed view of optical coupling between fiber end face and CCD-camera of first measurement setup.

The previously mentioned side effects were compensated before the measurements of the fivefold-, threefold-looped and single-fiber arrangements were performed.

3.3.2. The Laser

A Helium-Neon-laser, Model.No.*41735.9E*, fabricated by *PHYWE* emits continuous coherent light with a wavelength of 632.8 nm, supplied with $5V$ DC.

3.3.3. The Polymer Optical Fiber

A Multimode Step-Index Polymer Optical Fiber, Model *Eska Premier*, fabricated by *Mitsubishi Rayon Co. LTD* serves as a waveguide and curvature sensing element. The POF core with a typical diameter of 980 μm consists of *Polymethyl Methacrylate Resin*, a core refractive index of 1.49 and a numerical aperture of 0.5 [17]. The large core diameter posses high mechanical rigidity, which was the criterion for its choice.

3.3.4. The Embedded System Raspberry Pi

The Embedded System (ES) *Raspberry Pi Model B+* was developed by *Raspberry Pi Foundation* for prototyping and educational applications. The *Raspberry Pi* (RPI) consists of a *SoC* running on a 700 MHz *ARM1176JZFS CPU* with 512 MB SDRAM. A especially created operating system (OS) called *Raspbian* installed on a 8 GB *micro SD* improves the handling comfort of the ES. The RPI can be connected to a LAN via cable or a Wi-Fi pendrive. Additional digital I/O pins and serial interfaces can be accessed by the application of different

programming languages such as *Python, C, C++, Java, Scratch* and *Ruby*. The system was chosen due to the liberty of the CCD-camera *RaspiCam* control and the simplicity of usage. The employment of the ES avoids additional Hardware development and serves as a reliable base for technical development. The low dimensions of 85 x 56 x 17 mm and low power consumption at a supply voltage of $5V$ DC makes the system suitable for a variety of applications [58]. The following figure 3.9 demonstrates the Raspberry Pi and the labeled Hardware interfaces.

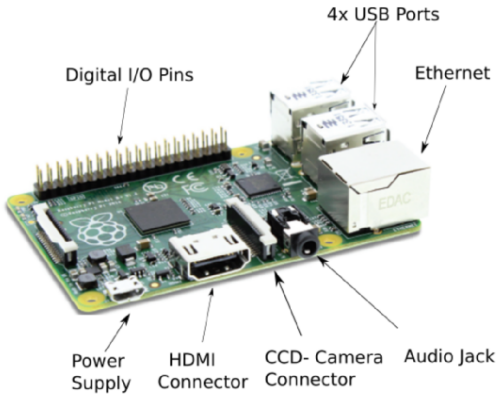

Figure 3.9: System overview of the embedded system Raspberry Pi, adapted from [58].

3.3.5. The CCD-Camera RaspiCam

The *RaspiCam* consists of an individually configurable five Megapixel 1/4" CMOS Image sensor *Omnivision OV5647*. The wide-angle lens is characterized by the size of 1/4" and a chief ray angle of 24°. The CMOS-Chip owns an effective CCD detection area of 2592 x 1944 μm and provides a 8/10 *bit* raw RGB-Image on the output. Several resolutions with frame rates in a range of 15 fps at a resolution of 2592 x 1944 pixels up to 120 fps at a resolution of 320 x 240 pixels can be defined. The high signal to noise ratio (SNR) of 36 dB and a dynamic range of 68 *db* assures a high quality image signal [56].

3.3.6. The Polarizer

A polarizer between the fiber end face and the lens of the CCD-camera is utilized for the evaluation of its effect on the detected amount of contours. Light gets partially reflected or absorbed by the filter that is not perpendicular orientated to the propagation direction. A scattering of a light wave by a surface causes

a partly depolarization of light. The granular structure of the speckle-pattern is changed when observed through a polarizer, rotated from 0° to 90°. For a complete depolarization of reflected waves, the complete contrast of the speckle-pattern is rather unity [22]. The polarizer is characterized by a plastic sheet in quadratic form of the dimensions 50 x 20 *mm*.

3.3.7. Software Development Environment

The image processing algorithm is programmed in *C++* with the integration of the open-source computer vision library *OpenCV 2.4.9*. The library was developed for the image analysis and feature detection and is mainly applied in the field of Robotics and can be utilized by the programming languages *C*, *C++* and *Python*. A desktop computer, running with the *Linux* operation system *Ubuntu 14.04 LTS* realizes the image processing tasks.

3.4. Improvements on Hardware Setup

The design of the twofold-looped fiber setup is based on the knowledge, achieved of the system analysis performed in section 4.1. Improvements on the measurement setup on the basis of the system analysis were realized and produced the final test setup of the two-times looped fiber. The following schematics 3.10 and 3.11 represent the final measurement setup, the two-times-looped fiber setup. The main characteristic is the same mounting side of the laser and the CCD-camera on the top of the goniometer, for the prevention of displacements on the optical coupling points.

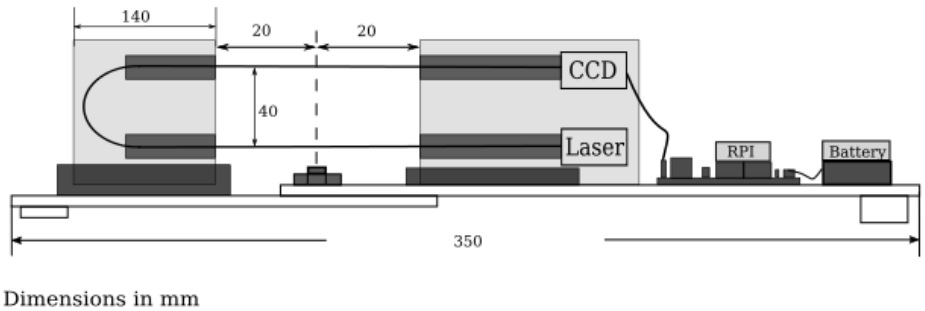

Figure 3.10: Side view of two-times-looped measurement setup.

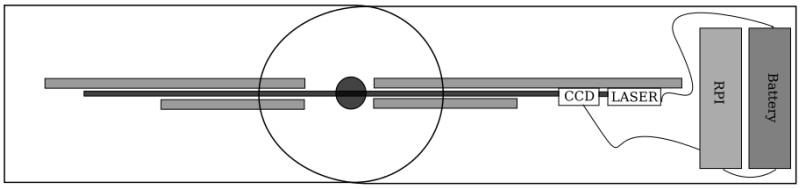

Figure 3.11: Top view of two-times-looped measurement setup.

The fixing plates are mounted exactly on the bending axis of the goniometer, hence the bending characteristic is almost identical for both bending directions that was not the case in the previous measurement setup. The type of attachment of the fixing plate was improved by more rigid support devices and the fiber attachment is supported with additional plates on the fixing plates as depicted on figure 3.10 and 3.12.

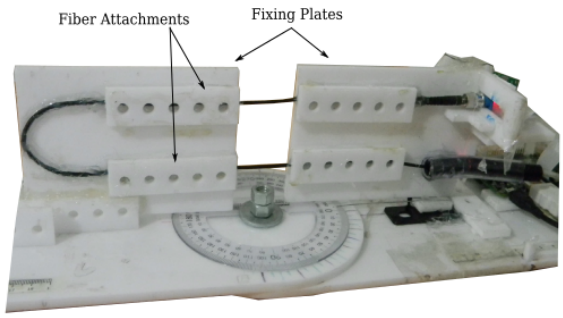

Figure 3.12: Photo of two-times-looped measurement setup.

The laser and the fiber input are housed in a tubing that ensures the precise and constant aligning as depicted on the figure 3.14. The light is directly coupled into the camera lens through a diffuser, thus the additional lens in front of the CCD-camera is removed. Less signal attenuation and imprecision by its displacement was eliminated by this measure.

The following figure 3.13 illustrates the optical connection between the fiber end face and the CCD-camera. The purpose is the optimum light coupling and transmission of the speckle-pattern onto the CCD-chip array. The calculations are performed on the basis of the numerical aperture of the POF and the chief-ray angle of the CCD-camera wide-range lens.

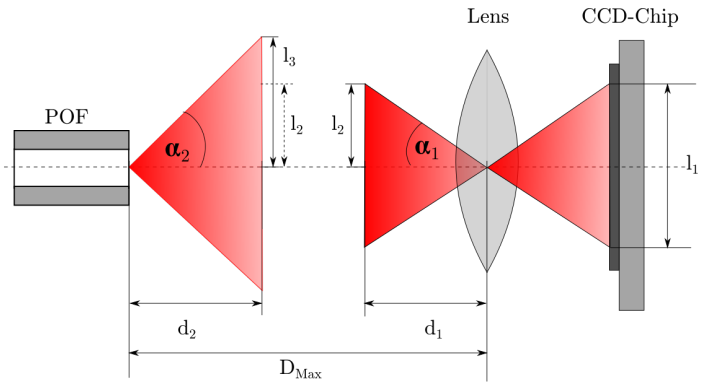

Figure 3.13: Schematic of optical connection between the fiber end face and the CCD-camera.

The system parameters are assumed as follows:

$\alpha_1 = 24°$ represents the *chief ray angle* of the camera lens.

$\alpha_2 = 30°$ indicates the acceptance angle of the fiber, calculated by means of the numerical aperture of $NA = 0.5$.

$l_1 = 2.4\ mm$ demonstrates the CCD-array diagonal and $l_2 = \frac{l_1}{2}$ describes the object dimensions that ensure an optimum image coupling onto the CCD-chip under assumption of the lens focus.

The distance for that an optimum exploitation of the CCD-array chip size is guaranteed, is stated as follows.

$$d_1 = \frac{l_2}{\tan(24°)} = \frac{1.2\ mm}{\tan(30°)} = 2.69\ mm \tag{3.1}$$

The distance from the fiber end face, for that the optimum focus of the camera lens is still given, is calculated as follows.

$$d_2 = \frac{l_2}{\tan(30°)} = \frac{1.2\ mm}{\tan(30°)} = 2.07\ mm \tag{3.2}$$

The maximum distance between the fiber end face and the CCD-camera that still ensures an optimum image projection onto the CCD-chip is stated as:

$$D_{max} = d_1 + d_2 = 2.07\ mm + 2.69\ mm = 4.7\ mm \tag{3.3}$$

As can be observed from the calculations and figure 3.13, the length l_3 should be the same as l_2 for an improved light coupling and image projection. The calculated

distance $D_{max} = 4.7\ mm$ represents a maximum value and a higher distance leads to additional signal losses arising from lost light rays. The distance between the CCD-camera and the fiber end face were chosen to $D = 4\ mm$ in the experimental setup. The following figure 3.14 illustrates the optical coupling point between the fiber end face and the CCD-camera, including the optical diffuser.

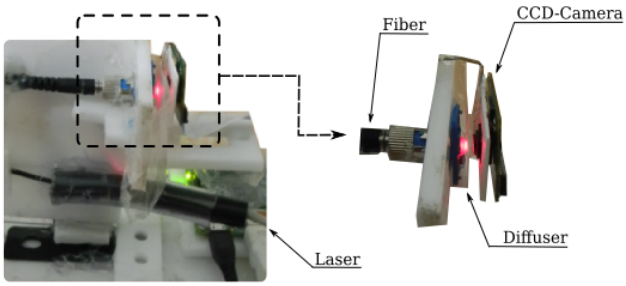

Figure 3.14: Detailed view of optical coupling point between fiber end face and CCD-camera of two-times-looped measurement setup.

3.5. Digital Image Processing

A granular speckle-pattern is recorded by the CCD-camera on the fiber output face and looks like a red lighting circle over a black background. The light distribution and intensity of the speckle-pattern changes in relation to the amount of bending angle. The variation in intensity is analyzed by several image processing steps such as spatial filtering and edge-detection. Two approaches for the determination of the bending angle by speckle image processing methods are investigated in the present research. The image processing techniques are performed in the spatial domain by the the fact of the working principle of the *Canny-Edge-Detection Algorithm*.

The first approach is a self-developed combination of image processing stages, based on the counting of the amount of contours within a defined region of the image by the Canny-edge-detection algorithm. The spatial image filters *Gaussian Low-Pass filter* and *Bilateral filter* are applied and compared under the focus of computational efficiency and the improvement of edge detection. The *Image Averaging* technique was applied as an image filtering technique. The variation of

the speckle intensity distribution is evaluated in a defined region of interest (ROI) and position on the source image. The influence of the ROI position on the edge detection was investigated.

The second approach for the detection of the bending angle, by the analysis of the speckle-pattern is realized with the *Speckle Mean Intensity Variation* (MSV) measuring technique as described in [13], where it is applied for the temperature measurement of a heated POF. The MSV is advantageous by its simplicity in implementation and low computational effort. The technique serves as a reference technique for the comparison with the self-developed canny-edge-detection technique.

The video frame of 40 fps with a resolution of 1296 x 972 is analyzed frame by frame where each frame is converted from Blue-Green-Red (BGR) OPENCV-image format to a gray image for the following processing of the Canny-edge detector. The information of colors is unnecessary for the edge detection and the Gaussian Low-pass filter would generate unexpected results by different filtering behave for each color channel. The Gaussian Low-Pass filter and the Bilateral filter suppress high distortion pixel intensities that could be detected as an edge. The amount of contours is determined and serves as an input signal for the calculation of the angle. The individual image processing stages are depicted on 3.15 [59] .

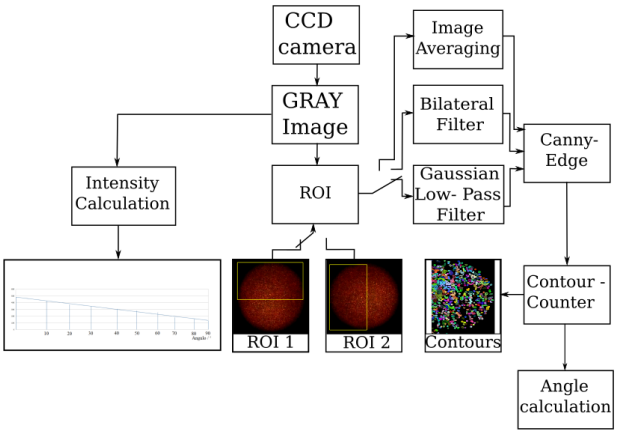

Figure 3.15: Image processing stages for speckle contour detection.

3.5.1. The Region of Interest

As previously discussed in the section 2.6.5 of the curvature analysis, the intensity of light is concentrated on one side on the fiber output face and therefore, the variation of the intensity distribution in a defined region on the speckle-pattern image is evaluated. The upper and the lateral part of the speckle-pattern represent the strongest variation in intensity distribution. Therefore, a ROI of size 500 x 270 pixels is positioned in these areas of the source image. The camera enables a recording of a defined ROI for the reduction of the recorded image data. Lateral displacement between the fiber tip and the CCD-camera is not detectable by application of this method, because the position of the camera ROI on the speckle-pattern of the fiber end face is not determinable. A displacement of the fiber is detectable already by inspection when the ROI is applied afterwards, because the whole speckle-pattern of the fiber end face is visible. Secondly, the image data of the entire speckle-pattern represents a source of information that can be utilized for further studies. The reduced image size generates less computational effort and is noticed as a positive side-effect of this method. The subsequent image processing tasks are applied on the cropped image. The different ROI placements on the speckle-pattern are illustrated on the following figure 3.16.

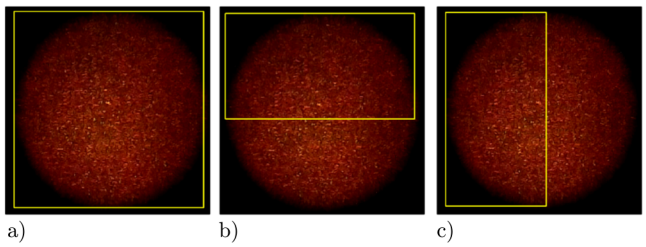

Figure 3.16: Different ROI placements on speckle-pattern: a) Entire speckle-pattern b) Upper half of speckle-pattern c) Lateral half of speckle-pattern.

3.5.2. Spatial Image Filtering

3.5.2.1. Gaussian Low-Pass Filter

The Gaussian Low-Pass filter is known in literature as the *Gaussian Blur*. The spatial image filter is based on domain filtering and computes a weighted average of neighborhood pixel values, determined by the distance to the center. The image filter smooths an image by averaging high pixel intensities in comparison to the average pixel intensity in an image. High intensity steps between two neigh-

borhood pixel are considered as an image distortion in digital image processing. Gaussian-Blur can be utilized for the restoration of images with low resolutions, however in our case it serves as a pre-stage for the edge detection improvement by the following Canny-edge-detection algorithm [60], [59].

Definition of Gaussian Low-Pass Filter

The *Kernel Size* represents the size of the kernel mask by M x N and the *Standard Deviation* σ, determines the spread of the Gaussian curve. An increasing kernel size M x N amplifies the blurring effect and reduces the visibility of edges. The standard deviation σ determines the spread of the Gaussian curve and represents the weight of the of the neighbor pixels. The weight decreases with an increasing distance from the Gaussian center as illustrated on the figure 3.17a. The spatial filter is based on the assumption that pixel values vary in a maximum range of pixel intensity. The intensity of a noise pixel in comparison to the neighborhood pixel is less correlated and gets reduced by averaging the neighbor pixels. The information of the image is preserved by application of this method [60], [59].

The following figure 3.17a demonstrates the influence of the filter kernel on the image and the figure 3.17b the corresponding filter kernels with different Gaussian curve spread.

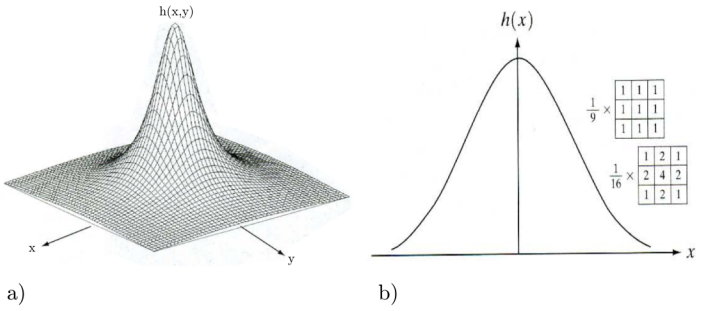

Figure 3.17: Gaussian Spatial Filter: a) 3D-visualization of filter kernel b) Gaussian curve with different filter kernels, adapted from [59].

The original image $f(x, y)$ of size M x N is convoluted with a filter mask $h(x, y)$ of size of m x n, producing the blurred image $g(x, y)$ [59], [61]. The general

convolution theorem for a two-dimensional space is stated as:

$$g(x,y) = f(x,y) * h(x,y) \tag{3.4}$$

in detail:

$$g(x,y) = \frac{1}{MN} \sum_{m=0}^{M-1} \sum_{n=0}^{N-1} f(m,n) \cdot h(x-m, y-n) = \frac{1}{MN} \cdot h(x,y) \tag{3.5}$$

where $h(x,y)$ is the Gaussian two-dimensional spatial Filter defined as [59]:

$$h(x,y) = G_0(x,y,\sigma) = \frac{1}{2\pi\sigma^2} \cdot e^{-\frac{x^2+y^2}{2\sigma^2}} \tag{3.6}$$

3.5.2.2. Bilateral Filter

The Bilateral filter can be considered as a combination of a domain filter and a range filter and is characterized by suppressing noise while preserving the information of edges. In case of its application on an image that contains a textured object, the textured area gets blurred while the visibility of object contours improves [60], [61].

Differences between two pixels can be considered as *close* by spatial distance or can be *similar* by comparing their values. In smooth areas where the pixel intensity does not vary significantly, the Bilateral Filter acts as a domain filter that averages higher pixel values, originated by noise pixels smooths the intensity distribution. This filtering characteristic is the same as of the aforementioned Gaussian Low-Pass filter [60], [61].

Assuming a high step of intensity between two pixels that represent a sharp edge in an image, as depicted on the following figure 3.18a: The Bilateral-Filter kernel is centered on the pixel with the higher intensity, as depicted on 3.18b, then it is replaced by the sum of the bright pixels in his neighborhood while the low intensity pixels are ignored. The contrary happens when the filter kernel is centered on the pixel with the lower pixel intensity. The edge after a bilateral filtering procedure on figure 3.18c demonstrates the preservation of edge information, while the

Gaussian noise is significantly suppressed [60], [61].

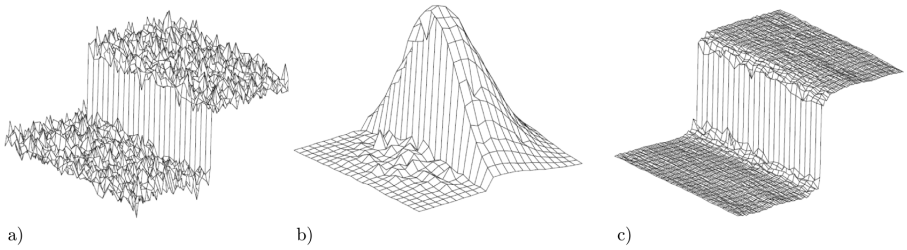

Figure 3.18: Bilateral filtering steps: a) Gray Level step perturbed by Gaussian noise of $\sigma = 10$ gray levels b) 23 x 23 similarity weight function applied on edge c) Edge after bilateral filtering, adapted from [60].

The previous example proves that the combination of the the domain and the range component causes a smoothing effect in areas with low variation of intensity, while crisp edges are preserved [60].

Definition of Bilateral Filter

The Bilateral Filter consists of a *Domain Kernel* $d(i, j, k, l)$ and *Range Kernel* $r(i, j, k, l)$. By their multiplication, they result in the *Bilateral Weight Function* $w(i, j, k, l)$. The domain kernel is defined as:

$$d(i, j, k, l) = exp\left(-\frac{(i-k)^2 + (j-l)^2}{2\sigma_d^2}\right) \tag{3.7}$$

The range kernel is stated as follows:

$$r(i, j, k, l) = exp\left(-\frac{||f(i, j) - f(k, l)||^2}{2\sigma_r^2}\right) \tag{3.8}$$

The bilateral weight function is defined as:

$$w(i, j, k, l) = exp\left(-\frac{(i-k)^2 + (j-l)^2}{2\sigma_d^2} - \frac{||f(i, j) - f(k, l)||^2}{2\sigma_r^2}\right) \tag{3.9}$$

The resulting image is calculated by a weighted combination of neighboring pixel values [61]:

$$g(i, j) = \frac{\sum_{k,l} f(k, l) \cdot w(i, j, k, l)}{\sum_{k,l} w(i, j, k, l)} \tag{3.10}$$

3.5.2.3. Image-Averaging

Image Averaging is an average calculation of several images and their pixel intensities. A sequence of images is continuously summed and scaled to the intensity depth of 8-Bit, corresponding to the range of 0 and 255 [59].

The final average image is scaled to the range of 0 to 255 after each summation. The common procedure applies a division of the final average image by the amount of summed images. The procedure generates wrong pixel intensities by values that exceed the 8-Bit range and reduces the quality and originality of the image [59].

The addition of several uncorrelated speckle-pattern images reduces the contrast of the final speckle-pattern images [22].

Definition of Image Averaging

The pixel values on the positions x, y of the final image $g_{avg}(x, y)$ consist of the scaled average of the pixel values of the summed images $f_i(x, y)$ on the positions x, y. Low computing effort and high effectiveness is a main advantage of this technique. Distortions in the image are reduced by the averaging of pixel values [59]

Two images $f_1(x, y)$ and $f_2(x, y)$ are added and result in the average image $g(x, y)$.

$$g(x, y) = f_1(x, y) + f_2(x, y) \tag{3.11}$$

The minimum value $min(g(x, y))$ of the average image $g(x, y)$ is subtracted for the elimination of negative pixel values and represent the image $g'(x, y)$.

$$g'(x, y) = g(x, y) - min(g(x, y)) \tag{3.12}$$

Afterwards, the average image $g'(x, y)$ is scaled to the range of 0 to 255 by its multiplication with the scaling factor f_{avg}, defined as:

$$f_{avg} = \frac{255}{max(g(x, y))} \tag{3.13}$$

The final image g_{avg} is stated as:

$$g_{avg} = f_{avg} \cdot g'(x,y) = f_{avg} \cdot \frac{255}{max(g(x,y))} \tag{3.14}$$

Figure 3.19 describes the processing stages as implemented in the source code for the image averaging technique.

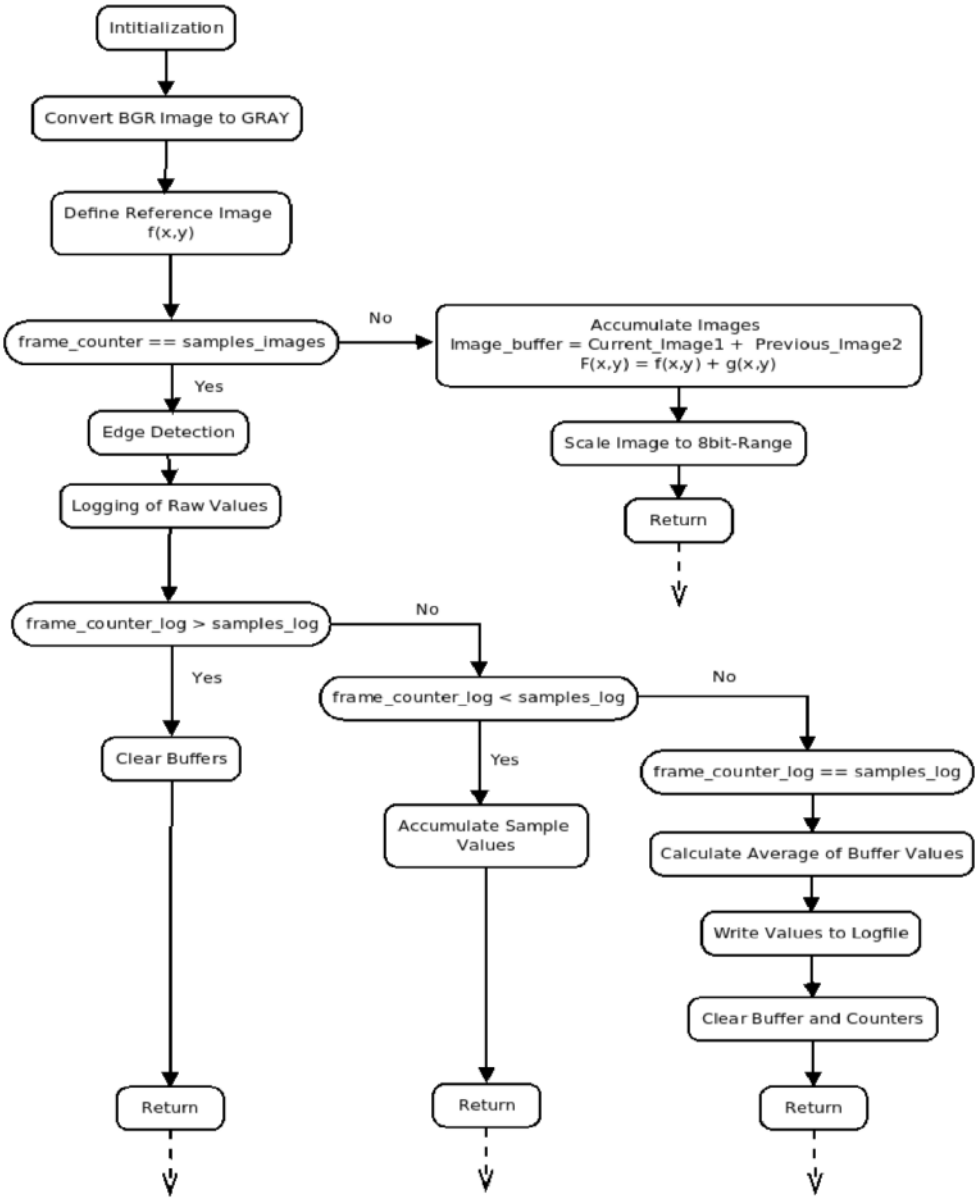

Figure 3.19: Structogram of image averaging routine as implemented in source code.

3.5.3. Spatial Filters Comparison

The following figure 3.20 illustrates the speckle-pattern images in gray format for different spatial filter application and proves that each spatial image filter affects the speckle-pattern in a different kind.

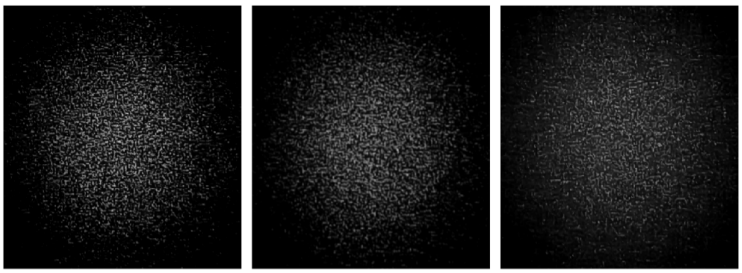

a) b) c)

Figure 3.20: Comparison of filtered speckle-patterns: a) Bilateral Filter b) Gaussian Low-Pass Filter c) Image Averaging.

3.5.4. Canny-Edge Detector

The Canny-Edge Detector algorithm was published in 1986 by *John Canny* and describes a reliable method for edge detection in a Gaussian-smoothed image [62]. The algorithm is characterized by its reliability, precision and low computing effort. Among other application fields it can be mainly found in the research area of feature detection in robotics and autonomous vehicles. For the present work, the algorithm is applied on a ROI of the speckle-pattern that generates an image with marked speckle contours. The concentration of speckles in a defined region can be determined by counting the number of closed contours. The following figure 3.21 represents the image processing stages that are performed for the contours detection.

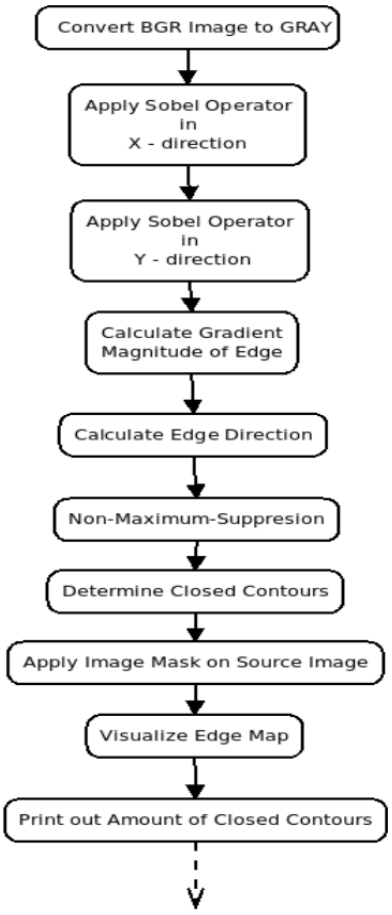

Figure 3.21: Structogram of Canny-edge detection algorithm as implemented in source code.

Definition of Canny-Edge Detector

The canny edge detector applies *Sobel*-operators to turn the firstly invisible edges into visible ones. In practice, a pair of convolution masks is applied to amplify the edges in horizontal and vertical direction [59].

$$\nabla f = \begin{bmatrix} G_x \\ G_y \end{bmatrix} = \begin{bmatrix} \frac{\partial f}{\partial x} \\ \\ \frac{\partial f}{\partial y} \end{bmatrix} \tag{3.15}$$

In the present work the *Sobel*-operators are applied as the gradient vector for both directions x and y [59].

$$G_x = \begin{bmatrix} -1 & -2 & -1 \\ 0 & 0 & 0 \\ 1 & 2 & 1 \end{bmatrix} \qquad G_y = \begin{bmatrix} -1 & 0 & 1 \\ -2 & 0 & 2 \\ -1 & 0 & 1 \end{bmatrix} \tag{3.16}$$

The maximum rate of grow of $f(x, y)$ per unit distance in direction of ∇f is also called the *Gradient* and is calculated as the magnitude of the ∇f at the coordinates (x, y) [59].

$$\nabla f = mag(\nabla f) = \sqrt{G_x^2 + G_y^2} \tag{3.17}$$

The computing effort is minimized by calculating roots and squares as absolute values. The following approach for the calculation of the ∇f magnitude is applied. [59].

$$\nabla f \approx |G_x| + |G_y| \tag{3.18}$$

The pointing angle $\alpha(x, y)$ of ∇f at the point (x, y) is defined by:

$$\alpha(x, y) = \tan^{-1}\left(\frac{G_y}{G_x}\right) \tag{3.19}$$

where the final direction of an detected edge is perpendicular to the direction of the gradient vector ∇f at the point (x, y) [59].

Subsequently, a non-maximum suppression (NMS) technique is applied, to guarantee that a thickness of an edge contour does not exceed one pixel. The neighborhood pixels of the pixel with the highest magnitude are evaluated and separated within a defined hysteresis of lower and upper threshold values. A high ratio leads to less detected edges. A ratio of $2:1$ was chosen for the present work. The ratio is chosen by the user and is defined as:

$$Canny\ \ Ratio = \frac{Upper\ \ Threshold}{Lower\ \ Threshold} = \frac{2}{1} \tag{3.20}$$

The following figure 3.22 demonstrates the images after the individual edge-detection stages. Figure 3.22a illustrates the detected edges of the speckle-pattern after the non-maximum-suppression and figure 3.22b demonstrates the detected closed contours that are counted for the detection of amount of contours [59].

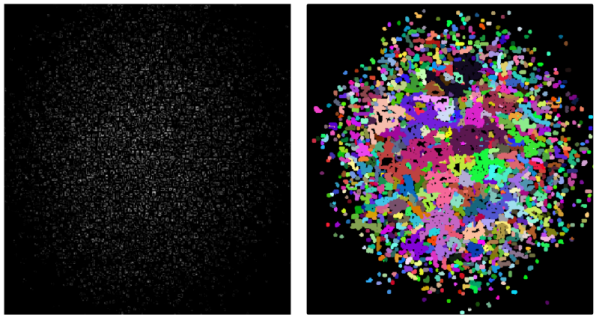

a) b)

Figure 3.22: Speckle-pattern for different edge-detection steps: a) Speckle-pattern after non-maximum suppression b) Detected closed contours.

3.5.5. Mean Intensity

The intensity in a defined region of the image is calculated in addition to the determination of the amount of speckle contours. This value represents a second parameter and can be utilized as a reference for the calculation of the bending angle. The mean intensity value of the ROI can be considered as a stable and reliable parameter according to its simplicity of calculation [59].

Definition of Mean Value

The mean value of the ROI is calculated by summing up all pixel intensities and dividing it by the total amount of pixel. The mean value represents the light intensity of the measuring signal and is defined as [59]:

$$\mu = \frac{1}{MN} \sum_{x=1}^{N-1} \sum_{y=1}^{M-1} f(x, y) \tag{3.21}$$

3.5.6. Mean Speckle Intensity Variation Technique

The additional speckle processing technique is utilized for comparison with the self-developed routine. The subtraction of images shows the moving part in images as described in [59]. The image processing technique is applied for the measurement of temperature by the analysis of the speckle-pattern in [13] and is characterized by simplicity and low computational effort. A reference image $f_0(x, y)$ is captured at the beginning of testing. All subsequent images $f_n(x, y)$ are subtracted from the reference image $f_0(x, y)$ and form the difference image $\delta f(x, y)$ that contains

the differences of the pixel intensities between both images. After each subtraction a scaling of the pixel intensity to the range of 0 to 255 is performed, thus image defects are eliminated [13].

$$\Delta f(x, y) = f_0(x, y) - f_n(x, y) \tag{3.22}$$

An integration of the difference image $\Delta f(x, y)$ leads to the integral image $F(x, y)$ of size M x N.

$$F(x, y) = \int_x \int_y \Delta f(x, y) \, \mathrm{d}x\mathrm{d}y \tag{3.23}$$

The mean value of the integral image serves as a unity for the correlation between the reference and the current image.

$$MSV = \frac{1}{MN} \sum_{x=1}^{N-1} \sum_{y=1}^{M-1} F(x, y) \tag{3.24}$$

The following figure 3.23 illustrates the image processing tasks performed for the MSV calculation as implemented in the source code.

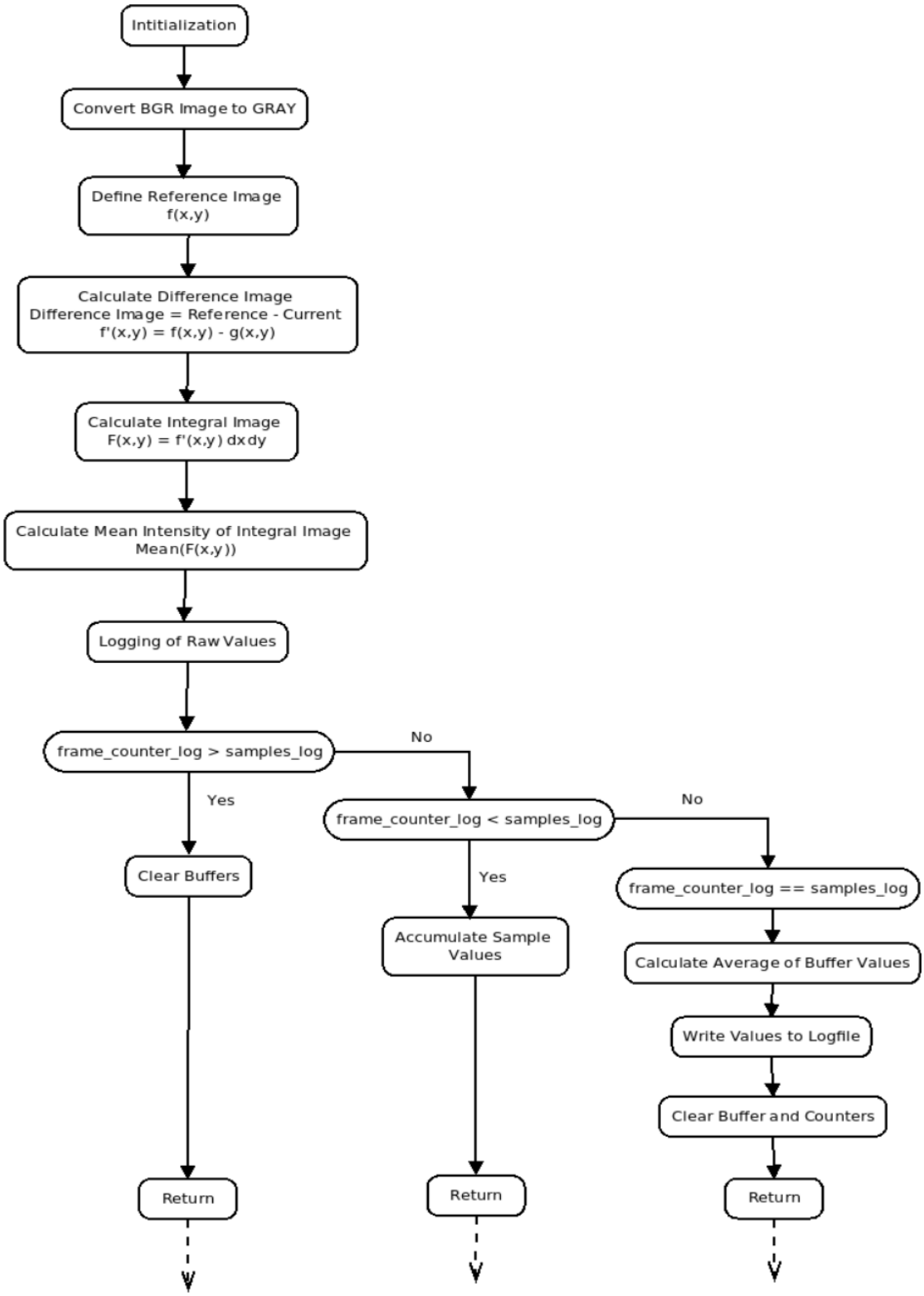

Figure 3.23: Structogram of MSV-routine as implemented in source code.

3.6. Measuring Procedures

3.6.1. General Description of Measurement Procedure

In this specific section, the term *Signal* substitutes the definition of the mean pixel intensity and amount of speckles. Both values are recorded and evaluated during all measuring procedures. The measurement results are presented and analyzed in the following section 4.

The quantity of speckles and the average value of the light intensity for different bending angles and geometrical arrangements of the the POF are recorded in a range of $-120°$ to $+130°$. The movement of the goniometer leg in left direction or clockwise is considered as the negative bending angle as depicted on figure 3.24. The measuring procedures were performed on the fivefold-, threefold- and a single-looped fiber arrangements with the experimental setup as described in section3.

The improved measurement setup for the two-times looped fiber arrangement was examined under the main aspects such as characteristic curve and repeat accuracy. Different measuring methods were performed for the identify the characteristics of the curvature sensor in static and dynamic operation.

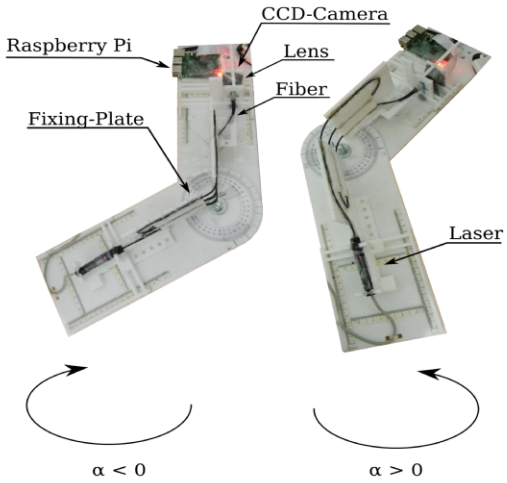

Figure 3.24: Detailed measurement setup with bending directions.

3.6.2. Characteristic Curve of Curvature Sensor

The characteristic curve of the sensor setup was determined by moving one goniometer leg in intervals of 5°. The angle position is maintained after each step for approximately three seconds to stabilize the signal.

3.6.3. Influence of Fiber Amount

The effect of the fiber arrangement on the amount of contours and light intensity during static and dynamic operation is investigated in the following section 4.

3.6.4. Influence of Region of Interest

The influence of the position and size of the ROI on the speckle-pattern is evaluated. The 500 x 500 pixel wide ROI is located over the entire speckle-pattern. For subsequent tests the ROI is reduced to 500 x 270 pixel array and located ones at the lateral side and secondly at the upper part of the speckle-pattern, according to figure 3.25.

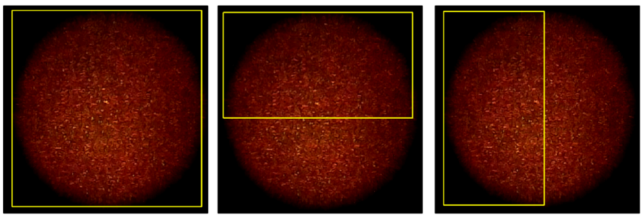

Figure 3.25: Different ROI placements on speckle-pattern: a) Entire speckle-pattern b) Upper half of speckle-pattern c) Lateral half of speckle-pattern.

3.6.5. Influence of Spatial Image Filters

The influences of the different spatial image filters such as *Gaussian Low-Pass filter*, *Bilateral filter* and *Image Averaging* are analyzed under the aspects of computational effort and improvement of contour detection.

3.6.6. Influence of Polarizer

The impact of a polarizer on the speckle-pattern is investigated by attaching it in front of the lens of the CCD-camera.

3.6.7. Influence of Temperature

The general effect of temperature on the signal response was tested for the two-times looped fiber setup. The fiber part of the measurement setup was heated by a hairdryer for a duration of 15 minutes. A significant temperature difference was sensible by hand contact. The intention is the achievement of the fundamental temperature influence on the signal response. Subsequent records of the amount of contours and the intensity before and after perturbation were performed and compared.

3.6.8. Influence of Mechanical Disturbances

The principle effect of mechanical disturbances on the detected amount of contours was investigated. The measurement setup is fixed during the test and a constant record of the amount of contours is performed. The measurement setup is perturbed by knocks on the measuring table in decreasing distances in relation to the goniometer and by wind, produced by a hairdryer, representing mechanical waves. The hairdryer is positioned closed to the free part of fiber bending points.

3.6.9. Repeat Accuracy over Long-Time Range

The repeat accuracy over a long-time range of the curvature sensor is investigated by the repetition of the aforementioned measurement procedure for ten times with a resting time of one hour between each trial. This test was performed for the fivefold- looped fiber setup.

3.6.10. Repeat Accuracy over Short-Time Range

The repeated accuracy over a short-time range of the curvature sensor is evaluated for the two-times-looped fiber setup. One leg of the goniometer is positioned to angles of destination in the range from $-120°$ to $+130°$. The bending angle is maintained for approximately three seconds and positioned back to the the zero-position. The procedure is performed five times for the bending angles $+50°$, $+70°$, $+90°$ in positive bending direction and $-50°$, $-70°$ and $-90°$ in negative bending direction.

4. Results and Analysis

The present section demonstrates the results of the measurement procedures, as described in the previous chapter 3. The system characterization is done by the detailed signal analysis of the measurement curves for the amount of contours and the intensity. The results serve as a basis for further researches and improvement of the measurement setup. The measurements on the test setups for the five-times-, three-times-looped-fiber and the single-fiber were performed initially. The results were analyzed and a final improved measurement setup, the two-times-looped fiber setup was developed.

The general finding of the experimental results says that the determination of the amount of speckles works reliable in the static operation and is perturbed by noise in the dynamic operation while the intensity of the speckle-pattern is slightly influenced.

4.1. Results

4.1.1. Measurement Results of Characteristic Curve

The bending form of the fiber is nonlinear over the entire angle range for all measurement setups, as depicted on figure 4.1 and 4.2. That condition explains the asymmetric shape of the characteristic curves. The bending in the positive direction of the first three test setups induced a slight signal attenuation, traced back to the displacement of the bending points in relation to the bending axis of the goniometer. That effect produces the fiber bending form as depicted on the following figure 4.1.

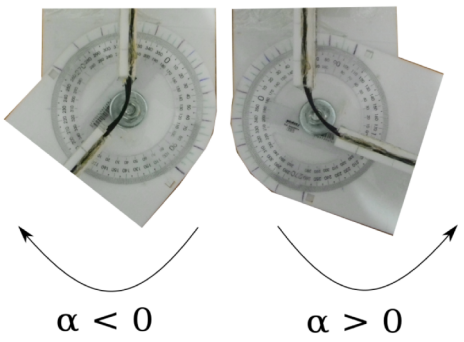

Figure 4.1: Detailed view of bending points of threefold-looped fiber test setup.

The bending in negative direction of the two-times-looped fiber setup leads to a stronger signal attenuation arising from the narrower bending shape of the fiber at a bending angle of 120°, as proven on the following figure 4.2.

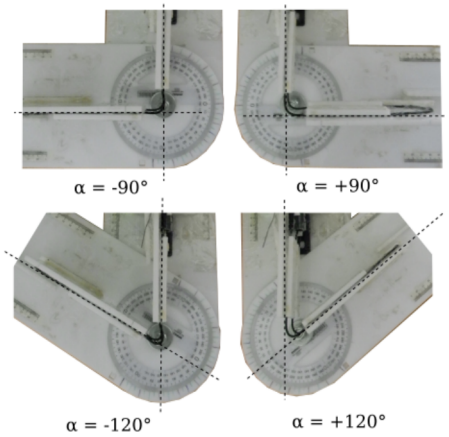

Figure 4.2: Detailed view of bending points of two-times-looped fiber test setup.

4.1.2. Graphs of Measurement Curves

The listed graphs demonstrate the measurement results for the amount of contours and the intensity of the four test setups in the bending angle range from −120° to +130°. The order of the graphs represent the chronological executions of the tests, where the final test setup of the two-times-looped fiber incorporates all improvements, as discovered with the results of the first experimental setups. The results presented in the current section were performed with the measurement procedures and equipment as described previously in chapter 3.

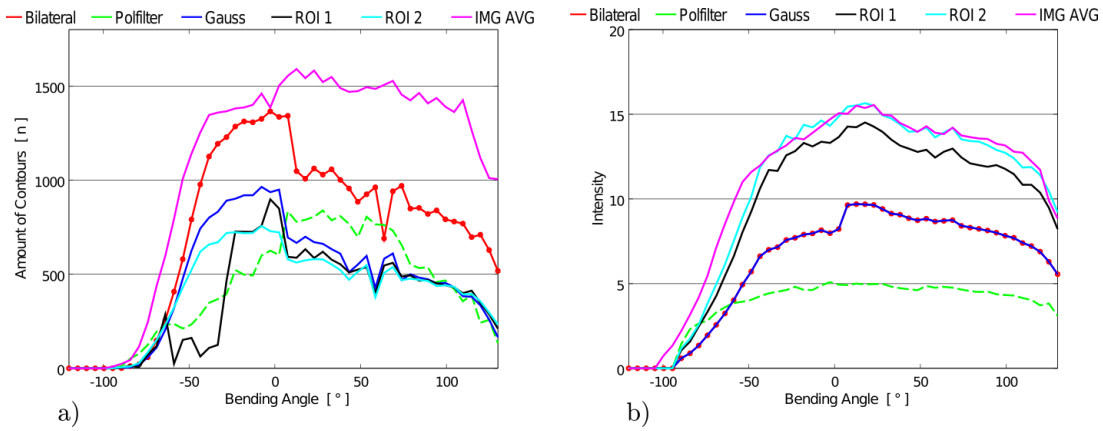

Figure 4.3: Measurement results of fivefold-looped fiber setup: a) Amount of contours versus bending angle b) Intensity versus bending angle.

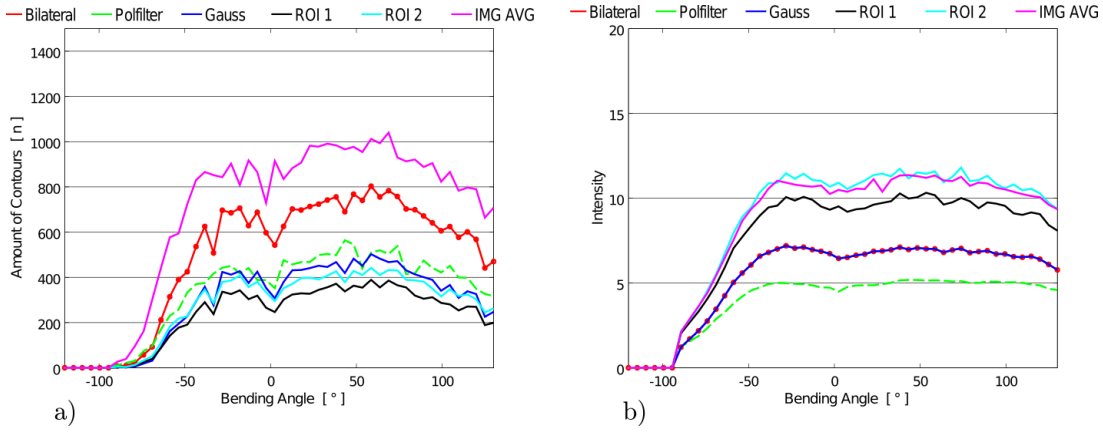

Figure 4.4: Measurement results of threefold-looped fiber setup: a) Amount of contours versus bending angle b) Intensity versus bending angle.

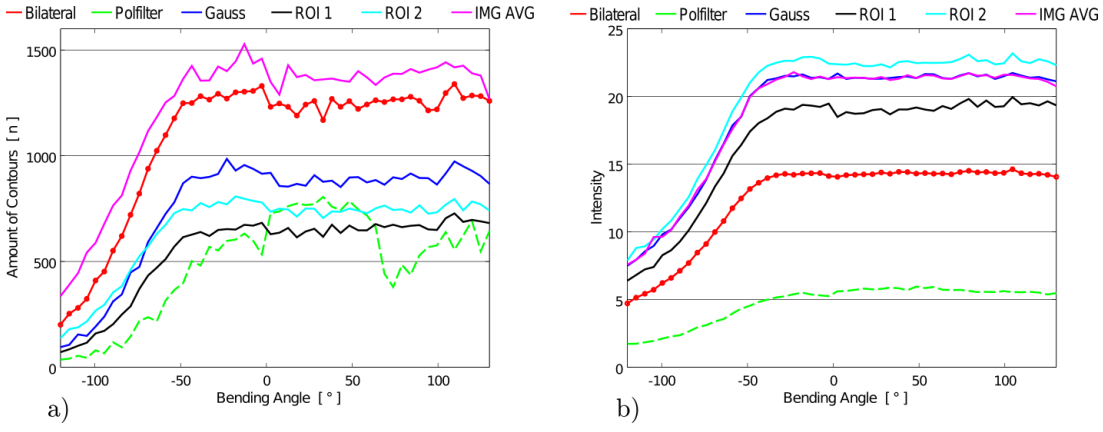

Figure 4.5: Measurement results of single fiber setup: a) Amount of contours versus bending angle b) Intensity versus bending angle.

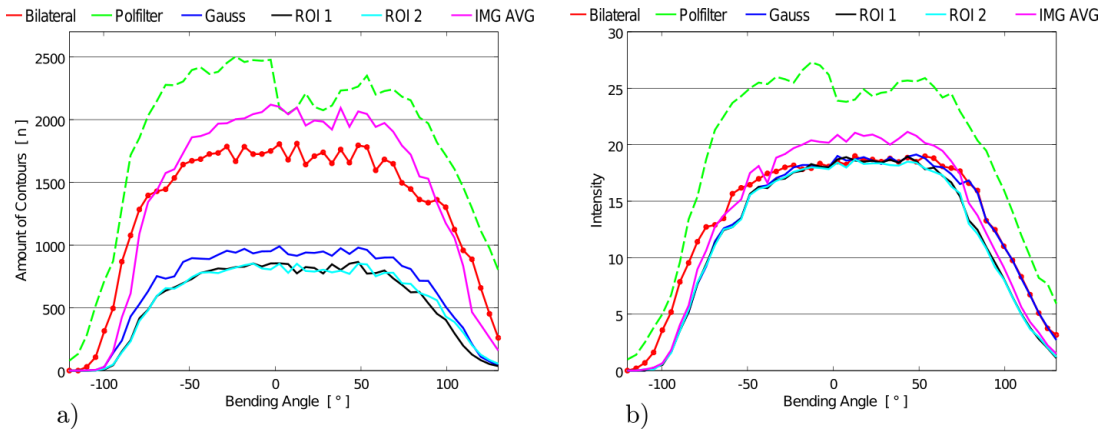

Figure 4.6: Measurement results of twofold-looped fiber setup: a) Amount of contours versus bending angle b) Intensity versus bending angle.

As described in the chapter 3, the measuring curves are all asymmetric, except the two-times-looped setup. The displacement of the bending point on the bending axis causes the fiber to bend in different forms for both bending directions, as in the case for the first three setups. That effect is applicable for the bending direction detection. The measuring curve of amount of speckles as a function of the bending angle demonstrates a higher gradient in clockwise direction. This effect is eliminated in the two-times looped fiber test setup where the characteristic curve demonstrates an almost symmetric shape.

The amount of contours curves constitute of a rough shape in comparison to the intensity of the speckle-pattern, as demonstrated on all figures from 4.3 to 4.6. The fluctuation of the individual speckles intensities in the speckle-pattern are crucial for this effect and leads to stepped values of the detected amount of speckle contours. The intensity value of the whole speckle-pattern is almost constant in static static operation and the curve describes a smooth shape.

The absolute value of amount of contours of the threefold-looped setup is visibly lower than for the other test setups. This effect arises from the image parameters configuration that produces a lower intensity.

All graphs indicate an almost similar gradient for the negative bending direction, while the gradient of the positive bending direction differs. The fivefold-looped

setup generates a sufficient signal loss for a measurement of the signal loss in positive bending direction, by the high amount of bending points, while the second and third setup only induce a slight measurable signal attenuation. The two-times-looped setup takes advantage of the system improvements and demonstrates an almost symmetric curve shape.

The evaluation of different POF arrangements proved that the signal loss rises strongly with the increment of loops, as shown on the figure 4.3 of the first measurement setup. The amount of speckles and intensity for the fivefold- and threefold-looped fiber setups converge to zero at a bending angle of $-90°$. The fivefold- and threefold looped fiber setups depict a linear characteristic in the range from $-90°$ to $-40°$ and the single fiber setup in the range from $-130°$ to $-40°$.

4.1.3. Measurement Result Region of Interest

Different ROI positions on the image have no effect on the shape of the measuring curve, while the absolute value of the amount of speckles and the intensity declines. The rise of the intensity is traced back to the mean value calculation of the ROI pixel intensity. Less pixels with low intensity are present in the calculated ROI. The application of the ROI reduces the amount of detected contours by 40 % and the computational effort by 20 % and can be considered as a parameter for the improvement of computing time.

4.1.4. Measurement Result of Spatial Image Filters

The signal responses of the Bilateral filter prove that the information of the amount of edges is preserved, while the Gaussian Low-Pass filter diminishes the measured amount of speckles about 25 %. The amount of contours for the improved measurement setup is reduced by almost 75 % by the Gaussian Low-Pass filter. The intensity is not influenced by the spatial filters. The computational effort for the utilization of the bilateral filter is 20 % higher in comparison to the Gaussian Low-Pass filter. The image averaging routine preserves the information about the edges and demonstrates the highest amount of detected contours and intensity for all measurement setups. The edge detection is processed as the fastest one under

application of the image averaging technique.

4.1.5. Measurement Result of Polarizer

The shape of the measuring curve is significantly changed and the total amount of speckles and intensity reduced by the polarizer for all measurement setups, except the fourth setup. The image parameter *Brightness* is increased by the application of the polarizer according to the damping effect of the light intensity in the fourth measurement setup. The purpose is to prove that the polarizer has the main effect of damping the light intensity, which can be compensated by the adjustment of the image parameters. The polarizer produces a high step at the zero position for the amount of contours and the intensity in the results of the fourth measurement setup, as depicted on figure 4.6. Generally can be stated that the polarizer generates a similar effect as an optical diffuser in case of the present application.

4.1.6. Measurement Result of Temperature Influence

The effect of a temperature influence on the measurement was tested and the measurement curves are presented on the following figures 4.7 and 4.8. As it can be observed, the amount of contours and the intensity drop down for an ascending ambient temperature. The curve shape of the amount of contours is altered by the temperature influence, arising from the change in the mechanical flexibility of the fiber. The curve form of the intensity remains unchanged.

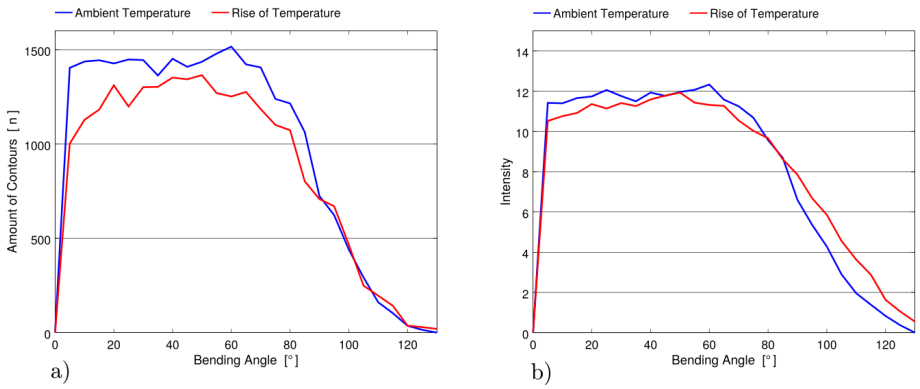

Figure 4.7: Measurement results of two-times-looped fiber setup under temperature influence: a) Amount of contours versus bending angle b) Intensity versus bending angle.

The following figure demonstrates the amount of contours as a function of the

bending angle range between 0° and +130° in steps of 5° before and after a temperature rise. The signal response is visibly disturbed by the temperature incline and indicates as strong flickering in the amount of contours and an alteration of the curve shape, as depicted on the following figure 4.8.

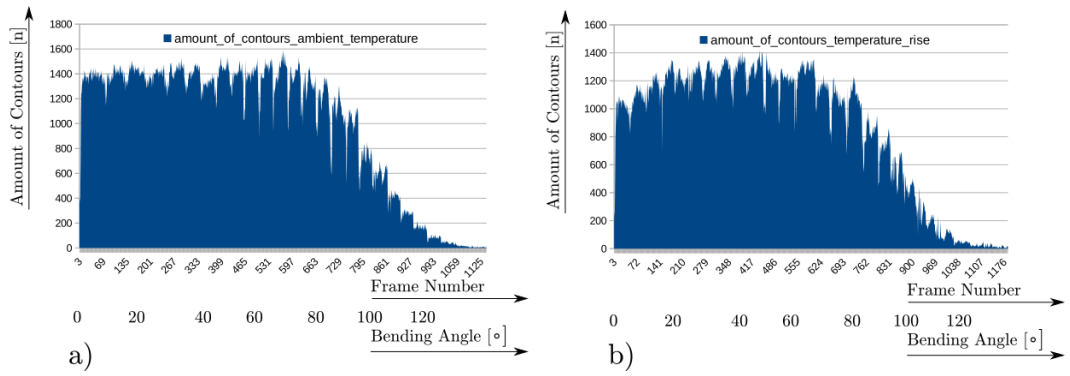

Figure 4.8: Measurement results of two-times-looped fiber setup under temperature influence: a) Amount of contours versus bending angle before temperature rise b) Amount of contours versus bending angle after temperature rise.

The temperature affects mainly the rigidity of the fiber and leads to a higher flexibility of the fiber, therefore the characteristic curve is changed after a temperature rise.

4.1.7. Measurement Results of Mechanical Disturbances Influence

The following figure 4.9 demonstrates the amount of contours over a time span, affected by knocks on the measuring table and wind produced by a common hairdryer. The moment of knocks are marked as numbers from '1' to '7', where at each knock the distance between the knocking position was diminished in relation to the goniometer.

The image of the speckle-pattern is affected strongly by mechanical shocks on the measuring table. The speckle-pattern image is strongly blurred as in case of the dynamic operation and avoids the correct detection of speckle contours. The knocks affect mainly the detecting device, the CCD-camera and secondly the loose fiber parts at the bending point.

The wind produced by the hairdryer, has a strong effect on the signal response

and prevents the correct measurement of contours, marked as '8', in the following figure 4.9.

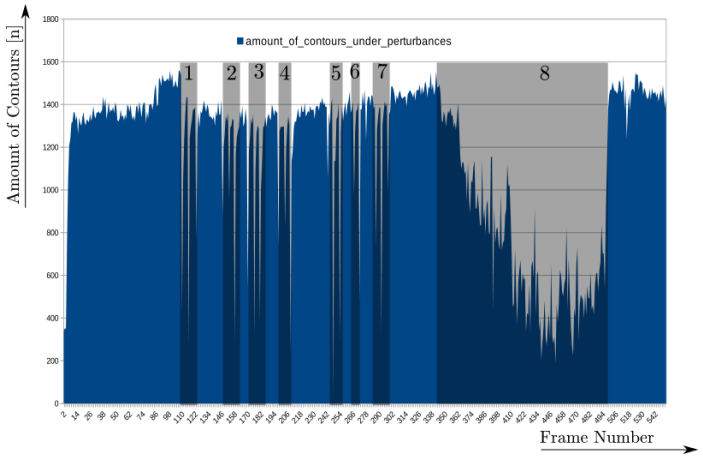

Figure 4.9: Measurement results of two-times-looped fiber setup under mechanical disturbances.

4.1.8. Measurement Result of Repeat Accuracy over Long-Time Range

The average standard deviation σ for the light intensity is $\sigma_{intensity} = 0.22$ and $\sigma_{contours} = 155$ for the amount of contours.

4.1.9. Measurement Result of Repeat Accuracy over Short-Time Range

The measurement results of the repeat accuracy over a short-time range from the two-times-looped fiber setup prove a high signal repeatability, as depicted on figure 4.10 and 4.11. The accuracy for the negative bending angles is higher than for the positive bending angles. The measurement of the intensity ensures a higher reliability in accuracy than the amount of contours, by the fact of the fluctuating values of the speckle intensities and the subsequent edge-detection.

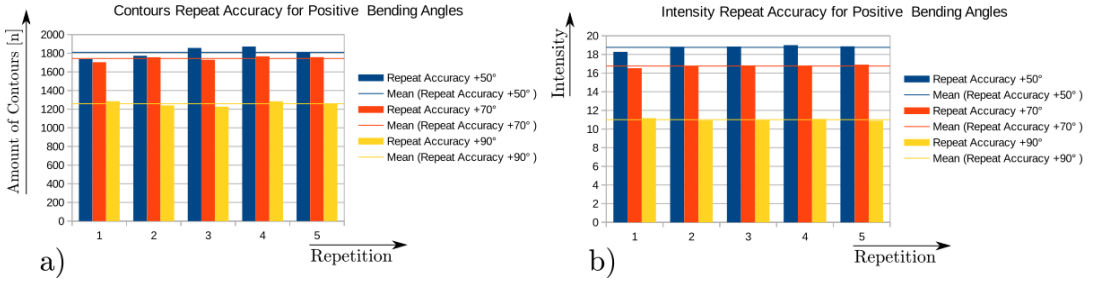

Figure 4.10: Repeat accuracy for positive bending angles of two-times-looped fiber setup: a) Amount of contours b) Intensity.

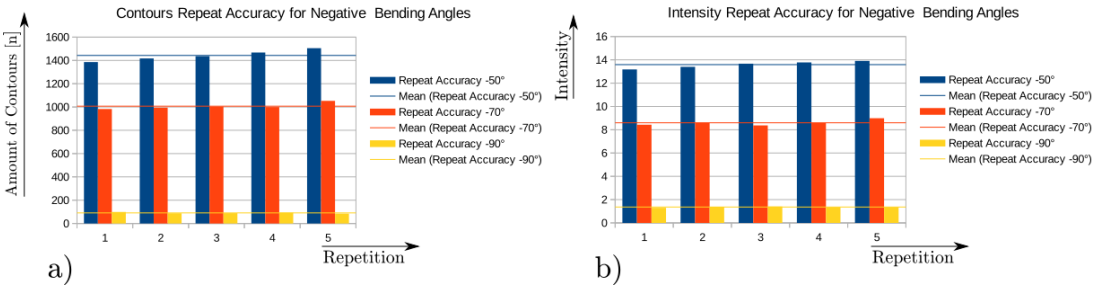

Figure 4.11: Repeat accuracy for negative bending angles of two-times-looped fiber setup: a) Amount of contours b) Intensity.

4.1.10. Measurement Result of Signal Delay

The delay time between the movement of the goniometers leg and the final calculated value was determined for a better system characterization.

40 frames with a resolution of 1296 x 972 and 8-bit depth are produced per second by the RaspiCam that corresponds to a data size of approximately 1.96 MB per second, is transmitted to the desktop computer via Ethernet. The RPI supports a transmission range of 100 $Mbps$ over Ethernet which yields to a transmission duration of approximately 167 ms to a desktop computer. The delay time between the movement of the goniometer leg and the calculated angle value on the desktop computer is almost 0.5 *seconds*, including the detection of amount of contours, the signal processing and transmission over Ethernet. The delay time can be reduced by including the image processing tasks on the embedded system, thus only the information about the current bending angle has to be transmitted to the desktop computer. Secondly, the image parameters can be changed for the generation of less image data.

4.2. Analysis

4.2.1. Signal Response in Static Operation

The signal of the amount of contours and the intensity varies strongly over the time, traced back to speckle noise. The fluctuation of the signal rises with a growing amount of fiber loops, lead back to tensile forces during bending and relaxing after bending. The variation of values depends on the temperature and an growing operation-time, as detected on the twofold-looped fiber setup. Differences of

about 60 contours between two contour values of the two-times-looped fiber setup in static operation were measured.

The following figure 4.12 illustrates the amount of contours of the three-times-looped fiber setup as a function of the bending angle during a goniometer leg position transition from 20° to 30°. The signal is visibly rippled and the movement induces a drop off in the amount of contours at the moment of the fastest goniometer leg movement. Slow movements between angle positions generate less disturbances, as noticed.

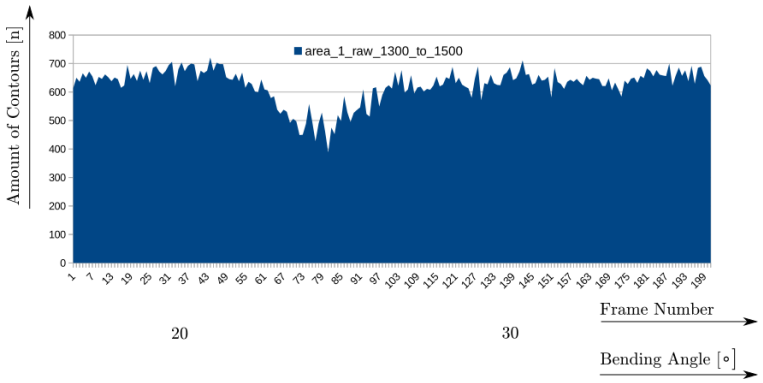

Figure 4.12: Signal fluctuations of amount of contours at dynamic transition between 30° and 40°.

4.2.2. Signal Response in Dynamic Operation

Distorted images and oscillating values for the amount of contours and intensity are detected during dynamic operation and shortly after moving the goniometer leg, as described previously. The mechanical memory and the rigidity of the fiber generate a major part of these disturbances besides the natural speckle noise. The bending characteristic of the fiber is affected by the core diameter, the material of core, cladding and jacket, the bending radius and the ambient temperature [6].

Figure 4.13 demonstrates the signal response of the amount of contours in the range from 0° to −130° degree in steps of 5° from the three-times looped measurement setup. The signal response is utilized as an example for further explanation under the focus of the signal characteristics.

The movement of the goniometers leg generates a rapid drop down of the amount

of contours and light intensity to an undefined value. The condition in dynamic operation is identifiable by the spared gaps between the bending angle positions on figure 4.13. The gap depth and shape varies for each movement as illustrated on the zoomed detail view on figure 4.14.

The effect is also noticed for the mean pixel intensity but the influence is less, as shown on figure 4.13.

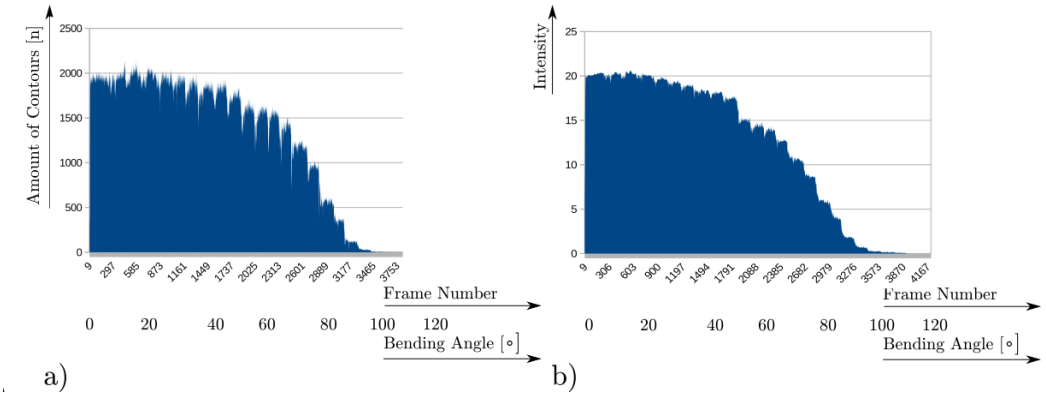

Figure 4.13: Signal fluctuation for positive bending angles: a) Amount of contours b) Intensity.

The following figure 4.14 illustrates a zoomed part of the raw measurement curve of figure 4.13 in the angle range from 0° to 60°. The varying shape of the spared gaps visible by observation. The depth of the gap width and depth varies for each transition.

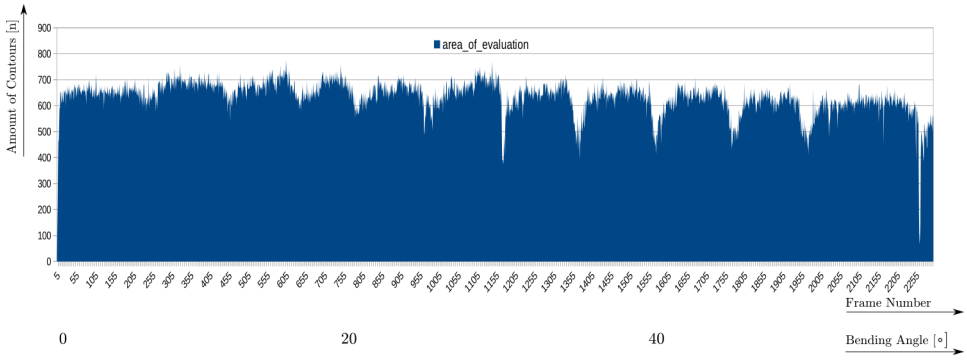

Figure 4.14: Signal fluctuations in dynamic operation.

A certain stabilizing time of the amount of contours is identifiable on the following figure 4.15 and figure 4.16 after a leg movement. The gaps are characterized by a falling and a rising time in relation to the mean value.

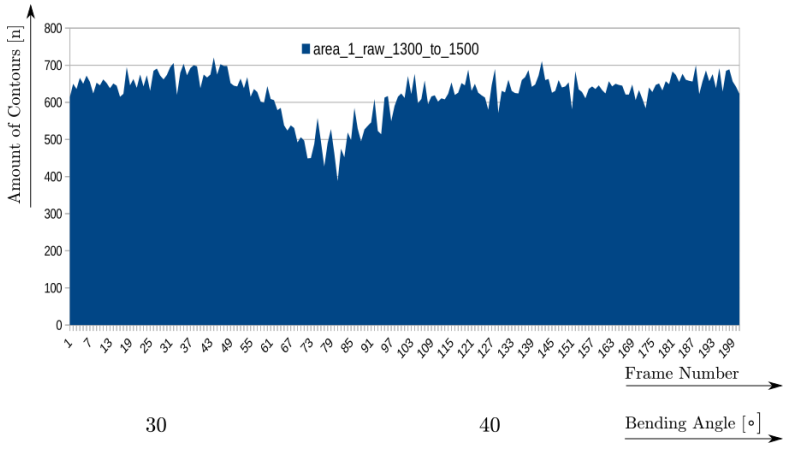

Figure 4.15: Signal fluctuations in dynamic operation first detail view.

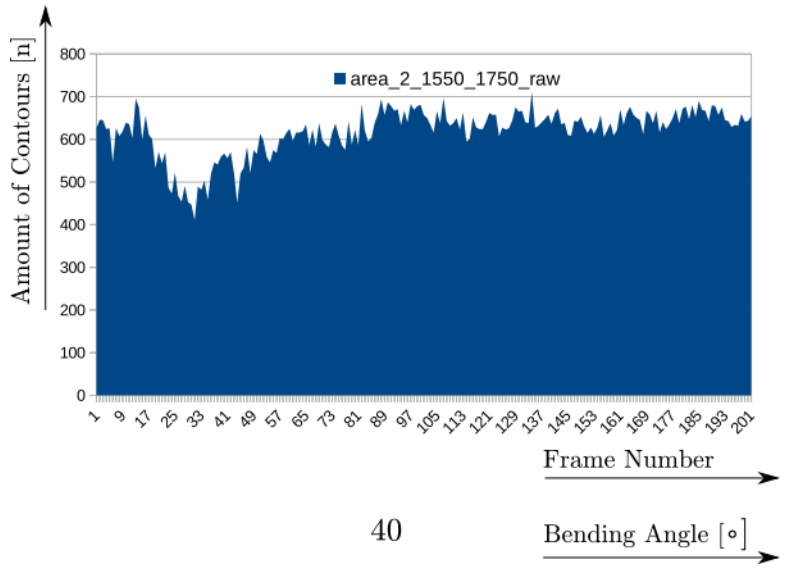

Figure 4.16: Signal fluctuations in dynamic operation second detail view.

The occurrence is comparable to a voltage transition, provoked by an actuated mechanical electronic switch. Several techniques for the compensation of transients exist in the field of digital signal processing. In the present work, the effect is compensated by a self-developed digital signal processing routine as described in chapter 5.

The resulting value inside a gap and the gap depth depends on the the parameter *Canny threshold* that determines the sensibility of the edge detection. The Canny threshold in the current measuring curve is configured to 40. The amount of contours rises for an lower value of the Canny threshold while the visibility of gaps improved for a higher value.

4.2.3. Interference caused by Measurement Setup

The first measurement setup, described in section 3, was built with the intention to measure the curvature of a bent POF with the aid of speckle image processing. The measurement results were presented previously in section 4. During the performance of measurements some imperfections in the measurement setup were detected, characterized as signal distortions, imprecision and deviations in the measurement results. The whole measurement setup was analyzed under the aspect of the detection of signal distortion origins. The experimental setup was clustered schematically into individual parts for their separate evaluation. The knowledge of the imprecision origin ensures a improvement of the measurement setup.

A schematic of the whole system divided in separate parts is depicted in the following figure 4.17.

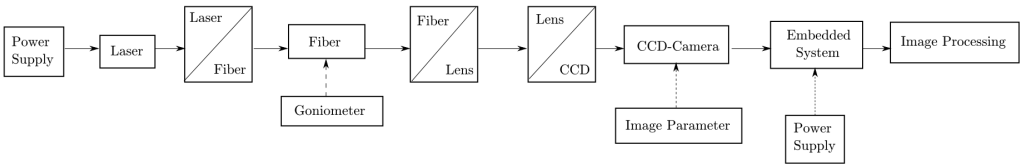

Figure 4.17: Sources of signal disturbance in the measurement setup.

All components in the signal processing chain are analyzed by its known characteristics.

Light Source

Fluctuations of the power supply result in a variation of light emission power. The utilization of a battery reduces this effect significantly. The ambient temperature causes a shift of the spectral wavelength with an growing operation time of the emitted laser light. This effect is comparatively low and not detectable in the current measurement setup therefore it is neglected.

Optical Coupling Laser-Fiber

The optical coupling between the laser and the fibers input represents a major point of signal loss in the present test setup. The laser posses a certain emitting area and the fiber a defined acceptance area, the numerical aperture. The emitting and acceptance areas must coincidence for a maximum light transmission. Both areas can be overlapped by the adjustment of the distance between these components.

Improvement of light coupling between the laser and the POF is achieved by collimating lenses which bound the out coming light to a definite incident angle as depicted on figure 4.18.

The angle of emission can be controlled by the distance adjustment between the laser-Lens and lens-POF. The same coupling method can be utilized for the optical coupling between the the fiber output and the CCD-camera.

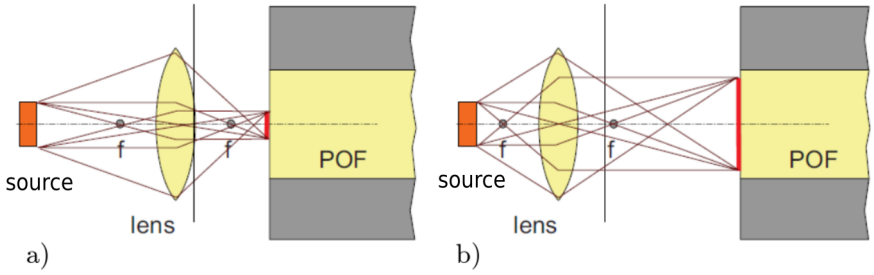

Figure 4.18: Principle of light coupling improvement by a lens: a) Reduction of lighted area b) Enlargement of illuminated area [6].

The anchor of the laser facilitates displacements in the mm-range in all directions and leads to misalignment between the laser and the POF input face. Signal attenuation is generated by emitted light outside the fibers aperture angle.

Figure 4.19 and figure 4.20 demonstrate the distribution of light losses at an optical coupling point. Light reflection is caused on the front fiber surface that is not coupled directly into the fiber core. A part of the light impacts the Jacket and gets absorbed. A portion of the light that lies outside the acceptance area passes the wave guide.

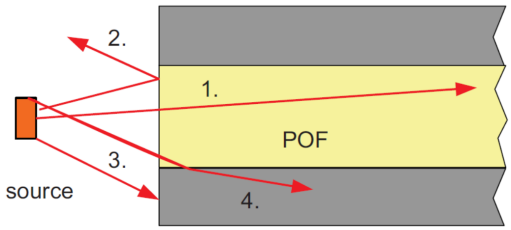

Figure 4.19: Coupling Losses : 1) Correct coupled light, 2) Light reflected at the front surface, 3) Light outside of front surface, 4) Light outside the acceptance range of fiber, [6].

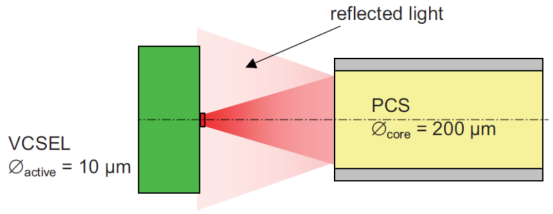

Figure 4.20: Coupling losses at an optical coupling interface [6].

The attenuation generated by cladding losses amplifies with an ascending angle of incident for the entering light rays as depicted on the following figure 4.21. The effect is influenced by the numerical aperture.

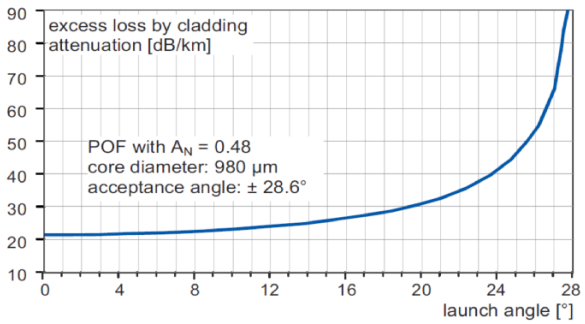

Figure 4.21: Signal attenuation versus launch angle [6].

The refractive index of the medium between the laser and the POF demonstrates a origin of losses. The roughness of the surface on the fiber input face causes microscopic scattering waves known as modal noise as described in 2.5.4 and represent an additional loss and increases for a higher surface roughness. Dust, pollutants and oily marks on the laser lens cause significant loss in light transmission.

Polymer Optical Fiber

The origins of signal attenuation and losses generated by the POF are described detailed in subsection 2.3.

The type of fiber guiding on the fixing plate influences the signal response significantly. The fiber experiences different drawing forces during the curvature that provoke a displacement of the fiber, detectable by imprecision in the measurement results of the repeat accuracy. The fiber is not bent circular during curvature by the stiffness of the fiber as discovered in [10]. This fact causes a non-linear curving behave leading to a nonlinear signal attenuation.

Optical Coupling POF-Lens

The optical coupling between the fiber output and the lens is influenced by the same effects as the optical connection between the laser and the fiber input. The fiber propagation axis is variable during curvature by the presence of lateral drawing forces. Imprecise coupling between the fiber output face and the lens is provoked. Modal noise induced by rough surface of the fiber end tip and is reduced by the utilization of polished connectors.

Optical Coupling Lens-CCD

The optical coupling between the lens and the CCD-camera depends on the alignment and the relative position in reference to the CCD-camera. A decreasing distance between the components generates a enlargement of the projection plane on the CCD-camera.

Dust and oily marks induce significant changes in the received image of the speckle-pattern. Ambient light has a strong influence on the signal response. In case of highly illuminated ambient, the detected amount of contours is less than in a sufficient illuminated room. The disturbance is eliminated by covering the optical connection of the lens with the CCD-camera.

CCD-Camera

The CCD-camera is influenced by varying ambient light levels and light of fluorescent light tubes, besides the wavelength of received light. Periodic noise in images is generated by electrical or electromagnetical interference, affecting the image quality [59]

The cameras measuring characteristics changes with an growing operation time and temperature rise, as noticed during the measurements. The amount of contours changed for the same measurement setup over an growing operation time.

The resulting image of the speckle-pattern is individually adjustable by the main parameters *ISO*, *Brightness*, *Shutter Speed*, *Exposure Time*, *Saturation*, *Sharpness* and *Contrast*. The parameters are adjusted with the intention of improving the visibility of speckle contours.

Image Parameters

A closer distance between the CCD-camera and the fiber end face produces a brighter image and higher amount of contours. The characteristic curve is influenced by the distance between the CCD-camera and the fiber end face. The amount of contours is almost constant during a fiber curvature for a minor distance, by the fact of a high amount of detected speckles. A certain amount of contours for the zero-position of the goniometer has to be configured by the adjustment of image parameters, to achieve a measurable decline during curvature.

The generation of an adequate speckle-pattern image by the adjustment of image parameters for the curvature measurement requires a certain experience.

The brightness and the shutter speed values are raised under application of a polarizer or diffuser to values of '30' and '3000' respectively, for the two-times-looped fiber setup. An increase of these parameter values is necessary for a higher amount of fiber-loops. A growing brightness generates an swelling diameter of the speckle-pattern circle and a higher amount of speckles. The effect of this parame-

ter is immediately visible in the final image and primary applicable in the case of a polarizer or diffuser.

The shutter speed is carefully applied by the to avoid a saturation of the CCD-chip, characterized as white areas in the speckle-pattern image while a low value hides the contours in the image. A higher amount of shutter speed and ISO generates more fluctuations in the amount of contours detection and higher sensibility to mechanical vibration.

The saturation parameter affects mainly the red light part of the image and leads to an declining amount of contours by its gain. The contrast affects mainly the amount of contours and is utilized as a main parameter for the rough adjustment of amount of contours. A high value blurs the image of speckle-pattern visibly.

All automatic effects are turned off during operation. The parameter *Automatic White Balance* has the strongest effect on the detection of amount of contours by the fact of the image luminosity adjustment that suppresses the detection of changes in speckle intensity variation.

The parameters *Brightness*, *Contrast*, *Saturation* and *Sharpness* are applied for a general adjustment of the image under the focus of generating a reddish illuminated speckle-pattern circle, containing a visible amount of huge speckle contours. The information about the color is not important for the detection of contours, only the edge information. Secondly the parameters *ISO* and *Shutter Speed* are applicable for the adjustment of the dynamics of the signal response to generate a stable image without flickering of the speckles.

Goniometer

The acrylic goniometer ensures a compact mounting of all moving components on the same point of reference. Some imperfections of the measurement setup were improved and resulted in the final setup of the twofold-looped fiber setup. The optical coupling points Laser-POF, POF-Lens and Lens-CCD-camera were also

improved.

Embedded System

The Embedded System is responsible for the recording of the speckle-pattern images and their transmission over Wi-Fi to the desktop computer. The images are recorded in real time. The Wi-Fi transmission depends on various factors such as connection speed and quality, transmission power of the Wi-Fi pen drive and the the current charge of the RPI-OS by background processes.

Image Processing

The image processing tasks are realized by the desktop computer with the aid of the computer vision library *OpenCV 2.4.9*. The visualization of the processed images on the screen is utilized as a debugging function. The computing time is reduced to 20% by turning off that feature.

The parameters of the spatial filters and Canny-edge detector are adjustable for a minimum computational effort. A major factor for computing time is the dimension of the filters kernel size and filter depth.

The programming style is a concerning variable factor for the improvement of computing time and represents a huge system variable.

Running background processes of the operating system are not all controllable. The operational system *Ubuntu 14.10* is capable to realize real time tasks.

5. Final Signal Processing Implementation

The signal response of the amount of contours and intensity posses a constant fluctuation in static operation and a certain stabilizing time after the movement of the goniometer leg, as investigated in the previous chapter 4. The calculation of the bending angle generates wrong values by the presence of that condition. The rapid falls of the amount of contours and intensity represent a difficulty for the the signal processing. The values of the amount of contours and the intensity are continuously logged and afterwards evaluated for the determination of the bending angle. The reliability and precision of the calculated angle was improved by the utilization of a self-developed digital signal processing method.

The focus of improvement is concentrated on the characteristic curve of the amount of contours. The negative influences of fluctuating values in static operation, in dynamic operation and transients in dynamic operation were analyzed in detail in the previous subsection 4.2.1.

The aforementioned signal disturbances are compensated by a self-developed algorithm that averages a certain amount of samples and sorts values that demonstrate a high difference in comparison to the previous value. The spared gaps between bending angle positions are identified and fluctuating values are smoothed by this method.

5.1. Averaging and Threshold Filtering Routine

The threshold function incorporates the comparison of the current value of amount of contours with the previous value by subtraction, as illustrated on the following figure 5.1. The absolute result of this subtraction is compared with a self-defined value, designated as *Threshold*. The value of threshold represents the depth of the gap between two bending angles or noisy values that are out of range. A low correlated value that exceeds the threshold value after subtraction is ignored. In practice a value of 150 contours for the threshold generated reliable results for the

two-times-looped fiber setup.

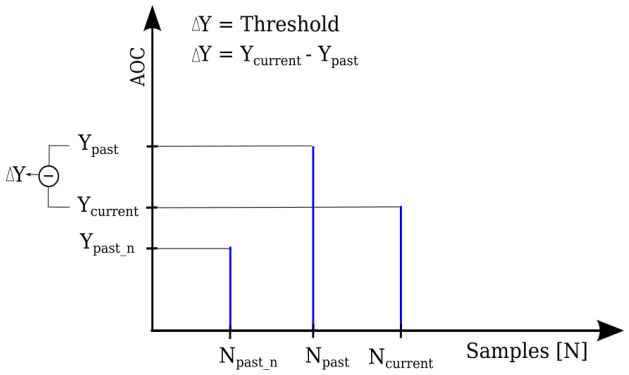

Figure 5.1: Working principle of threshold detection.

The method demonstrates a simple filter for the detection of false values, characterized by a low correlation in relation to the major part of values. The relative comparison of two values demonstrates a higher reliability than a comparison to an absolute value at an bending angle position. The sorting routine ensures the elimination of wrong values that could falsify the subsequent average calculation.

Subsequently, the routine simply takes the average of a defined amount of samples and generates a smoothed curve for the amount of contours. A value of 10 samples for the average, proved reliable results in practice. The following figure 5.11 illustrates the performed processing stages of the self-developed averaging routine including the threshold-detection, as implemented in the source code.

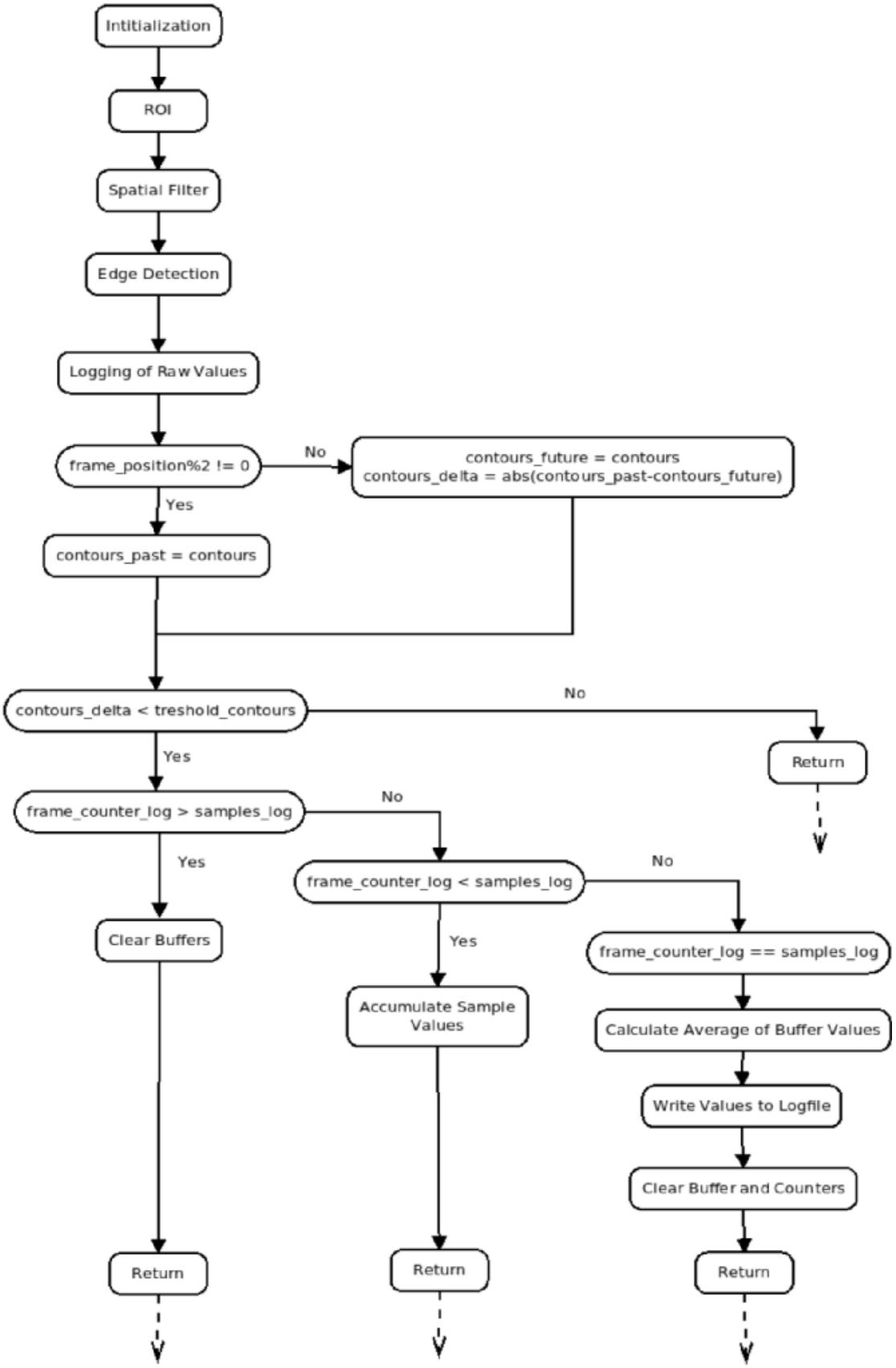

Figure 5.2: Structogram of averaging and threshold filtering routine as implemented in source code.

5.1.1. Results of Averaging and Threshold Filtering Routine

In the current section, the influences of both parameters of the digital signal processing routine are demonstrated. The first parameter is the amount of samples that is utilized for the average calculation. A high amount of samples smooths the curve significantly and leads to a higher delay in the signal response between the captured and the final averaged value, by the accumulation of samples. The video stream is recorded at a frame rate of 40 fps, an averaging of ten samples leads to a signal delay of 0.25 s. The averaging is important for the improvement of the signal response of the amount of contours.

The second parameter is the value of threshold that determines the maximum difference between two subsequent values of amount of contours. A high threshold value leads to less values that are ignored and the amount of low correlated values is not diminished noticeable. A low threshold value leads to a strong decreasing of amount of values and less values are present for the accumulation of averaging values, leading to a longer signal delay.

In summary, the averaging of values compensates the fluctuations in the signal curve and the threshold value defines the accuracy of gap detection by sorting of false values.

The effect of the averaging and threshold routine on the example curve of the previous section 4.2.2, is demonstrated on the following figures 5.3 and 5.4. The main shape of the signal curve is almost unchanged and the flickering signal values are smoothed and filtered. The effect is comparable to an envelope of the raw signal curve. Additionally, the gap is more defined in shape and better detectable as a transition point. The example on two different transients gives a better impression of the effect of the digital signal processing routines working principle.

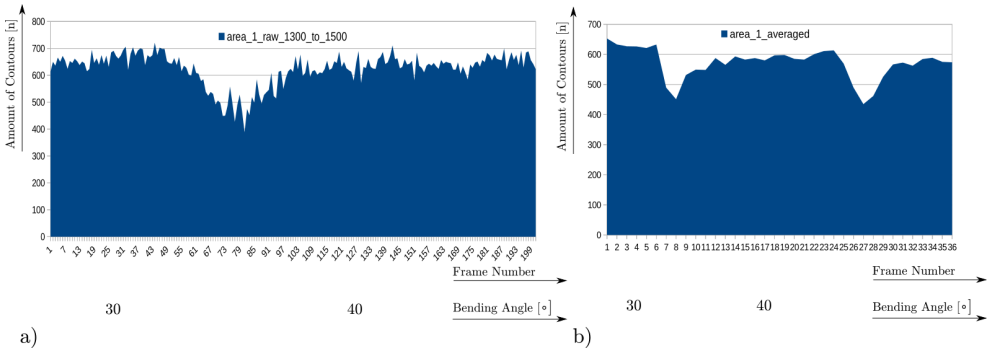

Figure 5.3: Effect of averaging and threshold detection on a transient: a) Raw measurement curve b) Averaged measurement curve.

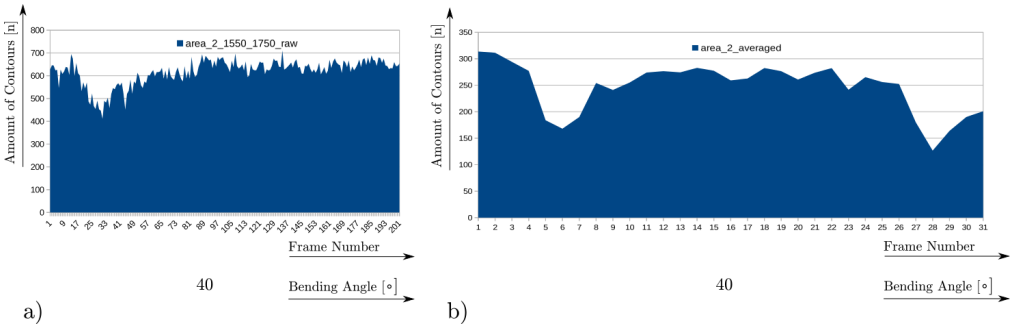

Figure 5.4: Effect of averaging and threshold detection on a second transient: a) Raw measurement curve b) Averaged measurement curve.

The effect of the Amount of Samples on Signal Response

The following figure 5.5 demonstrates the raw signal of the three-times-looped fiber setup for a bending angle range from 0° to 130°, as previously presented. Different values for the amount of averaging samples are applied and the effect on the signal response investigated. The amount of samples were defined to 5, 10, 15 and 20. The gap detection is switched off for these tests.

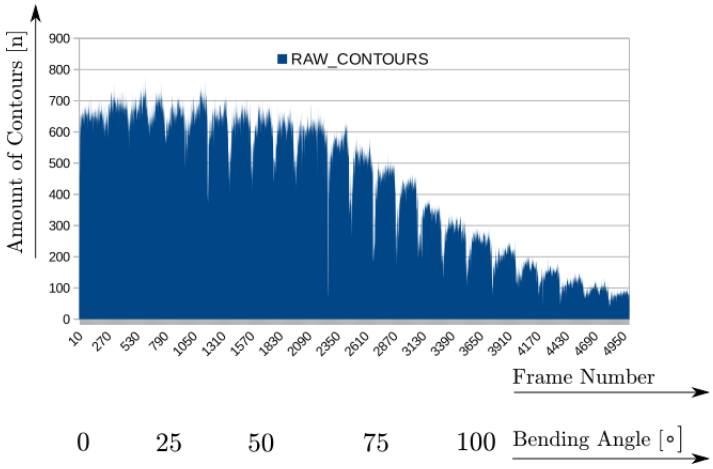

Figure 5.5: Raw signal of amount of contours as reference for averaging effect.

The amount of noisy values is released under application of 10 samples for averaging, as noticeable on the following figure 5.6. The utilization of 5 samples demonstrates only a slight difference in comparison to the raw signal.

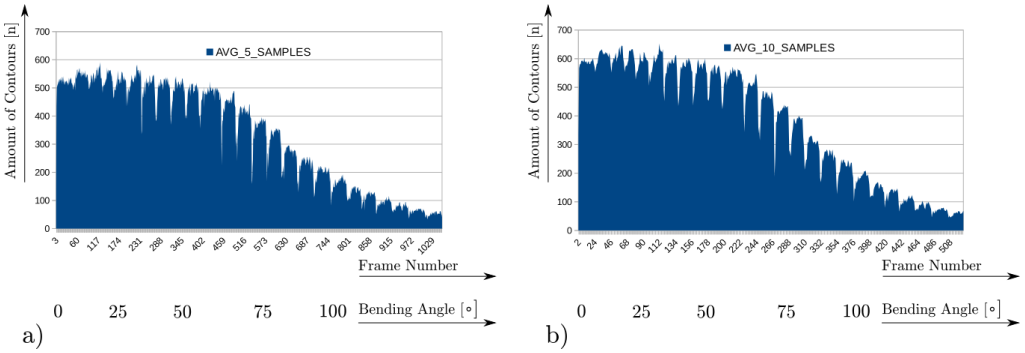

Figure 5.6: Effect of amount of samples for averaging on amount of contours: a) 5 Samples b) 10 samples.

The application of 15 samples demonstrates a visible enveloping effect on the curve and the absence of noisy values, as depicted on the following figure 5.7. The high amount of 20 samples induces strong smoothing of the curve and a grinding effect on the gap edges of the curve.

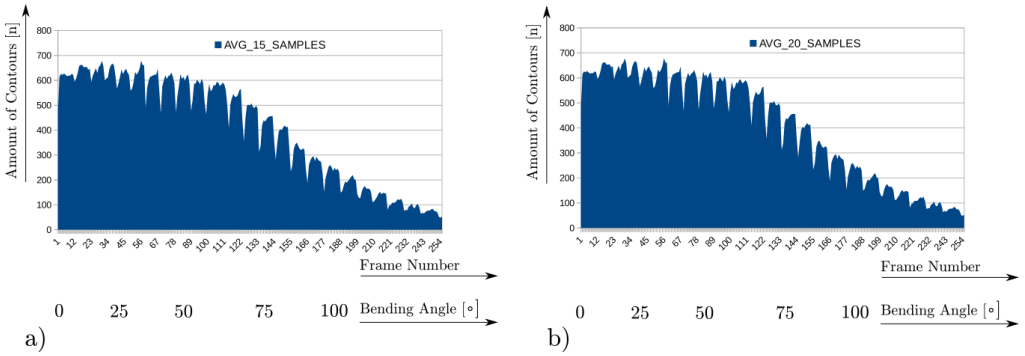

Figure 5.7: Effect of amount of samples for averaging on amount of contours: a) 15 Samples b) 20 samples.

The effect of the Threshold Value on the Signal Response

The effect of the amount of averaging values was investigated in the preceding part. The present part treats the filtering characteristic of the threshold value in combination with the amount of averaging samples. The reference curve of raw values on figure 5.8 remains unchanged. The amount of samples of 5 and 10 in combination with the threshold values 50 and 150 is applied on the raw measuring curve, as depicted on the figure 5.9 and figure 5.10.

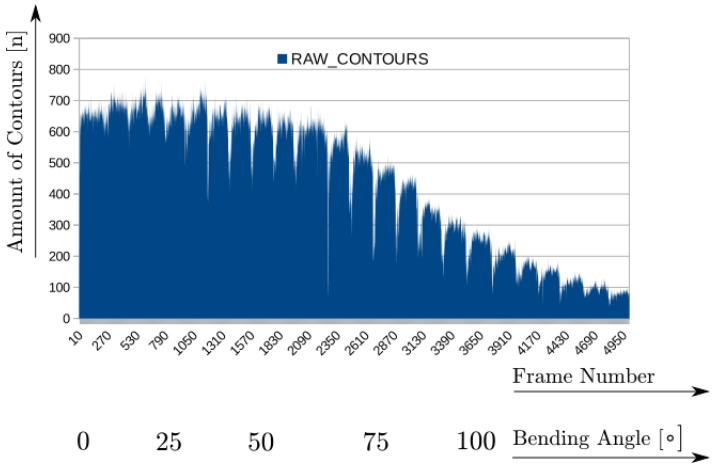

Figure 5.8: Raw signal of amount of contours as reference for averaging effect.

The low threshold value of 50 and the amount of 5 samples leads to a high rate of sorted values in the range from 0° to 60° as depicted on the following figure 5.9. The high amount of 150 of threshold affects the raw curve slightly.

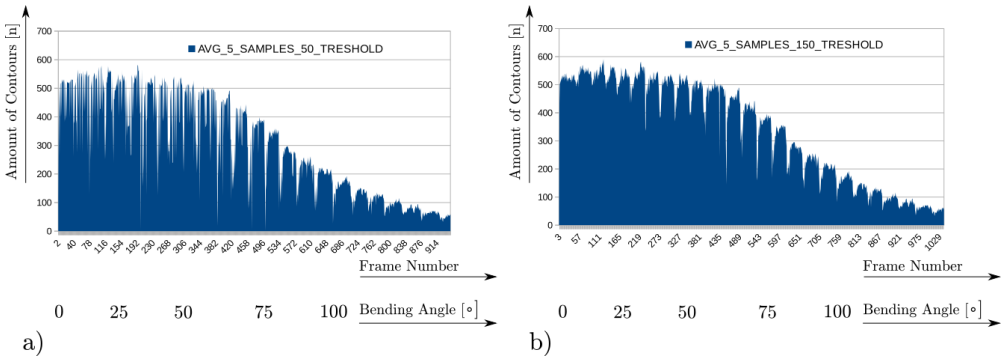

Figure 5.9: Signal comparison of five averaged samples with a) 50 threshold detection and b) 150 threshold detection.

The amount of 10 samples and low threshold value of 50 demonstrates a high rate of sorted values in the bending angle range from 0° to 60°, as depicted on the following figure 5.10. A reliable result is achieved by the choice of 10 samples and a threshold value of 150. The spared edges are preserved and the noisy values are filtered out, as proven on the following figure 5.10.

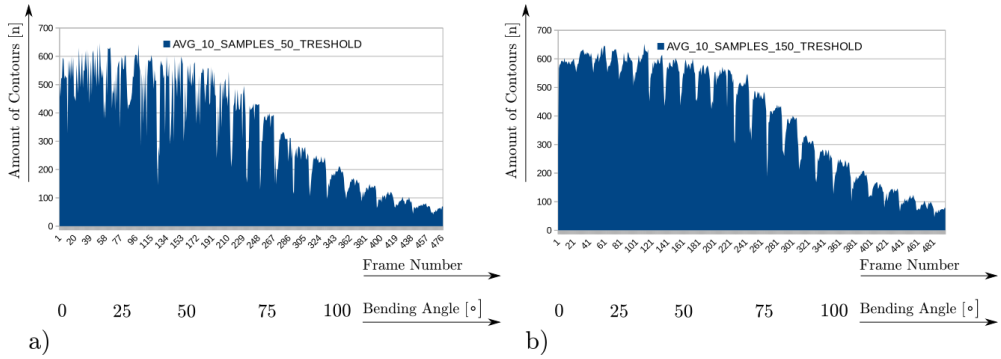

Figure 5.10: Signal comparison of 10 averaged samples with a) 50 threshold detection and b) 150 threshold detection.

5.2. Inversion Routine combined with Averaging and Threshold Filtering Routine

The signal processing routine was finally enhanced by an additional calculation that causes an inversion of the characteristic curve on the horizontal axis. A reference value for the amount of contours and the intensity is defined. All values of the amount of contours and the intensity are subtracted from the reference value and the curve results in its inverse.

The technique facilitates the ability to offset the signal curve and secondly, the values for the amount of contours and intensity ascend for a rising bending angle. The filtering routine achieves better results for the inverted curve, as will be presented. The following structogram on figure 5.11 represents the inversion routine as implemented in the source code.

Figure 5.11: Stuctogram of curve inversion routine combined with averaging and threshold filtering routine as implemented in source code.

5.2.1. Results of Inversion Routine combined with Averaging and Threshold Filtering Routine

The following images demonstrate the effects of the averaging and threshold detection algorithm on the example raw measurement curve. The raw curve, depicted on figure 5.12 left, is inverted and results in the curve on figure 5.12 right. Afterwards, the effect of the averaging routine with threshold detection with different parameters is applied and illustrated on figure 5.13. The figures show that the configuration of 10 samples and 30 threshold produce the less distorted shape of the inverted measurement curve.

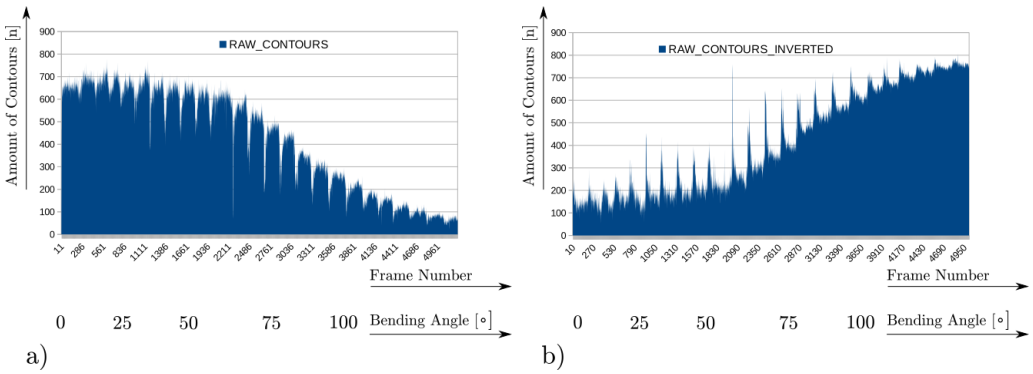

Figure 5.12: a) Raw measurement curve b) Inverted measurement curve.

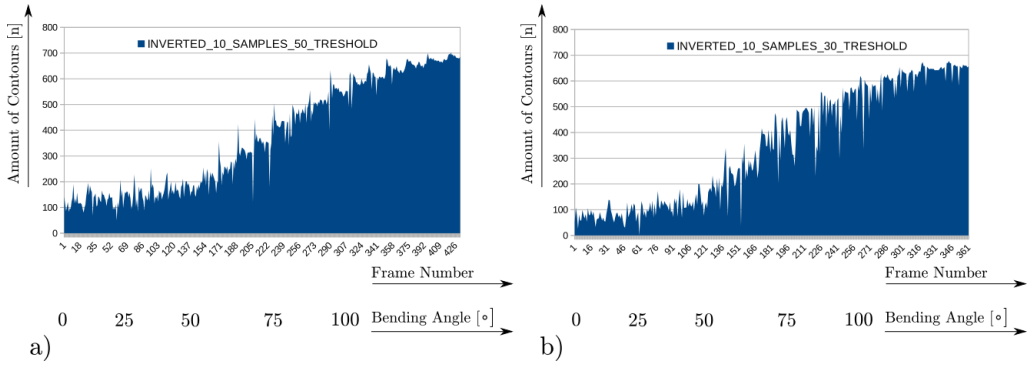

Figure 5.13: Filtering of inverted curves: a) 10 samples for averaging and a value of 50 of threshold detection b) 10 samples for averaging and a value of 30 of threshold detection.

5.3. Characteristic Curve over entire Bending Angle Range

The final characteristic curves that describe the amount of contours and the intensity as a function over the entire bending angle range from $-120°$ to $+120°$, are depicted on the following figures from 5.14 to 5.17. Each characteristic curve is mathematically describable by a polynomial of second or fourth order and that

is utilized for the final angle calculation. The curves are produced with the final setup of the two-times-looped fiber setup. The configuration of 10 samples for averaging and a threshold of 150 was configured. The graphs prove that the curve of intensities are smoother and more stable than for the amount of contours.

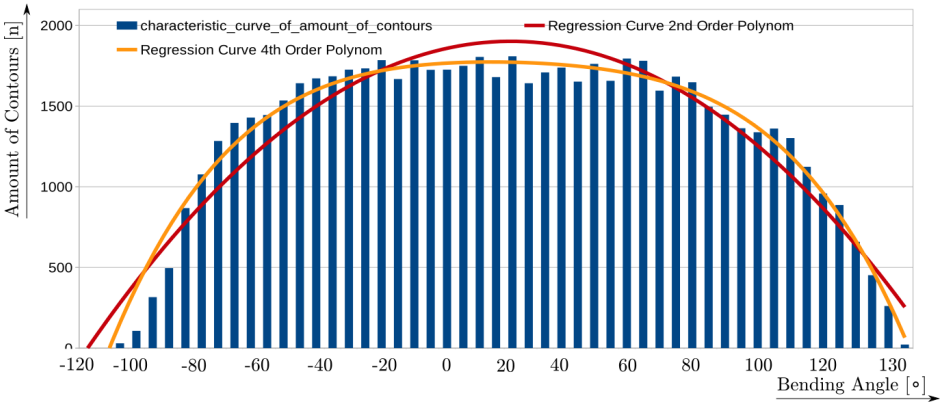

Figure 5.14: Characteristic curve of amount of contours over entire bending angle range with regression curves.

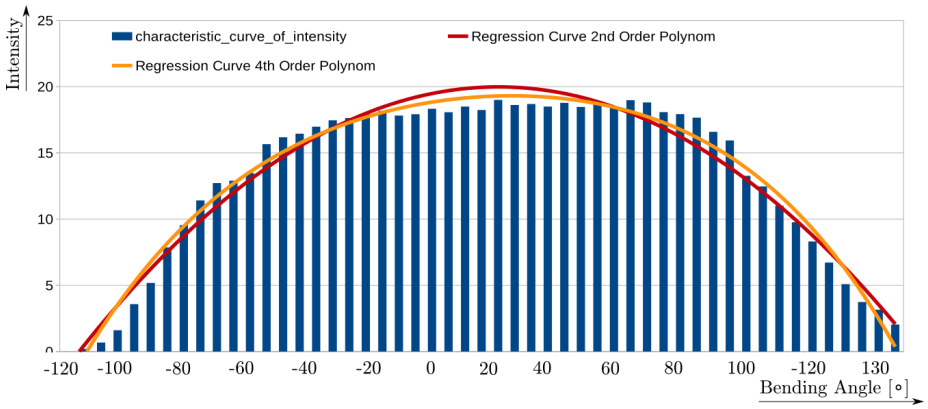

Figure 5.15: Characteristic curve of intensity over entire bending angle range with regression curves.

5.4. Inverted Characteristic Curve over entire Bending Angle Range

The following curves illustrated on figure 5.16 and figure 5.17 represent the inverted signal, processed by the signal processing algorithm under application of a bilateral filter, 10 samples for averaging and a value of 30 for the threshold detection. The inverted curves are applied for the final angle calculation under assumption of the polynomial of the 4th order. The main advantage of the inversion is the referencing of the values to a defined value. The curve can be modified and be offset by this

procedures. In case of a rising ambient temperature, the the absolute value of amount of contours can be changed by the reference value. The simplicity and low computing effort are the positive side effects of this procedure.

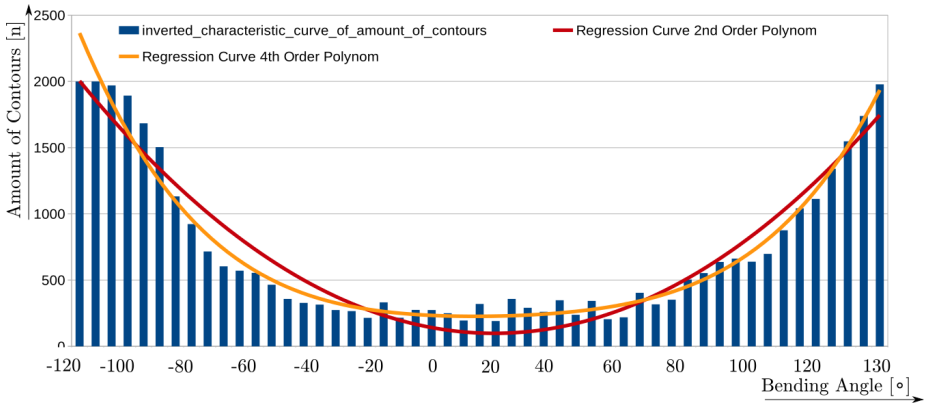

Figure 5.16: Inverted characteristic curve of amount of contours over entire bending angle range with regression curves.

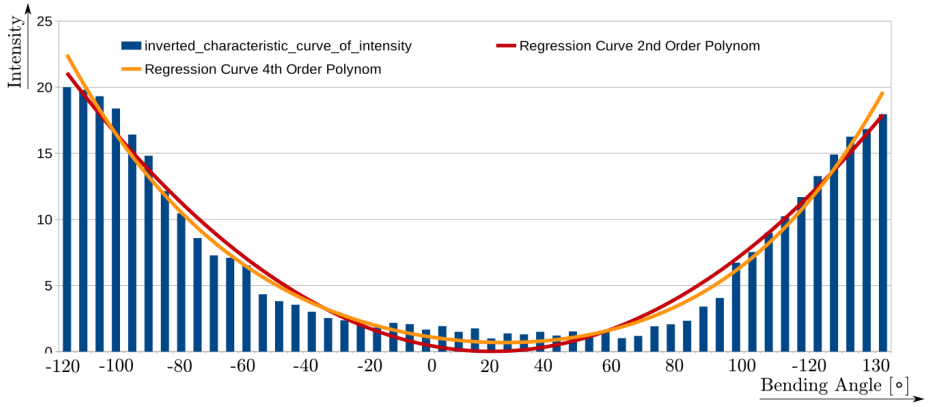

Figure 5.17: Inverted characteristic curve of intensity over entire bending angle range with regression curves.

5.5. Characteristic Curve of MSV - Routine over entire Bending Angle Range

The MSV routine was implemented and serves as a measuring technique for comparison with the self-developed one. The following curve on figure 5.18 demonstrates the value of the mean speckle intensity over the whole bending angle range. It can be observed that the curve posses an almost symmetric characteristic and can be approximated by an polynomial of 4th order.

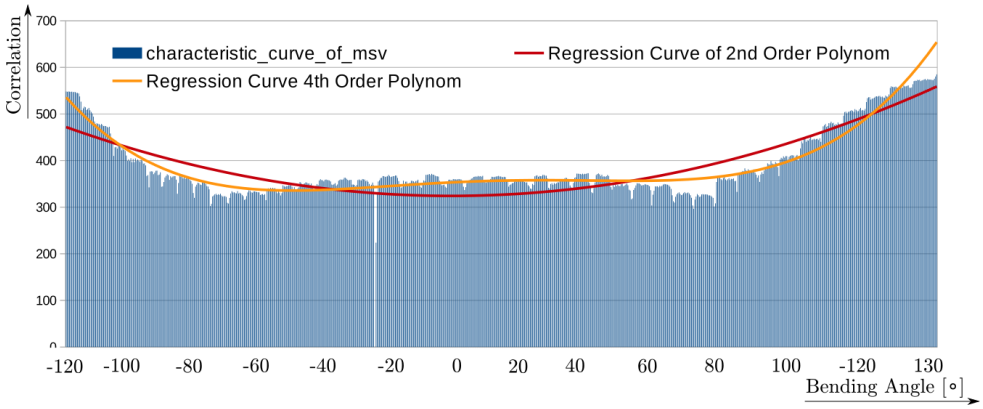

Figure 5.18: Characteristic curve of mean speckle intensity variation procedure.

6. Conclusion

6.1. Review of Research Results

In the present work, an elementary measuring technique with low cost-components and low computing effort for the determination of bending angles in the range from $-120°$ to $+130°$, based on the graphical analysis of digital speckle-pattern images is described. The research began at the basics, where general effects of the fiber under curvature were investigated and finishes with a precise measurement setup that produces reliable measurements of the bending angle.

A self-developed image processing technique for the counting of amount of speckle contours in a specified region in a digital speckle-pattern image was developed and an acrylic goniometer that facilitates the defined bending of the fiber for different fiber setups, was invented.

The fiber was arranged in different loop arrangements for the specification of the influence on the signal response and the sensor sensitivity. The test setup was varied by adding a polarizer in front of the CCD-camera. The accuracy of the measuring method was determined by the repeated bending of the fiber for the long-time and short-time ranges. The influence of the ROI on the final speckle-pattern image was investigated by the evaluation of the signal response for different ROI positions. The spatial image filters Gaussian Low-Pass filter, Bilateral filter and the Image Averaging technique were evaluated under the consideration of signal improvement. For comparison, the Mean Speckle Intensity Variation measuring method was successfully applied for the determination of the bending angle.

The influence of temperature and mechanical disturbances on the speckle-pattern was investigated by practical tests. A system identification was performed for the detection of signal disturbing origins and for the design of a signal processing routine. An improved measurement setup was developed on the basis of the results of the system analysis.

A special digital signal processing method for the noise reduction of the signal for the amount of contours and the intensity was developed. The second test setup demonstrated more reliable and precise measurement results, characterized by the signal response for the repeat accuracy measurement method.

The amount of contours is mainly influenced by the specific application of the filter type, where the image averaging technique achieves the highest number of contours and intensity. The image averaging technique seems more suitable as a filter routine for the present application, by the fact of the high edge detection rate and low computational effort.

The Bilateral filter routine preserves the information about the edges and demonstrates a high rate of edge detection. The high computational effort in comparison to the other spatial filters is noticed as an disadvantage.

The Gaussian Low-Pass filter represents a compromise between the rate of edge detection and computational effort.

The application of the ROI represents an adjustable parameter for the improvement of computational effort. The shape of the measuring curve remains unchanged by its application and the computing time is reduced. The ROI is applicable on different positions on the speckle-pattern for the evaluation image information.

The amount of loops affects the rate of attenuation traced back to the increased number of bending points. On the other side, the signal fluctuations are amplified for an ascending number of turns by the fact of tensile forces during bending and relaxing.

The final self-developed signal processing routine demonstrated improved results for the edge detection and characteristic curve shape. The effects of its parameters,

such as amount of averaging samples and threshold value were demonstrated. The signal processing analysis prove that the inverted curve includes a certain adaptability by its variation in the offset.

The MSV-routine served as a reference technique for the speckle-pattern analysis. The resulting curve is symmetric over the whole bending angle range. The measurement results of the self-developed measurement setup prove a reliable and almost symmetric characteristic curve over the bending angle range from $-120°$ to $130°$ and is comparable to the MSV-routine. The system of the curvature sensor based on the graphical analysis of the speckle-pattern could be identified and an appropriate digital signal processing routine for the compensation of signal fluctuations and disturbances was designed. The system posses a system delay of 0.5 seconds between a measurement occurrence of the goniometer until a final angle value is calculated.

The final measurement setup IV demonstrates reliable measurement results and produces a symmetric curve shape for the amount of contours and intensity over the entire bending angle range. The setup IV is the result of the measurement setup optimization based on the results of the system identification.

The application has the potential for a real-time application by the utilization of reduced image data.

6.2. Prospects and Future Development

The signal attenuation and numerical aperture varies for different fiber types with different core diameter of different manufacturers as described in section 2.2. A thinner core diameter reduces the signal loss and a higher NA induces a rise in the signal loss. The signal response for different fiber manufacturer alters over the wavelength. Several factors like the the elasticity and the core diameter influence the signal output, as explained in section 2.6. Further tests with fibers of different manufacturer and dimensions can be taken in consideration.

The characteristics of the digital camera has a strong effect on the visibility of the speckle- pattern. The *RaspiCam* facilitates the unlimited adjusting of the camera parameters. The influence of the CCD-camera parameters like *Resolution*, *Shutter Speed*, *ISO*, *Frame rate* and image effects can be inquired in depth to achieve higher accuracy for the contour detection.

Common web-cameras work with specific software drivers, created by their manufacturer. The parametrization is often limited by the driver and automatic functions such as *Automatic White Balance*, *Automatic Exposure* or *Automatic Histogram Equalization* do not allow any change by user. The auto calibration functions represent a limitation in the utilization of the camera and cause unpredictable system behave. The substitution of the Raspberry Pi by the IP-camera is imaginable and would yield in more comfort, less time consume and installation effort.

A more detailed study of the the temperature influences on the polymer optical fiber under curvature for the contour detection can be executed. The temperature causes a variation in the flexibility and transparency of the fiber. Experimental results in [19] proved the existence of relation between the bending losses of the fiber with the temperature, the bending radius and fiber manufacturer.

Measurement divergences according to temperature, electrical power fluctuations are detectable by a reference signal. A second web cam can be connected to the

RPI and the digital images of both are compared for an improved system identification. A reference signal is suitable for the determination of this influence, therefore the compensation of these disturbances is feasible. A photodetector as a reference signal for the detection of power fluctuations was utilized in [54] and [55].

The signal responses of two light sources with different wavelengths differ under perturbation, as discovered in [33]. The green light source with a wavelength of 532 nm posses a different signal response at the moment of perturbation in comparison to a red light source with a wavelength of 632.8 nm. This physical fact can be applied on the present sensor application. Two fibers with particular light wavelength are mounted in front of the CCD-camera for the simultaneous analysis of the speckle-patterns as realized in [35]

The image processing stages are realizable in the frequency domain to improve sensitivity and filtering characteristics. Filters applied in the spatial range facilitate the filtering of additive noise. Image blur is better filtered in the frequency domain, while EMC-periodic noise is suppressed [59].

A completely different measurement method, based on phase modulation. as described in [6], for the measurement of wing deformation is suitable. A deformation of the fiber induces a phase difference between a reference signal and the modulated signal that is propagated in the curved fiber. This approach is based on digital image processing and the measurement setup had to be adapted which has to be considered.

The measurement procedure can be automated by a stepper motor, as realized in [12]. Imprecision induced by the operator are eliminated and the precision of the bent angle is improved.

Several researches reported the sensitivity improvement of the curvature sensor by providing the fiber core with a sensitive zone as described in section 2.7.6. The effect of the sensitive zone on the speckle-pattern can be studied.

The signal response of a force sensor is improved significantly by the usage of an ANN as presented in [34]. The application of an ANN results in relatively low computing effort and the ability of adaption. A further sensor application should be adaptable according to the individual joint dimensions of human bodies and changing ambient influences. The disadvantage of the previous training procedure of the ANN has to be kept in mind.

The curvature sensor based on intensity modulation and the analysis of speckle-pattern was described in the present paper. A variety of curvature sensor applications exist in the industrial and medical field. The characteristic curve of the present sensor posses a parabolic shape. The signal response posses a certain delay after movement as discovered in section 4.2. In condition of a rapid joint movement, the information about the current bending angle would be delayed. The specific case has to be examined to determine if this effect is acceptable.

The measuring method works reliable in dynamic and static operation. The information about the amount of contours is utilizable for the static operation and the light intensity for the dynamic operation. The application of the sensor in the field of human joint movement analysis requires high precision and reliability under different ambient conditions. The influences of temperature and relative humidity on the signal response have to be characterized for their compensation.

A potential application for the measurement of human joint movement and posture in the medical field of rehabilitation is possible. The bending angle of a human knee, elbow or exoskeleton is measurable by this method. The curvature measurement for an application in the robotic field or industrial application is convenient.

Bibliography

[1] Mohd Anwar Zawawi, Sinead O'Keffe, and Elfed Lewis. Intensity-modulated fiber optic sensor for health monitoring applications: a comparative review. *Sensor Review*, 33(1):57–67, 2013.

[2] Joseba Zubia and Jon Arrue. Plastic optical fibers: An introduction to their technological processes and applications. *Optical Fiber Technology*, 7(2):101–140, 2001.

[3] Kamiar Aminian and Bijan Najafi. Capturing human motion using body-fixed sensors: outdoor measurement and clinical applications. *Computer Animation and Virtual Worlds*, 15(2):79–94, 2004.

[4] Jonathan M Williams, Inam Haq, and Raymond Y Lee. Dynamic measurement of lumbar curvature using fibre-optic sensors. *Medical engineering & physics*, 32(9):1043–1049, 2010.

[5] Dragan Z Stupar, Jovan S Bajic, Lazo M Manojlovic, Miloš P Slankamenac, Ana V Joza, and Miloš B Zivanov. Wearable low-cost system for human joint movements monitoring based on fiber-optic curvature sensor. *Sensors Journal, IEEE*, 12(12):3424–3431, 2012.

[6] Olaf Ziemann, Jürgen Krauser, Peter E Zamzow, and Werner Daum. *POF handbook: optical short range transmission systems*. Springer Science & Business Media, 2008.

[7] A Babchenko and J Maryles. A sensing element based on 3d imperfected polymer optical fibre. *Journal of Optics A: Pure and Applied Optics*, 9(1):1, 2007.

[8] Alberto Vallan, Alessio Carullo, Maria Luisa Casalicchio, and Guido Perrone. Static characterization of curvature sensors based on plastic optical fibers. *Instrumentation and Measurement, IEEE Transactions on*, 63(5):1293–1300, 2014.

[9] Gaizka Durana, Joseba Zubia, Jon Arrue, Gotzon Aldabaldetreku, and Javier Mateo. Dependence of bending losses on cladding thickness in plastic optical fibers. *Applied optics*, 42(6):997–1002, 2003.

[10] Felipe Jiménez, Jon Arrue, Gotzon Aldabaldetreku, Gaizka Durana, Joseba Zubia, Olaf Ziemann, and Christian-Alexander Bunge. Analysis of a plastic optical fiber-based displacement sensor. *Applied optics*, 46(25):6256–6262, 2007.

[11] Alvaro AP Boechat, Daoning Su, Denis R Hall, and Julian DC Jones. Bend loss in large core multimode optical fiber beam-delivery systems. In *The Hague'90, 12-16 April*, pages 176–187. International Society for Optics and Photonics, 1990.

[12] V Louis, P Le-Huy, JM Andre, M Abignoli, and Y Granjon. Optical fiber based sensor for angular measurement in rehabilitation. In *Systems, Man and Cybernetics, 1993.'Systems Engineering in the Service of Humans', Conference Proceedings., International Conference on*, pages 153–157. IEEE, 1993.

[13] BHASKER Gupta, HN Bhargaw, and HK Sardana. Qualifying fibre optic temperature sensor using speckle metrology. *Int. Inf. Technol. Knowl. Manage*, 1(2):337–350, 2008.

[14] Lúcia Bilro, Nélia Alberto, João L Pinto, and Rogério Nogueira. Optical sensors based on plastic fibers. *Sensors*, 12(9):12184–12207, 2012.

[15] Lúcia Maria Botas Bilro. *Metrologia óptica com fibra polimérica*. PhD thesis, Universidade de Aveiro, 2011.

[16] Dipl. Phys. Reinhard Jenny. Grundlagen zur faseroptik.

[17] Mitsubishi Mitsubishi Rayon Co. LTD. *Specification Sheet GH4001 High-Performance Plastic Optical Fiber, Eska*, 2001.

[18] Alberto Tapetado Moraleda, Carmen Vázquez García, Joseba Zubia Zaballa, and Jon Arrue. A temperature sensor based on a polymer optical fiber macro-bend. *Sensors*, 13(10):13076–13089, 2013.

[19] Mustapha Remouche, Francis Georges, and Patrick Meyrueis. Flexible optical waveguide bent loss attenuation effects analysis and modeling application to an intrinsic optical fiber temperature sensor. *Optics and Photonics Journal*, 2(01):1, 2012.

[20] Vasyl Varyshchuk, Yaroslav Bobitski, and Hans Poisel. Multimode polymer optical fiber strain gauge based on speckle correlation. *International Journal of Microelectronics and Computer Science*, 5(3):111–115, 2014.

[21] Yimin Gan and Wolfgang Steinchen. Speckle methods. In *Springer Handbook of Experimental Solid Mechanics*, pages 655–674. Springer, 2008.

[22] Joseph W Goodman. Some fundamental properties of speckle. *JOSA*, 66(11):1145–1150, 1976.

[23] J Arrue, J Zubia, G Fuster, and D Kalymnios. Light power behaviour when bending plastic optical fibres. In *Optoelectronics, IEE Proceedings-*, volume 145, pages 313–318. IET, 1998.

[24] DQ Ying, XM Tao, W Zheng, and GF Wang. Fabric strain sensor integrated with looped polymeric optical fiber with large angled v-shaped notches. *Smart Materials and Structures*, 22(1):015004, 2013.

[25] Alexander Djordjevich and Marijana Boskovic. Curvature gauge. *Sensors and Actuators A: Physical*, 51(2):193–198, 1996.

[26] João Miguel Serras Dias. Sensores baseados em fibras óticas poliméricas, 2013.

[27] Anna Grazia Mignani and Francesco Baldini. Biomedical sensors using optical fibres. *Reports on Progress in Physics*, 59(1):1, 1996.

[28] Jianjun Ma and Anand Asundi. Structural health monitoring using a fiber optic polarimetric sensor and a fiber optic curvature sensor-static and dynamic test. *Smart materials and structures*, 10(2):181, 2001.

[29] Alberto Vallan, Maria Luisa Casalicchio, Alessio Penna, and Guido Perrone. An intensity based fiber accelerometer. In *Instrumentation and Measurement*

Technology Conference (I2MTC), 2012 IEEE International, pages 1078–1082. IEEE, 2012.

[30] Yong Zhao, Pengsheng Li, Chenshuang Wang, and Zhaobang Pu. A novel fiber-optic sensor used for small internal curved surface measurement. *Sensors and Actuators A: Physical*, 86(3):211–215, 2000.

[31] D Sastikumar, G Gobi, and B Renganathan. Determination of the thickness of a transparent plate using a reflective fiber optic displacement sensor. *Optics & Laser Technology*, 42(6):911–917, 2010.

[32] Luis Rodriguez-Cobo, M Lomer, C Galindez, and José Miguel Lopez-Higuera. Pof vibration sensor based on speckle pattern changes. In *OFS2012 22nd International Conference on Optical Fiber Sensor*, pages 84212Y–84212Y. International Society for Optics and Photonics, 2012.

[33] L Rodriguez-Cobo, M Lomer, A Cobo, E Real, and JM Lopez-Higuera. Wavelength domain multiplexed fiber specklegram sensor. In *OFS2014 23rd International Conference on Optical Fiber Sensors*, pages 91579K–91579K. International Society for Optics and Photonics, 2014.

[34] HS Efendioglu, T Yildirim, O Toker, and K Fidanboylu. Design of intelligent fiber optic statistical mode sensors using novel features and artificial neural networks. In *Innovations in Intelligent Systems and Applications (INISTA), 2012 International Symposium on*, pages 1–4. IEEE, 2012.

[35] M Lomer, L Rodriguez-Cobo, P Revilla, G Herrero, F Madruga, and JM Lopez-Higuera. Speckle pof sensor for detecting vital signs of patients. In *OFS2014 23rd International Conference on Optical Fiber Sensors*, pages 91572I–91572I. International Society for Optics and Photonics, 2014.

[36] Rudi Irawan, Tjin Swee Chuan, Tay Chia Meng, and Tan Khay Ming. Rapid constructions of microstructures for optical fiber sensors using a commercial co2 laser system. *The open biomedical engineering journal*, 2:28, 2008.

[37] Liu Renqiang, Fu Zhuang, Zhao Yanzheng, Cao Qixin, and Wang Shuguo. Operation principle of a bend enhanced curvature optical fiber sensor. In

Intelligent Robots and Systems, 2006 IEEE/RSJ International Conference on, pages 1966–1971. IEEE, 2006.

[38] Nabeel Ahmed, Patricia Scully, John Vaughan, Christine Brown Wilson, and Krikor Ozanyan. Polymer optical fibre sensor for measuring breathing rate of lying person. 2014.

[39] Anatoly Babchenko, Boris Khanokh, Yoseph Shomer, and Meir Nitzan. Fiber optic sensor for the measurement of respiratory chest circumference changes. *Journal of biomedical optics*, 4(2):224–229, 1999.

[40] Alberto Vallan, Maria Luisa Casalicchio, Massimo Olivero, and Guido Perrone. Two-dimensional displacement sensor based on plastic optical fibers. *Instrumentation and Measurement, IEEE Transactions on*, 62(5):1233–1240, 2013.

[41] Kyoobin Lee and Dong-Soo Kwon. Wearable master device using optical fiber curvature sensors for the disabled. In *Robotics and Automation, 2001. Proceedings 2001 ICRA. IEEE International Conference on*, volume 1, pages 892–896. IEEE, 2001.

[42] M Kovacević, A Djordjevich, and D Nikezić. An analytical approach and optimization of curvature gauge. In *Journal of Physics: Conference Series*, volume 48, page 850. IOP Publishing, 2006.

[43] Milan S Kovacevic, Alexandar Djordjevich, and Dargoslav Nikezić. Analytical optimization of optical fiber curvature gauges. *Sensors Journal, IEEE*, 8(3):227–232, 2008.

[44] Yili Fu, Haiting Di, and Renqiang Liu. Light intensity modulation fiber-optic sensor for curvature measurement. *Optics & Laser Technology*, 42(4):594–599, 2010.

[45] Yili Fu and Haiting Di. Fiber-optic curvature sensor with optimized sensitive zone. *Optics & Laser Technology*, 43(3):586–591, 2011.

[46] Haiting Di. Space curve fitting method based on fiber-optic curvature gages. *Optics & Laser Technology*, 44(1):290–294, 2012.

[47] Dragan Z Stupar, Jovan S Bajić, Bojan M Dakić, Miloš P Slankamenac, and Miloš B Živanov. The possibility of using a plastic optical fibre as a sensing element in civil structural health monitoring. *Physica Scripta*, 2013(T157):014031, 2013.

[48] Hooman Dejnabadi, Brigitte M Jolles, and Kamiar Aminian. A new approach to accurate measurement of uniaxial joint angles based on a combination of accelerometers and gyroscopes. *Biomedical Engineering, IEEE Transactions on*, 52(8):1478–1484, 2005.

[49] Madhavi M Patil and Otto Prohaska. Fiber optic sensor for joint angle measurement. In *Engineering in Medicine and Biology Society, 1988. Proceedings of the Annual International Conference of the IEEE*, pages 803–804. IEEE, 1988.

[50] Kevin SC Kuang, Wesley J Cantwell, and Patricia J Scully. An evaluation of a novel plastic optical fibre sensor for axial strain and bend measurements. *Measurement Science and Technology*, 13(10):1523, 2002.

[51] L Cherbi, M Mehenni, and R Aksas. Conception and realization of an angular optical sensor. *Microwave and optical technology letters*, 40(6):500–503, 2004.

[52] Ursula Jane Brush. Design and validation of an intensity-based pof bend sensor applications in measuring three-dimensional trunk motion. Master's thesis, The Ohio State University, 2010.

[53] Lee Danisch, Kevin Englehart, and Andrew Trivett. Spatially continuous six degree of freedom position and orientation sensor. *Sensor Review*, 19(2):106–112, 1999.

[54] Lúcia Bilro, José G Oliveira, João L Pinto, and Rogério N Nogueira. Pof metrology in physics medicine and rehabilitation. In *(EWOFS'10) Fourth European Workshop on Optical Fibre Sensors*, pages 76531T–76531T. International Society for Optics and Photonics, 2010.

[55] L Bilro, JG Oliveira, JL Pinto, and RN Nogueira. A reliable low-cost wireless and wearable gait monitoring system based on a plastic optical fibre sensor. *Measurement Science and Technology*, 22(4):045801, 2011.

[56] Omnivision. *OV5647 5-Megapixel product brief*, 2010.

[57] Clemens Hägele, Anselmo Frizera Neto, and Maria José Pontes. Polymeric optical fiber curvature sensor measuring technique based on speckle pattern image processing. In *Paper accepted for presentation at XII. SBAI 2015, Simpósio Brasileiro de Automação Inteligente*. SBAI, 2015.

[58] Raspberry Pi Foundation. *Raspberry Pi Model B+ Datasheet*.

[59] Rafael C Gonzalez and Richard E Woods. *Digital image processing, 2nd*, volume 2. SL: Prentice Hall, 2002.

[60] Carlo Tomasi and Roberto Manduchi. Bilateral filtering for gray and color images. In *Computer Vision, 1998. Sixth International Conference on*. IEEE, 1998.

[61] Richard Szeliski. *Computer vision: algorithms and applications*. Springer Science & Business Media, 2010.

[62] John Canny. A computational approach to edge detection. *Pattern Analysis and Machine Intelligence, IEEE Transactions on*, (6):679–698, 1986.

Abbreviations

3D	Three Dimensions
AOC	Amount of contours
AOS	Amount of speckles
ARM	Acorn RISC machine
BGR	Blue Green Red
CCD	Charge Coupled Device
CMOS	Complementary Metal-Oxide-Semiconductor
CPE	Chlorinated Polyethylene
CPU	Control Processing Unit
DC	Direct Current
DSP	Digital Signal Processing
EMC	Electro Magnetic Compability
ES	Embedded System
FAPES	Fundacão de Amparo á Pesquisa do Espirito Santo
FBG	Fiber Bragg Grating
FPS	Frames Per Second
GB	Giga Byte
GI	Graded Index
GPIO	General Purpose Input Output
I/O	Input / Output
IOF	Intensity of light
IP	Internet Protocol
LABTEL	Laboratorio de Telecommunicações
LAN	Local Area Network
LASER	Light amplification by stimulated emission of radiation
LED	Light Emitting Diode
LTS	Long Time Support
MB	Mega Byte

MHz	Mega Hertz
MLP	Multilayer Perceptron
MSE	Mean Square Error
MSI	Multi Step Index
MSV	Mean Speckle Intensity Variation
NA	Numerical Aperture
NDE	Non Destructive Evaluation
NDT	Non Destructive Testing
NMS	Non Maximum Suppression
OPENCV	Open Computer Vision
OS	Operating System
PE	Polyethylene
PMMA	Polymethyl Methacrylate
POF	Polymer Optical Fibre
PVC	Polyvinylchloride
RGB	Red, Green, Blue
RMS	Root Mean Square
ROI	Region of Interest
RPI	Raspberry Pi
RTOS	Real Time Operating system
SD	Secure Digital
SDRAM	Synchronous Dynamic Random Access Memory
SI	Step Index
SNR	Signal to Noise Ratio
SoC	System On A Chip
TCP	Transmission Control Protocol
UFES	Universidade Federal de Espirito Santo
USB	Universal Serial Bus
V	Voltage
WAN	Wireless area network

List of Figures

List of Tables